

University of Windsor

## Scholarship at UWindor

---

Electronic Theses and Dissertations

Theses, Dissertations, and Major Papers

---

1988

### Collisional relaxation in 5(2)P potassium atoms.

Randolph William Derek. Berends  
*University of Windsor*

Follow this and additional works at: <https://scholar.uwindsor.ca/etd>

---

#### Recommended Citation

Berends, Randolph William Derek., "Collisional relaxation in 5(2)P potassium atoms." (1988). *Electronic Theses and Dissertations*. 1469.  
<https://scholar.uwindsor.ca/etd/1469>

This online database contains the full-text of PhD dissertations and Masters' theses of University of Windsor students from 1954 forward. These documents are made available for personal study and research purposes only, in accordance with the Canadian Copyright Act and the Creative Commons license—CC BY-NC-ND (Attribution, Non-Commercial, No Derivative Works). Under this license, works must always be attributed to the copyright holder (original author), cannot be used for any commercial purposes, and may not be altered. Any other use would require the permission of the copyright holder. Students may inquire about withdrawing their dissertation and/or thesis from this database. For additional inquiries, please contact the repository administrator via email ([scholarship@uwindsor.ca](mailto:scholarship@uwindsor.ca)) or by telephone at 519-253-3000ext. 3208.



National Library  
of Canada

Bibliothèque nationale  
du Canada

Canadian Theses Service

Service des thèses canadiennes

Ottawa, Canada  
K1A 0N4

## NOTICE

The quality of this microform is heavily dependent upon the quality of the original thesis submitted for microfilming. Every effort has been made to ensure the highest quality of reproduction possible.

If pages are missing, contact the university which granted the degree.

Some pages may have indistinct print especially if the original pages were typed with a poor typewriter ribbon or if the university sent us an inferior photocopy.

Previously copyrighted materials (journal articles, published tests, etc.) are not filmed.

Reproduction in full or in part of this microform is governed by the Canadian Copyright Act, R.S.C. 1970, c. C-30.

## AVIS

La qualité de cette microforme dépend grandement de la qualité de la thèse soumise au microfilmage. Nous avons tout fait pour assurer une qualité supérieure de reproduction.

S'il manque des pages, veuillez communiquer avec l'université qui a conféré le grade.

La qualité d'impression de certaines pages peut laisser à désirer, surtout si les pages originales ont été dactylographiées à l'aide d'un ruban usé ou si l'université nous a fait parvenir une photocopie de qualité inférieure.

Les documents qui font déjà l'objet d'un droit d'auteur (articles de revue, tests publiés, etc.) ne sont pas microfilmés.

La reproduction, même partielle, de cette microforme est soumise à la Loi canadienne sur le droit d'auteur, SRC 1970, c. C-30.

COLLISIONAL RELAXATION  
IN  
52P POTASSIUM ATOMS

BY

RANDOLPH WILLIAM DEREK BERENDS

A Dissertation  
Submitted to the Faculty of Graduate Studies through the  
Department of Physics in Partial Fulfilment  
of the requirements for the Degree of  
Doctor of Philosophy at  
The University of Windsor

Windsor, Ontario, Canada

1988

Permission has been granted to the National Library of Canada to microfilm this thesis and to lend or sell copies of the film.

The author (copyright owner) has reserved other publication rights, and neither the thesis nor extensive extracts from it may be printed or otherwise reproduced without his/her written permission.

L'autorisation a été accordée à la Bibliothèque nationale du Canada de microfilmer cette thèse et de prêter ou de vendre des exemplaires du film.

L'auteur (titulaire du droit d'auteur) se réserve les autres droits de publication; ni la thèse ni de longs extraits de celle-ci ne doivent être imprimés ou autrement reproduits sans son autorisation écrite.

ISBN 0-315-43729-4

ABX 3320

© Randolph W. D. Berends 1988

## ABSTRACT

Collisional excitation transfer and relaxation of K  $5^2P$  atoms in collisions with noble gases, as well as the radiative lifetimes of the K  $5P$ ,  $6P$  and  $7P$  fine-structure states have been investigated by methods of atomic fluorescence spectroscopy.

Potassium vapour was mixed in a cell with a noble gas and selectively excited by pulsed dye-laser radiation to the  $5^2P_{1/2}$  or the  $5^2P_{3/2}$  state in zero magnetic field and to the  $5^2P_{1/2-1/2}$  or the  $5^2P_{3/2-3/2}$  Zeeman substate in a field of 70 kG. Interferometric analysis of the fluorescence emitted from the directly (optically) excited state and that emitted from the collisionally populated states allowed the determination of the fine-structure mixing cross sections for collisions with He, Ne, Ar, Kr and Xe in zero magnetic field. Excitation transfer between Zeeman substates was investigated for collisions between the selectively excited  $5P$  atoms and He, Ne and Ar atoms, allowing the determination of the multipole relaxation (depolarization) cross sections for dipole, quadrupole and octupole decay, as well as the Zeeman and fine-structure mixing cross sections and orientation transfer cross sections. A comparison of theoretical calculations with the experimental data has been made and the rate equations governing multipole relaxation and including effects due to strong fine-structure mixing on the multipole relaxation, have been described in detail.

The radiative lifetimes of the individual fine-structure components of the K 5P, 6P and 7P states have been determined experimentally by means of time-resolved laser-induced fluorescence techniques. These data are compared with numerous theoretical calculations and the available experimental values.

For my family



## ACKNOWLEDGEMENTS

I am most grateful to Dr. L. Krause, under whose supervision this research was conducted, for years of advice and constructive criticism and in particular for his tireless reading of this dissertation in manuscript. I would like to express my sincere gratitude to Dr. W. Kedzierski for his invaluable advice and assistance with experimental aspects of this research and for the friendship I enjoyed during our period of association. I would like to express my thanks to Dr. W. E. Baylis for his assistance with respect to the theoretical aspects of this work.

I would like to acknowledge the expertise of the staff of the Electronics Shop under the supervision of Mr. B. Masse, and to Mr. P. Seguin, for the design, construction and maintenance of the many electronic components necessary for the success of these experiments. I would like to express my thanks to the Superintendent of the Machine Shop Mr. W. Grewe for his skill and assistance in designing and constructing the precise mechanical and optical fixtures which contributed to the success of this research and for the friendship I enjoyed during our period of association. I would like to thank Mr. A. Buzzeo for his skill in preparing the diagrams which appear in this dissertation.

I am indebted to the National Research Council for financial assistance in the form of scholarships which were awarded to me in the years 1982-1986.

## TABLE OF CONTENTS

ABSTRACT .....	iv
DEDICATION .....	vi
ACKNOWLEDGEMENTS .....	vii
LIST OF TABLES .....	x
LIST OF FIGURES .....	xi
1. INTRODUCTION .....	1
2. THEORETICAL .....	10
2.1 Fine-structure Mixing Between the 5P states of Potassium .....	10
2.2 Application of Density Matrix Formalism to the Collisional Decay of Atomic Multipole Moments .....	14
2.3 The Radiative Lifetimes of the Potassium 5P, 6P and 7P States .....	31
3. THE APPARATUS AND EXPERIMENTAL PROCEDURES .....	33
3.1 The Apparatus and Procedure Used in Fine- structure and Zeeman Mixing Experiments .....	33
3.1.1 The Fluorescence Cell, Oven and Vacuum System .....	39
3.1.2 The Superconducting Magnet .....	41
3.1.3 The Interferometer and Synchronization System .....	43
3.1.4 The Effect of Gated Fluorescence Detection .....	47
3.1.5 The Design and Operation of a Potassium Thermionic Diode .....	52
3.1.6 A Fizeau Wavemeter with Single-Mode Optical Fibre Coupling .....	55
a. Principle of Operation .....	55

b. Details of Construction .....	56
c. Calibration .....	59
d. Realignment of the Optical Components ...	62
e. Performance Specifications .....	64
3.2 Description of the Apparatus for Lifetime Measurements .....	68
3.2.1 Experimental Procedure .....	74
4. RESULTS AND DISCUSSION .....	76
4.1 Fine-structure Excitation Transfer .....	76
4.2 Relaxation of the Multipole Moments in the 5P State of Potassium .....	89
4.3 Radiative Lifetimes of the 5P, 6P and 7P Fine-structure States .....	130
5. CONCLUSIONS .....	137
APPENDIX A: Zeeman Splitting of the P and D States .....	139
APPENDIX B: Feasibility of an Experimental Study of Zeeman Mixing In the 5D State .....	142
1.. Applications of Density Matrix Formalism to the Collisional Decay of Atomic Multipole Moments in the D States .....	142
2. Preliminary Experimental Study Of The D States .	151
BIBLIOGRAPHY .....	154
VITA AUCTORIS .....	157

## LIST OF TABLES

(3.5)	Excited states detected with the thermionic diode .....	54
(4.1.1)	Fine-structure Mixing Cross Sections for He, Ne, Ar, Kr and Xe .....	88
(4.2.1)	5P Zeeman Mixing Cross Sections for collisions with He, Ne and Ar .....	117
(4.2.2)	5P Fine-Structure Mixing and Orientation Transfer Cross Sections .....	118
(4.2.3)	5P Multipole Relaxation Cross Sections .....	119
(4.3.1)	Lifetimes of the 5P, 6P and 7P States in Potassium .....	135
(6.1)	Zeeman Displacement $\Delta\nu$ in Relation to Magnetic Field Strength B (G) .....	139
(7.1)	Relative $A_i$ Coefficients for 5D- $\rightarrow$ 4P Polarized Emission .....	148

## LIST OF FIGURES

(1)	Partial Grotian Diagram for the potassium atom	9
(3.1)	Schematic arrangement of the apparatus for fine-structure and Zeeman mixing .....	38
(3.1.4)	A plot of the time delay correction factor against He pressure .....	51
(3.2)	Optical layout of the Fizeau wavemeter .....	66
(3.3)	Schematic diagram of the electronic data acquisition system of the wavemeter .....	67
(3.4)	Schematic diagram of the apparatus used for lifetime measurements .....	73
(4.1.1)	Interferogram of the 4044/4047 Å 5P fluorescence doublet in K with 200 mtorr Kr ..	79
(4.1.2)	Plots of fluorescence ratios $\eta_1$ and $\eta_2$ against He and Ar pressure .....	81
(4.1.3)	Plots of fluorescence ratios $\eta_1$ and $\eta_2$ against Ne, Kr and Xe pressure .....	83
(4.1.4)	Plots of collision numbers $Z_{12}$ and $Z_{21}$ against Ar and He pressure .....	85
(4.1.5)	Plots of collision numbers $Z_{12}$ and $Z_{21}$ against Ne, Kr and Xe pressure .....	87
(4.2.1)	Energy level diagram of the 5 <sup>2</sup> P Zeeman substates in K, showing their $\sigma$ decays to the ground state .....	100
(4.2.2)	A trace of the Zeeman fluorescence spectrum emitted from K vapour mixed with 50 mtorr Ar .	102
(4.2.3)	A trace of the Zeeman fluorescence spectrum emitted from K vapour mixed with 150 mtorr Ne	104
(4.2.4)	Plots of the Zeeman fluorescence intensity (and population) ratios arising from the S <sup>2</sup> P <sub>1/2-1/2</sub> excitation showing effects of mixing induced in K-He collisions .....	106

(4.2.5)	Plots of the Zeeman fluorescence intensity (and population) ratios arising from $S^2P_{3/2-3/2}$ excitation showing effects of mixing induced in K-He collisions .....	108
(4.2.6)	Plots of the Zeeman fluorescence intensity (and population) ratios arising from $S^2P_{1/2-1/2}$ excitation showing effects of mixing induced in K-Ne collisions .....	110
(4.2.7)	Plots of the Zeeman fluorescence intensity (and population) ratios arising from $S^2P_{3/2-3/2}$ excitation showing effects of mixing induced in K-Ne collisions .....	112
(4.2.8)	Plots of the Zeeman fluorescence intensity (and population) ratios arising from $S^2P_{1/2-1/2}$ excitation showing effects of mixing induced in K-Ar collisions .....	114
(4.2.9)	Plots of the Zeeman fluorescence intensity (and population) ratios arising from $S^2P_{3/2-3/2}$ excitation showing effects of mixing induced in K-Ar collisions .....	116
(4.2.10)	Plots of the Zeeman population ratios obtained from a computer simulation of the relaxation of the 5P Zeeman manifold, showing effects of mixing induced in K-He collisions .....	121
(4.2.11)	Plots of multipole relaxation rates $\lambda_{ii}^{(0)}$ against $N\nu, \tau$ for He (exp.) .....	123
(4.2.12)	Plots of multipole relaxation rates $\lambda_{ii}^{(1)}$ against $N\nu, \tau$ for He (theor.) .....	125
(4.2.13)	Plot of eqs. (2.2.100-101) for He (exp.) .....	127
(4.2.14)	Plot of eqs. (2.2.100-101) for He (theor.) ...	129
(4.3.1)	A semilogarithmic plot of the fluorescence intensity against time showing the decay of the $K7^2P_{1/2}$ state .....	134
(6.1)	The relative displacements of the 5P Zeeman substates ( $\text{cm}^{-1}$ ) in a magnetic field of 70 kG (drawn to scale) .....	141
(7.1)	Transition diagram for the radiative decay of the $S^2D$ state .....	150

## 1 INTRODUCTION

The experimental and theoretical study of collisional interactions of excited atoms with ground state atoms and molecules has continued to be of interest since the pioneering work of Wood (1917) to the present day. These interactions are of fundamental importance to the understanding of phenomena taking place in the upper atmosphere, plasmas, stellar atmospheres, lasers and other systems where atoms and molecules are continuously being excited and de-excited by the absorption and emission of radiation and by processes of collisional excitation transfer. These processes may be described in terms of reaction rates or cross sections governing the particular interaction. The knowledge of these parameters allows the development of theoretical models describing the interaction, which may then be used to predict certain experimental observations. The intensive investigation of the collisional interactions of alkali metal atoms with perturber gas atoms has been aided by their relatively simple electronic structure, which lends itself readily to theoretical modeling, and by the facility with which relatively high density vapours of these metals may be obtained at easily produced temperatures in a laboratory.

The collisional interaction may be either elastic or inelastic. Elastic collisions are those which preserve the kinetic energy of the system, however the long range electromagnetic forces distort the electron distribution about the colliding partners, resulting in the broadening and shift of the emission lines. Inelastic collisions include a variety of interactions in which all or part of the initial excitation energy is transferred out of the

originally excited state. Quenching is a process in which the energy of an excited state is transferred to its collision partner without the direct emission of radiation (this may be due to the excitation of various degrees of freedom of the perturber, such as the rotational and vibrational states of a molecule). Inelastic collisions, in which only a part of this energy is transferred, are characterized by the emission of sensitized fluorescence of wavelength different from the direct fluorescence emitted from the initially excited state.

The study of quenching and excitation transfer began with the investigations by Wood (1918) and coworkers (Wood and Dunoyer 1914). Other groups (Lochte-Holtgreven 1928) studied resonance fine-structure mixing in Na with various collision partners. Cario and Franck (1922) studied excitation transfer between Hg and Tl. In later investigations Seiwert (1956) measured and calculated cross sections for fine-structure mixing in Na with corrections for trapping of resonance radiation which occurs in high density vapours. Many of the subsequent experiments, carried out here and elsewhere, are described in review articles by Krause (1972), Baylis (1978) and Elbel (1978).

Wood (1922) discovered the pressure broadening of the Hg resonance line, and also, that the addition of a buffer gas destroyed the polarization characteristics of the resonance fluorescence emitted from excited Hg vapour. An atomic vapour is said to be polarized if a non-Boltzmann population distribution of Zeeman substates exists in the vapour. von Keussler (1927) measured the degree of polarization of the fluorescence emitted from Hg vapour in the presence of perturber gases and Mrozowski (1932) used selective excitation techniques to excite hyperfine structure substates of Hg. Many of these early studies,



along with descriptions of the ingenious optical excitation methods employed, have been described by Mitchell and Zemansky (1934).

The optical pumping of a particular atomic state or substate may create a non-equilibrium population of states within an ensemble of atoms. In particular, the selective optical excitation of Zeeman substates results in the polarization of the vapour, which also manifests itself in the polarization of the emitted fluorescence. The atomic polarization may be described as the creation of a bulk magnetic multipole moment in the vapour. The density matrix formalism (Fano 1957, Omont 1977, Baylis 1978) may be employed to express the population distribution of the polarized vapour in terms of irreducible tensor operators which define the  $2^L$ th multipole components of the bulk multipole moment. The monopole or occupation component ( $L=0$ ) corresponds to the total population of the fine-structure Zeeman manifold. The dipole or orientation component ( $L=1$ ) describes a population characterized by the preferred occupation of Zeeman substates whose quantum numbers are of the same sign (e.g.  $m_j = +3/2, +1/2$ ). The alignment or the quadrupole component ( $L=2$ ) describes a population distribution corresponding to the predominant occupation of Zeeman substates whose magnetic quantum numbers have the same absolute magnitude (e.g.  $m_j = \pm 1/2$ ) and the octupole component ( $L=3$ ) describes a higher order atomic polarization distribution.

Collisional depolarization experiments may be classified into those performed in low magnetic fields and those done in higher fields. In low magnetic fields the coupling of the nuclear and electronic angular momenta is preserved in the hyperfine structure of the atom. In higher fields these momenta are effectively decoupled (Paschen-Back effect).

of the hyperfine-structure) simplifying the analysis of the experimental observations (Bulos and Happer 1971). The influence of the hyperfine coupling must be considered in the low field measurements because, even though the nucleus may be considered to be decoupled during the collisional interaction, its immediate recoupling tends to realign the system and dampen the observed effects ('flywheel effect').

Collisions of the polarized atoms with buffer gas atoms such as atoms of noble gases, cause the redistribution of the Zeeman state populations (through collisional excitation transfer) and result in the depolarization of the fluorescence. The depolarization may be described in terms of relaxation rates or cross sections which are different for the various multipole components. The depolarization of a  $2P_{1/2}$  state is described only by a dipole relaxation or disorientation cross section, while the depolarization of a  $2P_{3/2}$  state involves the relaxation of dipole, quadrupole and octupole moments.

An experimental determination of disorientation and disalignment cross sections requires the measurement of the degree of circular and linear polarization  $P_{circ}, P_{lin}$  of the fluorescence, which is defined in terms of the relative intensities of right- and left-circularly and linear polarized radiation emitted by the polarized vapour <sup>1</sup> parallel and perpendicular to the field. However, in order to determine the cross sections for the relaxation of higher moments, the fluorescence must also be spectrally resolved to determine the relative intensities of all the Zeeman components present in the fluorescence. The first reported study in which all the relaxation cross sections were determined, dealt with the interaction of Na(3P) atoms with noble gases in magnetic fields up to 80 KG (Gay and Schneider 1976).

---

<sup>1</sup>  $P_{circ} = (I_{\sigma^+} - I_{\sigma^-}) / (I_{\sigma^+} + I_{\sigma^-})$ ,  $P_{lin} = (I_{||} - I_{\perp}) / (I_{||} + I_{\perp})$

The resolution of the individual Zeeman components in the fluorescence allowed the determination of the  $m_j$  mixing cross sections and of all the multipole relaxation cross sections. Boggy and Franz (1982) studied relaxation of K(4P) atoms in collisions with He, Ne and Kr. Using a modified Zeeman scanning method for optical excitation, Skalinski and Krause (1982) determined the multipole relaxation cross sections for K(4P)-K and K(4P)-Ar interactions in fields up to 10 kG and Berends et al. (1984) carried out a similar determination for interactions with N<sub>2</sub> and H<sub>2</sub>. Theoretical calculations of the relaxation cross sections for noble gases have been reported by several groups, with a varying degree of agreement with experimental data. Depolarization cross sections have been calculated by Behmenburg et al. (1985) for Na-Ar collisions and by Rebentrost et al. (1987) for He in collisions with all of the resonance-state alkali metals, producing order of magnitude agreement with experiments. A detailed theoretical test of interatomic potentials for collisions of K(4P) atoms with Ar carried out by Pascale et al. (1984) yielded good agreement with the experiment of Skalinski and Krause (1982).

Far fewer studies have been attempted to probe interactions of atoms excited to states higher than the resonance states. This investigation describes the first experimental determination of the multipole relaxation cross sections for collisions of K(5P) atoms with He, Ne and Ar in a high magnetic field (70 kG) and these values have been compared with several theoretical calculations of these cross sections. A comprehensive theoretical and experimental study of the K(5P) level by Spielfiedel et al. (1979) yielded the pressure broadening and shift constants for interactions with noble gases. The authors also calculated

the corresponding multipole relaxation cross sections based on the interatomic model potentials of Pascale and Vandeplanque (1974) and utilized both semiclassical and fully quantal computation methods. Spielfiedel and Feautrier (1988) recalculated these cross sections using a fully quantal close coupling method and the model potentials computed by Masnou-Seeuws (1982) for collisions with Ne. A recent calculation of the multipole relaxation cross sections and Zeeman mixing cross sections for collisions of K(5P) atoms with He has been carried out by Pascale (1987) using improved interatomic potentials.

This thesis also describes an experimental study of the radiative lifetimes of the 5P, 6P and 7P fine-structure states. The precise knowledge of excited state lifetimes is required for many experimental investigations and also provides a useful vehicle for comparison of experimental data with increasingly accurate theoretical calculations. The S and D states of potassium have been previously investigated both theoretically and experimentally by Hart and Atkinson (1986), who determined the lifetimes for the fine structure 3, 5, 6 and 7 D states. A recent theoretical treatise and review of alkali metal lifetimes by Theodosiou (1984) distinguishes between the fine structure states of these atoms. While the P states of potassium are relatively easy to excite using laser techniques, separate measurements of the lifetimes of the fine-structure P states have been performed only for the 4P states (Copley and Krause 1969), although the lifetimes of the  $5P_{3/2}$  and  $6P_{3/2}$  states have been measured by Svanberg (1971) using Hanle level-crossing methods; the lifetimes of the 7P states have not been determined experimentally. A partial Grotrian diagram for potassium is shown in Fig. 1.

The experiments described in this thesis were accomplished with pulsed dye laser excitation; previous experiments to determine multipole relaxation cross sections (Gay and Schneider 1976, Boggy and Franz 1982, Skalinski and Krause 1982) have utilized various forms of cw excitation. The complexity of pulsed laser excitation coupled with the simultaneous scanning of an interferometer, required the development of a synchronized photon counting technique which produced interferograms of the resolved fine-structure or Zeeman manifold, digitized in intensity as well as in wavelength resolution. The experiments required the development and modification of a considerable amount of equipment, all of which was of considerable benefit to the ultimate success of the investigations.


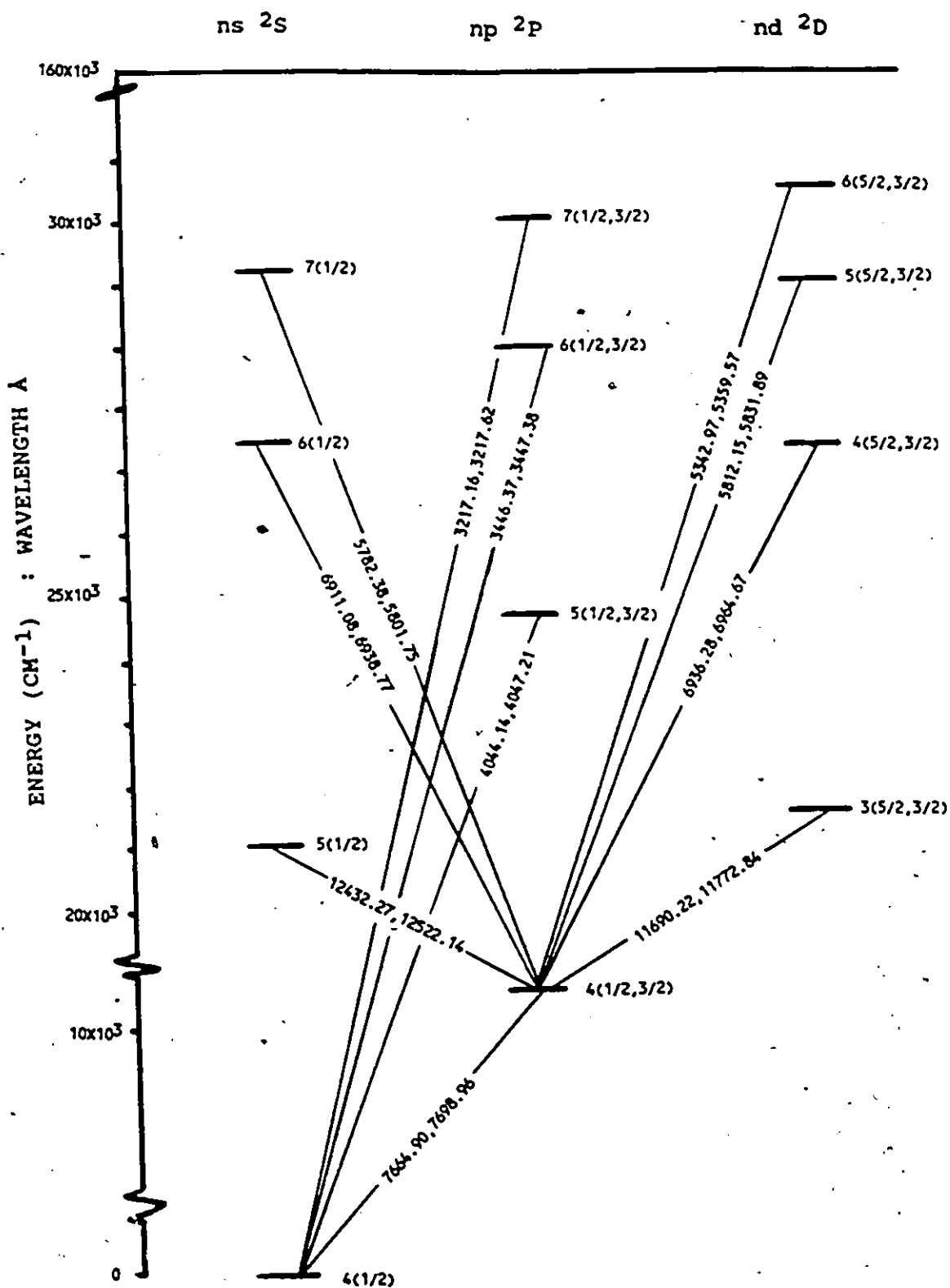


Figure (1)

Partial Grotrian diagram for the potassium atom.



## 2 THEORETICAL

### 2.1 Fine-structure Mixing Between the 5P States of Potassium

The collisional excitation transfer between the fine-structure (fs) states of the 5P level may be described by

$$K(5^2P_{3/2}) + X \rightleftharpoons K(5^2P_{1/2}) + X + \Delta E \quad (2.1.1)$$

where X is a ground-state noble gas atom and  $\Delta E = 18.75 \text{ cm}^{-1}$  is the energy defect between the  $5^2P$  fs states, each of which was excited in turn by a pulsed dye laser. When the  $5^2P_{1/2}$  state is radiatively excited, the time evolution of the population densities of the two states may be described by the rate equations

$$\frac{dN_1}{dt} = s_1 - N_1(\tau^{-1} + Z_{12} + Z_1) + N_2 Z_{21} \quad (2.1.2)$$

$$\frac{dN_2}{dt} = N_1 Z_{12} - N_2(\tau^{-1} + Z_{21} + Z_2) \quad (2.1.3)$$

where  $N_1$  and  $N_2$  are the population densities of the  $5^2P_{1/2}$  and  $5^2P_{3/2}$  substates, respectively,  $s_1$  is the  $5^2P_{1/2}$  radiative excitation rate,  $\tau$  is the radiative lifetime of the  $5^2P$  state, and  $Z_{ab}$  are the frequencies of inelastic collisions per excited atom, leading to the transfer  $a \rightarrow b$ .  $Z_1$  and  $Z_2$  represent the non-radiative depopulation rates (per excited atom) of the fs states by quenching collisions which result in excitation transfer to all states below the 5P state, including the ground state. When the  $5^2P_{3/2}$  state is populated by laser excitation, the time evolution of the two substates is described by the rate equations



$$\frac{dN_2}{dt} = s_2 - N_2(\tau^{-1} + Z_{21} + Z_2) + N_1 Z_{12} \quad (2.1.4)$$

$$\frac{dN_1}{dt} = N_2 Z_{21} - N_1(\tau^{-1} + Z_{12} + Z_1) \quad (2.1.5)$$

where  $s_2$  is the  $S^2P_{3/2}$  radiative excitation rate. Although, because of pulsed excitation, the population densities of the 5P states are time-dependent eqs. (2.1.2-5) can be integrated to give the following ratios (Pace and Atkinson 1974).

$$\frac{\bar{N}_1}{\bar{N}_2} = (\tau^{-1} + Z_{21} + Z_2) / Z_{12} \quad (2.1.6)$$

$$\frac{\bar{N}_2}{\bar{N}_1} = (\tau^{-1} + Z_{12} + Z_1) / Z_{21} \quad (2.1.7)$$

In eq. (2.1.6),  $\bar{N}_2$  represents the population produced by collisional transfer, while  $\bar{N}_1$  is the population due to direct radiative excitation; in eq. (2.1.7) the reverse is the case. Assuming that the measured fluorescence intensities are proportional to the products of the appropriate populations and Einstein A coefficients, eqs. (2.1.6-7) may be expressed in terms of the measured time integrated intensities of the two spectral components.

$$Z_{12} = \eta_2 (A_{1/2} / A_{3/2}) (\tau^{-1} + Z_{21} + Z_2) \quad (2.1.8)$$

$$Z_{21} = \eta_1 (A_{3/2} / A_{1/2}) (\tau^{-1} + Z_{12} + Z_1) \quad (2.1.9)$$

where  $\eta_1$  and  $\eta_2$  are the measured ratios of the fluorescence intensities:

$$\eta_1 = \frac{I(404.7 \text{ nm})}{I(404.4 \text{ nm})} ; \quad \eta_2 = \frac{I(404.4 \text{ nm})}{I(404.7 \text{ nm})} \quad (2.1.10)$$

In each case the component appearing in the denominator is of the same wavelength as the exciting radiation.

Since the  $A_{3/2}$  and  $A_{1/2}$  coefficients are very nearly equal to one another (Wiese et al. 1969), as are the frequencies of the two spectral components, their ratios were omitted from further consideration. The lifetimes of the two fs states were assumed to be equal to each other  $\tau = \tau_1 = \tau_2 = 133 \text{ ns}$  (Svanberg 1971); in a subsequent experiment (see sec. 4.3) these lifetimes were measured directly and found to be equal within the stated limits of experimental error. It was also assumed that  $Z_1$  and  $Z_2$  could be neglected because quenching of alkali fluorescence by collisions with noble gases has been found too weak to be observed, even at buffer gas pressures much higher than those employed here ( $< 250 \text{ mtorr}$ ) (Siara et al. 1972, Bellisio et al. 1968). This assumption was later verified directly by measuring the lifetime of the 5P state in the presence of 50 torr of Ar and detecting no noticeable change from the lifetime measured in the absence of a buffer gas; with the addition of as little as 60 mtorr of  $\text{N}_2$  a 10% decrease in the effective lifetime was measured. Using these approximations, eqs. (2.1.8) and (2.1.9) may be solved for the collision numbers.

$$Z_{12} = \frac{(\eta_2 + \eta_1 \eta_2)}{\tau(1 - \eta_1 \eta_2)} \quad (2.1.11)$$

$$Z_{21} = \frac{(\eta_1 + \eta_1 \eta_2)}{\tau(1 - \eta_1 \eta_2)} \quad (2.1.12)$$

Equations (2.1.11) and (2.1.12) provide the connection between the measured fluorescence intensity ratios and the collision numbers  $Z_{ab}$  which are related to the transfer cross section  $Q_{ab}$  which are defined analogously to the gas kinetic cross section,

$$Z_{ab} = N(X) Q_{ab} v_r \quad (2.1.13)$$

where  $N(X)$  is the density of the noble gas atoms and  $v_r$  is the average relative speed of the colliding partners whose reduced mass is  $\mu$ .

$$v_r = (8kT/\pi\mu)^{1/2} \quad (2.1.14)$$

where  $k$  is the Boltzmann constant and  $T$  is the absolute temperature of the fluorescing vapour-gas mixture.

According to the principle of detailed balancing, the cross sections  $Q_{12}$  and  $Q_{21}$  should be in the ratio

$$\frac{Q_{12}}{Q_{21}} = \frac{Q(1/2 \rightarrow 3/2)}{Q(3/2 \rightarrow 1/2)} = \left(\frac{g_2}{g_1}\right) e^{-\frac{\Delta f}{kT}} \quad (2.1.15)$$

where  $g_1=2$  and  $g_2=4$  are the statistical weights of the fs states.

## 2.2 Application of Density Matrix Formalism to the Collisional Decay of Atomic Multipole Moments

When a potassium atom, excited to one of the  $5^2P$  Zeeman substates, collides with a buffer gas atom such as He, Ne or Ar excitation transfer may be induced to other substates within the  $5^2P$  Zeeman manifold.

The collisional process may be described by the following expressions :

$$K(S^2P_{1/2-1/2}) + X \rightarrow K(S^2P_{J,m}) + X + \Delta E \quad (2.2.1)$$

$$K(S^2P_{3/2-3/2}) + X \rightarrow K(S^2P_{J,m}) + X + \Delta E \quad (2.2.2)$$

where X is a buffer gas atom and  $\Delta E$  is the change in the kinetic energy of the buffer gas atom. When  $J$  or  $J'=1/2$ ,  $m$  or  $m' = \pm 1/2$  ; when  $J$  or  $J'=3/2$ ,  $m$  or  $m' = \pm 3/2$  or  $\pm 1/2$ . There are altogether six Zeeman substates within the  $5P$  doublet. The population density vector  $\bar{N}$ , describing the population density of the potassium atoms in these Zeeman substates, must accordingly be described by a six-dimensional vector.

The time evolution of the population density vector  $\bar{N}$  may be described using density matrix formalism (Baylis, 1978).

$$\dot{\bar{N}} = \frac{d\bar{N}}{dt} = \bar{S} - \bar{\Gamma}\bar{N} - \bar{\gamma}\bar{N} \quad (2.2.3)$$

where  $\bar{S}$  represents the rate at which the Zeeman states are being optically excited,  $\bar{\Gamma}$  is the matrix describing the spontaneous decay rate of the excited state to the ground

state and  $\bar{\gamma}$  is the matrix describing the rate of collisional transfer between all the available Zeeman sublevels. Under steady-state conditions an equilibrium is reached such that the change in the population density with time approaches zero. When optical excitation is accomplished by means of short laser pulses, eq. (2.2.3) can be integrated (Pace and Atkinson 1974) to yield the following expression for the time-averaged population of the excited state in terms of the spontaneous decay, collisional transfer and the radiative excitation rates.

$$\bar{S} - \bar{\Gamma} \bar{N} - \bar{\gamma} \bar{N} = 0 \quad (2.2.4)$$

The horizontal bars indicate time-integrated quantities (the bars will be suppressed throughout the following discussion for the sake of simplicity).  $\bar{N}$  may be expressed in terms of the spherical basis vectors directly related to the multipole density distribution. The vectors describing the six-dimensional Zeeman manifold are defined by the following expressions.

$$\bar{T}_{1L}^T = (\bar{a}_L^T, 0) \quad L = 0, 1 \quad (2.2.5)$$

$$\bar{T}_{2L}^T = (0, \bar{v}_L^T) \quad L = 0, 1, 2, 3 \quad (2.2.6)$$

Where  $\bar{a}_L^T$  and  $\bar{v}_L^T$  are the 2-dimensional and 4-dimensional spherical-basis vectors, respectively (Bäylis 1983).

$$\bar{a}_0^T = \frac{1}{\sqrt{2}}(1, 1) \quad (2.2.7)$$

$$\bar{a}_1^T = \frac{1}{\sqrt{2}}(1, -1) \quad (2.2.8)$$

$$\bar{v}_0^T = \frac{1}{2}(1, 1, 1, 1) \quad (2.2.9)$$

$$\bar{v}_1^T = \frac{1}{2\sqrt{5}}(3, 1, -1, -3) \quad (2.2.10)$$

$$\bar{v}_2^T = \frac{1}{2}(1, -1, -1, 1) \quad (2.2.11)$$

$$\bar{v}_3^T = \frac{1}{2\sqrt{5}}(1, -3, 3, -1) \quad (2.2.12)$$

The quantities  $\bar{N}$ ,  $\bar{S}$ ,  $\bar{\Gamma}$  and  $\bar{\gamma}$  can be expressed similarly, bearing in mind the statistical weights of the fs states:

$$\bar{N} = \begin{pmatrix} \bar{N}_1 \\ \bar{N}_2 \end{pmatrix} \quad (2.2.13); \quad \bar{N}_1 = \begin{pmatrix} N_{11} \\ N_{22} \\ N_{\frac{1}{2}-\frac{1}{2}} \end{pmatrix} \quad (2.2.14); \quad \bar{N}_2 = \begin{pmatrix} N_{33} \\ N_{22} \\ N_{\frac{3}{2}-\frac{1}{2}} \\ N_{\frac{3}{2}-\frac{3}{2}} \end{pmatrix} \quad (2.2.15);$$

$$\bar{S} = \begin{pmatrix} \bar{S}_1 \\ \bar{S}_2 \end{pmatrix} \quad (2.2.16); \quad \bar{S}_1 = \begin{pmatrix} S_{11} \\ S_{22} \\ S_{\frac{1}{2}-\frac{1}{2}} \end{pmatrix} \quad (2.2.17); \quad \bar{S}_2 = \begin{pmatrix} S_{33} \\ S_{22} \\ S_{\frac{3}{2}-\frac{1}{2}} \\ S_{\frac{3}{2}-\frac{3}{2}} \end{pmatrix} \quad (2.2.18);$$

$$\bar{\Gamma} = \begin{pmatrix} \tau_1^{-1} \mathbb{1}_2 & 0 \\ 0 & \tau_2^{-1} \mathbb{1}_2 \end{pmatrix} \quad (2.2.19); \quad \bar{\gamma} = \begin{pmatrix} \hat{\gamma}_{11} & \hat{\gamma}_{21} \\ \hat{\gamma}_{12} & \hat{\gamma}_{22} \end{pmatrix} \quad (2.2.20);$$

$\mathbb{1}_1$  is the two-dimensional identity matrix,  $\mathbb{1}_2$  is the four-dimensional identity matrix and 0 represents the appropriately dimensioned null matrix.  $\tau = \tau_1 = \tau_2$  is the mean radiative lifetime of the  $5^3P$  state which was taken to be 133 ns (Svanberg 1971) (see section (2.1)). The  $\hat{\gamma}_{ij}$  components of  $\bar{\gamma}$  are  $(2i) \times (2j)$  dimensional matrices. The individual elements of the  $\hat{\gamma}_{ij}$  are the collisional transfer rates  $\gamma_{ij} = \gamma(|Jm\rangle, \rightarrow |J'm'\rangle)$ , which are equal in magnitude to the collision numbers  $Z(J, m \rightarrow J', m')$  (defined in section 2.1). In section 2.1 the direction of excitation transfer

is explicitly included in the rate equations (2.1.2-5). In order that the direction of the collisional transfer be consistent in this notation and all individual cross sections  $\sigma_{ij}$  be defined positive, all the off-diagonal components  $\gamma_{ij}$  of  $\hat{\gamma}$  are defined to be negative and all diagonal components  $\gamma_{ii}$  positive. This notation is summarized as follows:

$$\gamma_{ij} = -Nv_r \sigma_{ij} \quad i \neq j; \quad \gamma_{ii} = Nv_r \sigma_{ii}; \quad \sigma_{ij} > 0 \quad \forall i, j \quad (2.2.21)$$

Substituting eqs. (2.2.13, 16, 19) and (2.2.20) into (2.2.4) leads to

$$\begin{pmatrix} \tau_1^{-1} \mathbb{1}_1 + \hat{\gamma}_{11} & \hat{\gamma}_{21} \\ \hat{\gamma}_{12} & \tau_2^{-1} \mathbb{1}_2 + \hat{\gamma}_{22} \end{pmatrix} \begin{pmatrix} \bar{N}_1 \\ \bar{N}_2 \end{pmatrix} = \begin{pmatrix} \bar{S}_1 \\ \bar{S}_2 \end{pmatrix} \quad (2.2.22)$$

The vectors  $\bar{N}$  and  $\bar{S}$  are now expressed in terms of the spherical basis of (2.2.5) and (2.2.6).

$$\bar{N} = \begin{pmatrix} \bar{N}_1 \\ \bar{N}_2 \end{pmatrix} = \sum_{l=0}^1 \begin{pmatrix} n_1^{(l)} \hat{u}_l \\ \hat{0} \end{pmatrix} + \sum_{l=0}^2 \begin{pmatrix} \hat{0} \\ n_2^{(l)} \hat{v}_l \end{pmatrix} \quad (2.2.23)$$

$$n_1^{(l)} = \hat{u}_l^T \cdot \bar{N}_1 \quad (2.2.24)$$

$$n_2^{(l)} = \hat{v}_l^T \cdot \bar{N}_2 \quad (2.2.25)$$

The equations for  $\bar{S}$ ,  $s_1^{(l)}$  and  $s_2^{(l)}$  follow in an analogous manner. The quantities  $n_1^{(l)}$  and  $n_2^{(l)}$  represent the  $2^l$ -th multipole moment density associated with  $\bar{N}_1$  and  $\bar{N}_2$ , respectively.

Occupation or monopole component of  $\bar{N}_1$ :

$$n_1^{(0)} = \frac{1}{\sqrt{2}} \left( N_{\frac{1}{2} \frac{1}{2}} + N_{\frac{1}{2} -\frac{1}{2}} \right) \quad (2.2.26)$$

Orientation or dipole component of  $\bar{N}_1$ :

$$n_1^{(1)} = \frac{1}{\sqrt{2}} \left( N_{\frac{1}{2}\frac{1}{2}} - N_{\frac{1}{2}-\frac{1}{2}} \right) \quad (2.2.27)$$

Occupation component of  $\bar{N}_2$ :

$$n_2^{(0)} = \frac{1}{2} \left( N_{\frac{3}{2}\frac{3}{2}} + N_{\frac{3}{2}\frac{1}{2}} + N_{\frac{3}{2}-\frac{1}{2}} + N_{\frac{3}{2}-\frac{3}{2}} \right) \quad (2.2.28)$$

Orientation component of  $\bar{N}_2$ :

$$n_2^{(1)} = \frac{1}{2\sqrt{5}} \left( 3N_{\frac{3}{2}\frac{3}{2}} + N_{\frac{3}{2}\frac{1}{2}} - N_{\frac{3}{2}-\frac{1}{2}} - 3N_{\frac{3}{2}-\frac{3}{2}} \right) \quad (2.2.29)$$

Alignment or quadrupole component of  $\bar{N}_2$ :

$$n_2^{(2)} = \frac{1}{2} \left( N_{\frac{3}{2}\frac{3}{2}} - N_{\frac{3}{2}\frac{1}{2}} - N_{\frac{3}{2}-\frac{1}{2}} + N_{\frac{3}{2}-\frac{3}{2}} \right) \quad (2.2.30)$$

Octupole component of  $\bar{N}_2$ :

$$n_2^{(3)} = \frac{1}{2\sqrt{5}} \left( N_{\frac{3}{2}\frac{3}{2}} - 3N_{\frac{3}{2}\frac{1}{2}} + 3N_{\frac{3}{2}-\frac{1}{2}} - N_{\frac{3}{2}-\frac{3}{2}} \right) \quad (2.2.31)$$

When the system is collisionally isotropic, the rotational invariance of the components of  $\hat{y}$  allow eq. (2.2.22) to be expressed in terms of the appropriate multipole densities  $n^{(L)}$  given by eq. (2.2.24-5) (Baylis 1983).

$$\begin{pmatrix} \tau_1^{-1} + \gamma_{11}^{(L)} & \gamma_{21}^{(L)} \\ -\gamma_{12}^{(L)} & \tau_2^{-1} + \gamma_{22}^{(L)} \end{pmatrix} \begin{pmatrix} n_1^{(L)} \\ n_2^{(L)} \end{pmatrix} = \begin{pmatrix} s_1^{(L)} \\ s_2^{(L)} \end{pmatrix} \quad (2.2.32)$$

Where the matrix elements are defined by:

$$\gamma_{11}^{(L)} = \hat{u}_L^T (\hat{y}_{11}) \hat{u}_L \quad L = 0, 1 \quad (2.2.33)$$

$$\gamma_{22}^{(L)} = \hat{v}_L^T (\hat{y}_{22}) \hat{v}_L \quad L = 0, 1, 2, 3 \quad (2.2.34)$$

$$\gamma_{12}^{(L)} = \hat{u}_L^T (\hat{y}_{12}) \hat{v}_L \quad L = 0, 1 \quad (2.2.35)$$

$$\gamma_{21}^{(L)} = \hat{v}_L^T (\hat{y}_{21}) \hat{u}_L \quad L = 0, 1 \quad (2.2.36)$$



$\gamma_{11}^{(L)}$  and  $\gamma_{22}^{(L)}$  are the multipole decay rates and  $\gamma_{ii}^{(0)}$  are the depopulation rates. The elements  $\gamma_{12}^{(0)}$  and  $\gamma_{21}^{(0)}$  are the fs excitation transfer rates for the ( $S^2 P_{1/2} \rightarrow S^2 P_{3/2}$ ) and ( $S^2 P_{3/2} \rightarrow S^2 P_{1/2}$ ) transitions, respectively. The elements  $\gamma_{11}^{(1)}$  and  $\gamma_{22}^{(1)}$  are the fs orientation transfer rates. All other  $\gamma_{ii}^{(L)}$  must vanish to conserve the symmetry relations obeyed by  $\hat{y}$  (Baylis 1983).

The following equations define some of the relationships among the  $\gamma_{ii}^{(L)}$  elements defined in eqs. (2.2.33-36); the notation is consistent with eq. (2.2.21).

$$\gamma_{11}^{(0)} = -\sqrt{2}(\gamma_{12}^{(0)}) \quad (2.2.37)$$

$$\gamma_{22}^{(0)} = -\frac{1}{\sqrt{2}}(\gamma_{21}^{(0)}) \quad (2.2.38)$$

$$\gamma_{12}^{(0)} = -N\nu\sigma_{12}^{(0)} \quad (2.2.39)$$

$$\gamma_{21}^{(0)} = -N\nu\sigma_{21}^{(0)} \quad (2.2.40)$$

$$\gamma_{11}^{(0)} = N\nu\sigma_{11}^{(0)} \quad (2.2.41)$$

$$\gamma_{22}^{(0)} = N\nu\sigma_{22}^{(0)} \quad (2.2.42)$$

$$\sigma_{11}^{(0)} = \sqrt{2}\sigma_{12}^{(0)} \quad (2.2.43)$$

$$\sigma_{22}^{(0)} = \frac{1}{\sqrt{2}}\sigma_{21}^{(0)} \quad (2.2.44)$$

The fs transfer cross sections measured in the absence of a magnetic field (sec. 2.1) are equal to the depopulation cross sections  $\sigma_{11}^{(0)}$  and  $\sigma_{22}^{(0)}$ .

$$Q_{12} = \sigma_{11}^{(0)} \quad (2.2.45)$$

$$Q_{21} = \sigma_{22}^{(0)} \quad (2.2.46)$$

The multipole decay rates  $\gamma_{11}^{(L)}$  and  $\gamma_{22}^{(L)}$  are described in terms of two components,  $\gamma_{ii}^{(0)}$  which describes the multipole decay due to the collisional transfer of excitation between the two fs states, and  $\lambda_{ii}^{(L)}$  which describes the collisional relaxation due to excitation transfer among the Zeeman substates within the L-th fs state.

$$\gamma_{11}^{(1)} = \gamma_{11}^{(0)} + \lambda_{11}^{(1)} \quad (2.2.47)$$

$$\gamma_{22}^{(L)} = \gamma_{22}^{(0)} + \lambda_{22}^{(L)} \quad (2.2.48)$$

These rates are now expressed in terms of the corresponding multipole decay cross sections  $\sigma_{11}^{(L)}$  and  $\sigma_{22}^{(L)}$  ( $L=1,2,3$ ), and the multipole relaxation cross sections  $\lambda_{11}^{(L)}$  and  $\lambda_{22}^{(L)}$ .

$$\gamma_{11}^{(1)} = N\nu\sigma_{11}^{(1)} \quad (2.2.49)$$

$$\gamma_{22}^{(L)} = N\nu\sigma_{22}^{(L)} \quad (2.2.50)$$

$$\lambda_{11}^{(1)} = N\nu\Lambda_{1/2}^{(1)} \quad (2.2.51)$$

$$\lambda_{22}^{(L)} = N\nu\Lambda_{3/2}^{(L)} \quad (2.2.52)$$

$$\sigma_{11}^{(1)} = \sigma_{11}^{(0)} + \Lambda_{1/2}^{(1)} \quad (2.2.53)$$

$$\sigma_{22}^{(L)} = \sigma_{22}^{(0)} + \Lambda_{3/2}^{(L)} \quad (2.2.54)$$

Inverting eq. (2.2.32) yields the following solution for the population densities in terms of the transfer and excitation rates.

$$\begin{pmatrix} n_1^{(L)} \\ n_2^{(L)} \end{pmatrix} = D_L^{-1} \begin{pmatrix} \tau_2^{-1} + \gamma_{22}^{(L)} & -\gamma_{21}^{(L)} \\ -\gamma_{12}^{(L)} & \tau_1^{-1} + \gamma_{11}^{(L)} \end{pmatrix} \begin{pmatrix} s_1^{(L)} \\ s_2^{(L)} \end{pmatrix} \quad (2.2.55)$$

Where  $D_L$ , the determinant of the matrix in eq. (2.2.32), has the following form:

$$D_L = (\tau_1^{-1} + \gamma_{11}^{(L)})(\tau_2^{-1} + \gamma_{22}^{(L)}) - \gamma_{21}^{(L)}\gamma_{12}^{(L)} \quad (2.2.56)$$

The following K coefficients are defined in order to facilitate the manipulation of eq. (2.2.55).

$$K_{ab}^{LL} = \frac{n_b^{(L)}}{n_a^{(L)}} \cdot \frac{s_a^{(L)}}{s_b^{(L)}} \quad a, b = 1, 2 \quad (2.2.57)$$

$$K^{(0)} = \left( \frac{n_2^{(0)} s_1^{(0)}}{n_1^{(0)} s_1^{(0)}} \right) \left( \frac{n_1^{(0)} s_2^{(0)}}{n_2^{(0)} s_2^{(0)}} \right) \quad (2.2.58)$$

$$K^{(1)} = \left( \frac{n_2^{(1)} s_1^{(1)}}{n_1^{(1)} s_1^{(1)}} \right) \left( \frac{n_1^{(1)} s_2^{(1)}}{n_2^{(1)} s_2^{(1)}} \right) \quad (2.2.59)$$

Where  $K_{ab}^{LL}$  is the ratio of the population density of the multipole components within the same fs state,  $K^{(0)}$  (analogous to the product  $\eta_1 \eta_2$  in section 2.1) is the product of the monopole (population) ratio of the collisionally

populated fs state to the directly populated fs state and  $K(1)$  describes the transfer of orientation between the two fs states.

The solution of eq. (2.2.55) in terms of the  $K$  coefficients follows by considering the levels that were directly (radiatively) populated. The first case involves laser excitation of the  $5^2K_{1/2-1/2}$  state while the second case arises from  $5^2K_{3/2-3/2}$  excitation.

Case (1): When the  $K^2P_{1/2-1/2}$  substate is optically excited,

$$\bar{S}_1 = \begin{pmatrix} 0 \\ S_{1/2-1/2} \end{pmatrix}, \quad s_2^{(L)} = 0 \quad (L=0,1,2,3),$$

and eqs. (2.2.55-59) yield the following  $K$  coefficients.

$$K_{11}^{01} = \frac{n_1^{(0)} s_1^{(1)}}{n_1^{(1)} s_1^{(0)}} = \frac{(\tau_2^{-1} + \gamma_{22}^{(0)})}{(\tau_2^{-1} + \gamma_{22}^{(1)})} \cdot \frac{D_1}{D_0} \quad (2.2.60)$$

$$K_{12}^{01} = \frac{\gamma_{12}^{(0)} D_1}{\gamma_{12}^{(1)} D_0} \quad (2.2.61)$$

Case (2): When the  $K^2P_{3/2-3/2}$  substate is optically excited,

$$\bar{S}_2 = \begin{pmatrix} 0 \\ 0 \\ 0 \\ S_{3/2-3/2} \end{pmatrix}, \quad s_1^{(L)} = 0 \quad (L=0,1)$$

$$K_{21}^{01} = \frac{\gamma_{21}^{(0)} D_1}{\gamma_{21}^{(1)} D_0} \quad (2.2.62)$$

$$K_{22}^{01} = \frac{(\tau_1^{-1} + \gamma_{11}^{(0)}) D_1}{(\tau_1^{-1} + \gamma_{11}^{(1)}) D_0} \quad (2.2.63)$$

$$K_{22}^{02} = (1 + \tau_1 \gamma_{11}^{(0)}) \cdot \frac{D_2}{D_0} \quad (2.2.64)$$

$$K_{22}^{03} = (1 + \tau_1 \gamma_{11}^{(0)}) \cdot \frac{D_3}{D_0} \quad (2.2.65)$$

$$\gamma_{12}^{(0)} \gamma_{21}^{(0)} = K^{(0)} (\tau_1^{-1} + \gamma_{11}^{(0)}) (\tau_2^{-1} + \gamma_{22}^{(0)}) \quad (2.2.66)$$

$$\gamma_{12}^{(1)} \gamma_{21}^{(1)} = K^{(1)} (\tau_1^{-1} + \gamma_{11}^{(1)}) (\tau_2^{-1} + \gamma_{22}^{(1)}) \quad (2.2.67)$$

The explicit forms of the determinants  $D_L$  are:

$$\begin{aligned} D_0 &= (\tau_1^{-1} + \gamma_{11}^{(0)}) (\tau_2^{-1} + \gamma_{22}^{(0)}) - \gamma_{21}^{(0)} \gamma_{12}^{(0)} \\ &= (\tau_1^{-1} + \gamma_{11}^{(0)}) (\tau_2^{-1} + \gamma_{22}^{(0)}) (1 - K^{(0)}) \end{aligned} \quad (2.2.68)$$

$$\begin{aligned} D_1 &= (\tau_1^{-1} + \gamma_{11}^{(0)}) (\tau_2^{-1} + \gamma_{22}^{(1)}) - \gamma_{21}^{(1)} \gamma_{12}^{(1)} \\ &= (\tau_1^{-1} + \gamma_{11}^{(0)}) (\tau_2^{-1} + \gamma_{22}^{(1)}) (1 - K^{(1)}) \end{aligned} \quad (2.2.69)$$

$$D_2 = (\tau_1^{-1}) (\tau_2^{-1} + \gamma_{22}^{(2)}) \quad (2.2.70)$$

$$D_3 = (\tau_1^{-1}) (\tau_2^{-1} + \gamma_{22}^{(3)}) \quad (2.2.71)$$

The K coefficients, -defined by eq. (2.2.57-59), describe the multipole population distributions within the Zeeman manifold which are obtained from the intensities of the components of the resolved Zeeman fluorescence spectra through the appropriate A coefficients.

The spontaneous decay of the excited states takes place by linearly polarized  $\pi$  radiation emitted perpendicularly to the magnetic field and circularly polarized  $\sigma$  radiation emitted parallel to the field. In this experiment only the  $\sigma$  components were detected because the superconducting solenoid did not contain a port for perpendicular observation.

For the  $5^2P_{1/2} \rightarrow 4^2S_{1/2}$  and  $5^2P_{3/2} \rightarrow 4^2S_{1/2}$  transitions in zero field, the ratios of the Einstein A coefficients for the emission of polarized radiation are:

$$A_{\frac{3}{2}, \frac{3}{2}}^{\pi} : A_{\frac{3}{2}, \frac{1}{2}}^{\sigma} = 1:2$$

$$A_{\frac{3}{2}, \frac{3}{2}}^{\sigma} : A_{\frac{3}{2}, \frac{1}{2}}^{\sigma} : A_{\frac{3}{2}, \frac{1}{2}}^{\pi} = 3:1:2. \quad (2.2.72)$$

The oscillator strengths for the transitions from the two 5P fs states to the ground state are equal to a good approximation (section 2.1), allowing eq. (2.2.72) to be expressed for the emission of circularly polarized light (Boggy and Franz 1982) by the following:

$$A_{\frac{3}{2}, \frac{3}{2}}^{\sigma} : A_{\frac{3}{2}, \frac{1}{2}}^{\sigma} : A_{\frac{3}{2}, \frac{1}{2}}^{\pi} = 3:1:2 \quad (2.2.73)$$

The Einstein A coefficients, which give the spontaneous electric dipole transition probability associated with the emission of circularly polarized radiation, must be modified to include the effect of increased mixing between the Zeeman substates due to perturbation by the magnetic field. The calculation of the magnetic field correction (the first order Zeeman perturbation) was carried out in detail by Boggy and Franz (1982). They performed a Clebsch-Gordan expansion of the eigenfunctions of the Zeeman manifold and evaluated the expectation value of the perturbation Hamiltonian which yielded the off-diagonal matrix elements for the perturbed wave functions. The perturbed wave functions were then expressed in terms of the unperturbed wave functions and the expectation value of the electric dipole operator was calculated to determine the required A coefficients:

$$A_{\frac{3}{2}, \frac{3}{2}}^{\sigma}(B) : A_{\frac{3}{2}, \frac{1}{2}}^{\sigma}(B) : A_{\frac{3}{2}, \frac{1}{2}}^{\pi}(B) =$$

$$\begin{aligned}
 -3 &: 1 - \frac{2\sqrt{2}\mu_B B}{3\Delta E} : 2 + \frac{\sqrt{2}\mu_B B}{3\Delta E} \\
 &= 3 : .83 : 2.09
 \end{aligned} \tag{2.2.74}$$

where  $\mu_B$  is the Bohr magneton,  $B = 70$  kG and  $\Delta E = 18.75 \text{ cm}^{-1}$  is the fs splitting. This correction is important in the present experiment as, at this field strength, the Zeeman splitting and the fs splitting are comparable.

The population ratios are related as follows to the measured ratios of fluorescence intensities:

$$\frac{N_{JM}}{N_{J'M'}} = \frac{I_{JM}}{I_{J'M'}} \cdot \frac{A_{J'M'}^g(B)}{A_{JM}^g(B)} \tag{2.2.75}$$

In order to determine the multipole relaxation cross sections from the measured intensity ratios, the collision rates  $\gamma_{21}^{(0)}$ ,  $\gamma_{12}^{(0)}$ ,  $\gamma_{11}^{(0)}$  and  $\gamma_{22}^{(0)}$ , appearing in eqs. (2.2.58-71), must be determined. These rates are directly obtainable from the fs mixing cross sections which have been determined in zero field (see eqs. (2.2.45-46) and section 2.1), and may also be determined from the experimental data determined in the presence of a magnetic field. Equations (2.2.64-65) may be solved directly for  $\gamma_{22}^{(2)}$  and  $\gamma_{21}^{(2)}$  using these values of  $\sigma_{12}^{(0)}$  and  $\sigma_{21}^{(0)}$ . Equations (2.2.60-63) are coupled through the orientation transfer rate product  $\gamma_{12}^{(1)}\gamma_{21}^{(1)}$  contained in eq. (2.2.69). An estimate for  $\gamma_{12}^{(1)}\gamma_{21}^{(1)}$  can be obtained from the experimental data assuming single collision conditions, which require the collision rate to be much smaller than the reciprocal lifetime of the excited state,  $N\nu, Q(Jm \rightarrow J'm') \ll \tau^{-1}$ . Under this condition the Zeeman mixing cross section may be expressed as follows.

$$Q(JM \rightarrow J'M') = \frac{1}{N_{\nu\tau}} \frac{N_{J'M'}}{N_{JM}} \quad (2.2.76)$$

The fs orientation transfer rates are defined by

$$\gamma_{12}^{(1)} = -N_{\nu}\sigma_{12}^{(1)} \quad (2.2.77) \quad \gamma_{21}^{(1)} = -N_{\nu}\sigma_{21}^{(1)} \quad (2.2.78)$$

where  $\sigma_{12}^{(1)}$  and  $\sigma_{21}^{(1)}$  are the fs orientation transfer cross sections. Various definitions of the fs transfer rates and orientation transfer rates may be found in the literature (Baylis, 1978; Elbel, 1978); the essential difference between them lies in the normalization factors. The normalization factors used here are obtained by inverting eq. (83) in the article by Baylis (1978), or may be determined by evaluating eqs. (2.2.35-36) and result in the following expressions.

$$\sigma_{21}^{(1)} = \frac{1}{\sqrt{10}} \left( 3Q\left(\frac{1}{2}, -\frac{1}{2} \rightarrow \frac{3}{2}, -\frac{3}{2}\right) + Q\left(\frac{1}{2}, -\frac{1}{2} \rightarrow \frac{3}{2}, -\frac{1}{2}\right) - Q\left(\frac{1}{2}, -\frac{1}{2} \rightarrow \frac{3}{2}, \frac{1}{2}\right) - 3Q\left(\frac{1}{2}, -\frac{1}{2} \rightarrow \frac{3}{2}, \frac{3}{2}\right) \right)$$

$$\sigma_{12}^{(1)} = \frac{\sqrt{10}}{3} \left( Q\left(\frac{3}{2}, -\frac{3}{2} \rightarrow \frac{1}{2}, -\frac{1}{2}\right) - Q\left(\frac{3}{2}, -\frac{3}{2} \rightarrow \frac{1}{2}, \frac{1}{2}\right) \right) \quad (2.2.79)$$

$$\sigma_{21}^{(0)}\left(\frac{1}{2} \rightarrow \frac{3}{2}\right) = \frac{1}{\sqrt{2}} \sum_m Q\left(\frac{1}{2}, -\frac{1}{2} \rightarrow \frac{3}{2}, m\right)$$

$$\sigma_{12}^{(0)} = \sqrt{2} \left( Q\left(\frac{3}{2}, -\frac{3}{2} \rightarrow \frac{1}{2}, -\frac{1}{2}\right) + Q\left(\frac{3}{2}, -\frac{3}{2} \rightarrow \frac{1}{2}, \frac{1}{2}\right) \right) \quad (2.2.80)$$

The resulting experimental values of the fs orientation transfer cross sections are smaller than the fs transfer cross sections by an order of magnitude and thus the product  $\sigma_{12}^{(0)}\sigma_{21}^{(1)}$  may be neglected to a good approximation. Under this approximation eqs. (2.2.60, 63-65) yield the multipole decay rates  $\lambda_{11}^{(1)}$  and  $\lambda_{22}^{(1)}$  which, in conjunction with eqs. (2.2.49-54), give the multipole relaxation cross sections  $A_{1/2}^{(1)} = A_{11}^{(1)}$  and  $A_{3/2}^{(1)} = A_{22}^{(1)}$ .

$$A_{1/2}^{(1)} = \frac{1}{N\nu\tau_1} [K_{11}^{01} - 1] + \left[ \frac{K_{11}^{01}}{1 + N\nu\tau_2(\sigma_{22}^{(0)})} - 1 \right] \sigma_{11}^{(0)} \quad (2.2.81)$$

$$A_{3/2}^{(L)} = \frac{1}{N\nu\tau_2} [K_{22}^{0L} - 1] + \left[ \frac{K_{22}^{0L}}{1 + N\nu\tau_1(\sigma_{11}^{(0)})} - 1 \right] \sigma_{22}^{(0)} \quad (2.2.82)$$

It is useful to note that the first terms of eqs. (2.2.81-82) are similar to the definitions of the Zeeman mixing cross sections which are defined in terms of the population density ratio of the collisionally- to directly-populated Zeeman substates:

$$Q(JM \rightarrow J'M') = \frac{1}{N\nu_r\tau} \frac{N_{J'M'}}{N_{JM}} \quad (2.2.76)$$

When a single Zeeman substate is optically populated, the multipole relaxation cross sections are expressed in terms of the ratios of the population density of the monopole moment to that of the multipole moment.

$$A_J^{(L)} = \frac{1}{N\nu_r\tau} \left( c \frac{n_J^{(0)}}{n_J^{(L)}} - 1 \right) \quad (2.2.83)$$

where the normalization factor  $c$  is specific to the excitation conditions and is determined by the ratio of the multipole excitation rates given in eq. (2.2.57).

I will now show that, in the limit of low pressure, eqs. (2.2.81-82) are identical to the definitions of the multipole relaxation cross sections given by Boggy and Franz (1982) and Spielfiedel et al. (1979). To this end it is useful to state the explicit form of the  $K$  coefficients in terms of the experimentally determined population ratios.



$$K_{11}^{01} = \frac{\left(1 + \frac{N_{\frac{1}{2}\frac{1}{2}}}{N_{\frac{1}{2}-\frac{1}{2}}}\right)}{\left(1 - \frac{N_{\frac{1}{2}\frac{1}{2}}}{N_{\frac{1}{2}-\frac{1}{2}}}\right)} \quad (2.2.84)$$

$$K_{22}^{01} = \frac{\left(\frac{N_{\frac{3}{2}\frac{3}{2}}}{N_{\frac{3}{2}\frac{1}{2}}} + \frac{N_{\frac{3}{2}\frac{1}{2}}}{N_{\frac{3}{2}-\frac{1}{2}}} + \frac{N_{\frac{3}{2}-\frac{1}{2}}}{N_{\frac{3}{2}-\frac{3}{2}}} + 1\right)}{\left(-\frac{N_{\frac{3}{2}\frac{3}{2}}}{N_{\frac{3}{2}\frac{1}{2}}} - \frac{N_{\frac{3}{2}\frac{1}{2}}}{3N_{\frac{3}{2}-\frac{1}{2}}} + \frac{N_{\frac{3}{2}-\frac{1}{2}}}{3N_{\frac{3}{2}-\frac{3}{2}}} + 1\right)} \quad (2.2.85)$$

$$K_{22}^{02} = \frac{\left(\frac{N_{\frac{3}{2}\frac{3}{2}}}{N_{\frac{3}{2}\frac{1}{2}}} + \frac{N_{\frac{3}{2}\frac{1}{2}}}{N_{\frac{3}{2}-\frac{1}{2}}} + \frac{N_{\frac{3}{2}-\frac{1}{2}}}{N_{\frac{3}{2}-\frac{3}{2}}} + 1\right)}{\left(\frac{N_{\frac{3}{2}\frac{3}{2}}}{N_{\frac{3}{2}\frac{1}{2}}} - \frac{N_{\frac{3}{2}\frac{1}{2}}}{N_{\frac{3}{2}-\frac{1}{2}}} - \frac{N_{\frac{3}{2}-\frac{1}{2}}}{N_{\frac{3}{2}-\frac{3}{2}}} + 1\right)} \quad (2.2.86)$$

$$K_{22}^{01} = \frac{\left(\frac{N_{\frac{3}{2}\frac{3}{2}}}{N_{\frac{3}{2}\frac{1}{2}}} + \frac{N_{\frac{3}{2}\frac{1}{2}}}{N_{\frac{3}{2}-\frac{1}{2}}} + \frac{N_{\frac{3}{2}-\frac{1}{2}}}{N_{\frac{3}{2}-\frac{3}{2}}} + 1\right)}{\left(-\frac{N_{\frac{3}{2}\frac{3}{2}}}{N_{\frac{3}{2}\frac{1}{2}}} + \frac{3N_{\frac{3}{2}\frac{1}{2}}}{N_{\frac{3}{2}-\frac{1}{2}}} - \frac{3N_{\frac{3}{2}-\frac{1}{2}}}{N_{\frac{3}{2}-\frac{3}{2}}} + 1\right)} \quad (2.2.87)$$

When the population density ratios are very small and

$$\frac{N(\frac{1}{2} + \frac{1}{2})}{N(\frac{1}{2} - \frac{1}{2})} \ll 1 \quad \frac{N(\frac{3}{2} m_j)}{N(\frac{3}{2} - \frac{3}{2})} \ll 1, \quad m_j = \pm \frac{1}{2}, \frac{3}{2} \quad (2.2.88)$$

eqs. (2.2.84-87) may be written in the form

$$K^L = \frac{(1 + \Delta n^{(0)})}{(1 - \Delta n^{(L)})} \quad (2.2.89)$$

where the population ratio sums appearing in eq. (2.2.84-87) are represented by  $\Delta n^{(0)}$  and  $\Delta n^{(L)}$ . The first-order expansion of the denominator in eq. (2.2.89) yields:

$$K^L = (1 + \Delta n^{(0)})(1 + \Delta n^{(L)}). \quad (2.2.90)$$

Neglecting second-order terms in this product, the K coefficients are now of the form

$$K^L = (1 + \Delta n^{(0)} + \Delta n^{(L)}) \quad (2.2.91)$$

which, when substituted into the first terms of eqs. (2.2.81-82), yield the relaxation cross sections in the following form.

$$\Lambda^{(L)} = \frac{1}{N\nu_r\tau} [K^L - 1] = \frac{1}{N\nu_r\tau} [\Delta n^{(0)} + \Delta n^{(L)}] \quad (2.2.92)$$

In the low pressure limit, eq. (2.2.92) describes the multipole relaxation cross sections as a linear sum of the population ratios, divided by  $N\nu_r\tau$ . According to eq. (2.2.76), eq. (2.2.92) may be expressed in terms of the Zeeman mixing cross sections;

$$\Lambda_{\frac{3}{2}}^{(1)} = 2Q\left(\frac{1}{2} - \frac{1}{2} \rightarrow \frac{1}{2} \frac{1}{2}\right) \quad (2.2.93)$$

$$\Lambda_{\frac{3}{2}}^{(1)} = 2Q\left(\frac{3}{2} - \frac{3}{2} \rightarrow \frac{3}{2} \frac{3}{2}\right) + \frac{4}{3}Q\left(\frac{3}{2} - \frac{3}{2} \rightarrow \frac{3}{2} \frac{1}{2}\right) + \frac{2}{3}Q\left(\frac{3}{2} - \frac{3}{2} \rightarrow \frac{3}{2} - \frac{1}{2}\right) \quad (2.2.94)$$

$$\Lambda_{\frac{3}{2}}^{(2)} = 2Q\left(\frac{3}{2} - \frac{3}{2} \rightarrow \frac{3}{2} \frac{1}{2}\right) + 2Q\left(\frac{3}{2} - \frac{3}{2} \rightarrow \frac{3}{2} - \frac{1}{2}\right) \quad (2.2.95)$$

$$\Lambda_{\frac{3}{2}}^{(3)} = 2Q\left(\frac{3}{2} - \frac{3}{2} \rightarrow \frac{3}{2} \frac{3}{2}\right) - 2Q\left(\frac{3}{2} - \frac{3}{2} \rightarrow \frac{3}{2} \frac{1}{2}\right) + 4Q\left(\frac{3}{2} - \frac{3}{2} \rightarrow \frac{3}{2} - \frac{1}{2}\right) \quad (2.2.96)$$

Equations (2.2.93-96) may be shown to be identical to the definitions used by Boggy and Franz (1982), Spielfiedel et al. (1979) and others. This may be done with the aid of the following relationship (2.2.97) which results from the fact that the hexadecapole-relaxation rate  $\gamma^{(4)}$  equals zero (D'Yakonov and Perel 1965). This relation is required for the comparison of the definitions, as  $Q(3/2 - 1/2 \rightarrow 3/2 - 1/2)$  is not directly obtainable from the experimental data because the  $5^2P_{3/2-1/2}$  state was not optically excited.

$$Q\left(\frac{3}{2}, -\frac{1}{2} \rightarrow \frac{3}{2}, \frac{1}{2}\right) = \frac{4}{3}Q\left(\frac{3}{2}, -\frac{3}{2} \rightarrow \frac{3}{2}, -\frac{1}{2}\right) - \frac{4}{3}Q\left(\frac{3}{2}, -\frac{3}{2} \rightarrow \frac{3}{2}, \frac{1}{2}\right) + Q\left(\frac{3}{2}, -\frac{3}{2} \rightarrow \frac{3}{2}, \frac{3}{2}\right) \quad (2.2.97)$$

Equations (2.2.81-82) have a slightly different form if the relationship between the depopulation cross sections and the fs mixing cross sections is not assumed (eqs. (2.2.43-44)) and the orientation transfer terms are not neglected. The solution for the multipole relaxation cross sections in the absence of these approximations, in terms of the K coefficients defined by eqs. (2.2.57-59), is as follows:

$$\lambda_{LL}^{(1)} = N\nu_r \tau \Lambda_{LL}^{(1)} = \left( \frac{K_{LL}^{01}(1 - K^{(0)})}{(1 - K^{(1)})} - 1 \right) (\tau_1^{-1} + \gamma_{LL}^{(0)}) \quad L=1,2 \quad (2.2.98)$$

$$\lambda_{22}^{(1)} = N\nu_r \tau \Lambda_{22}^{(1)} = \left( K_{22}^{01}(1 - K^{(0)}) - 1 \right) (\tau_1^{-1} + \gamma_{22}^{(0)}) \quad L=2,3 \quad (2.2.99)$$

Rearranging (2.2.98-99) yields the following:

$$N\nu_r \tau_L \left( K_{LL}^{01} \frac{(1 - K^{(0)})}{1 - K^{(1)}} - 1 \right)^{-1} = \frac{1}{\Lambda_{LL}^{(1)}} + N\nu_r \tau_L \frac{\sigma_{LL}^{(0)}}{\Lambda_{LL}^{(1)}} \quad L=1,2 \quad (2.2.100)$$

$$N\nu_r \tau_2 \left( K_{22}^{01}(1 - K^{(0)}) - 1 \right)^{-1} = \frac{1}{\Lambda_{22}^{(1)}} + N\nu_r \tau_2 \frac{\sigma_{22}^{(0)}}{\Lambda_{22}^{(1)}} \quad L=2,3 \quad (2.2.101)$$

It is interesting to note that an equation of identical form may be simply derived from eq. (2.1.6), describing the collisional transfer between the two fs states in the absence of a magnetic field, when the  $Z_{ab}$  are expressed in terms of their respective cross sections and quenching is neglected:

$$N\nu_r \tau \left( \frac{N_2}{N_1} \right)^{-1} = \frac{1}{Q_{12}} + N\nu_r \tau \frac{Q_{21}}{Q_{12}} \quad (2.2.102)$$

A cross section may be regarded as a measure of the probability for a particular collisional transfer process. While the cross sections themselves are pressure-independent, the measured population ratios are not linear with pressure under conditions involving multiple collisions. It is only at pressures where the population ratios

are sufficiently small ( $<0.01$ ) that eqs. (2.2.81-82) and the theoretical definitions of the multipole relaxation cross sections given by (2.2.93-96) are in good agreement. Equations (2.2.100-102) have been written in the form  $Y=A+BX$  where  $X$  is proportional to the pressure and  $A$ , the low pressure intercept of a plot of  $Y$  against  $X$ , is the inverse of the relaxation cross sections and the slope  $B$ , the ratio of the depopulation cross section to the relaxation cross section, is a measure of the rate at which the multipole density distributions come to equilibrium with increased collision rates. The equations, when written in this form, define the relaxation cross section to be a pressure independent measure of the collisional relaxation process and are therefore consistent with equations (2.2.93-96). It should be noted that  $K^{(0)}$  and  $K^{(1)}$ , are second-order terms which vanish at low pressure, justifying the expansion of eqs. (2.2.81-82) in terms of the first order term  $K^{(2)}$ .

In this investigation the population ratios were determined under almost single collision conditions:  $Nu, Q(Jm \rightarrow J'm')\tau \leq 0.3$ . Because the 'single collision condition' was only weakly satisfied, the use of equations (2.2.81-82, 100-101) would seem most appropriate for the calculation of the multipole relaxation cross sections. However, it is also apparent from equations (2.2.84-87), that eqs. (2.2.81-82, 100-101) involve the manipulation of a larger number of population ratios, with their associated experimental errors, than do eqs. (2.2.93-96). The smaller propagation of experimental error inherent in eqs. (2.2.93-96) provides an argument in favour of using these equations for the calculation of the multipole relaxation cross sections and outweighs the error associated with the imperfect fulfillment of the single collision condition.

### 2.3 The Radiative Lifetimes of the Potassium 5P, 6P and 7P States

The time evolution of the population of an excited atomic state is governed primarily by the process of radiative decay. When stimulated emission, absorption and quenching are negligible, the probability of decay from an initial state  $i$  to a final state  $j$  is described by the Einstein coefficient  $A_{ij}$ . The total probability  $A_i$  for the transition out of the excited state  $i$  by spontaneous emission, is given by the sum of the  $A_{ij}$  coefficients over all the final states.

$$A_i = \sum_j A_{ij} \quad (2.3.1)$$

An allowed electric dipole transition from state  $i$  to a state  $j$  is governed by the following selection rules

$$\Delta l = \pm 1, \Delta J = 0, \pm 1 \quad (J=0 \nrightarrow J=0) \quad (2.3.2)$$

$$\Delta m_j = 0, \pm 1 \quad (m_j = 0 \nrightarrow 0 \text{ if } \Delta J = 0) \quad (2.3.3)$$

The time evolution of the excited state population  $N_i$  decaying by spontaneous emission is given by

$$\frac{dN_i}{dt} = -A_i N_i(t) \quad (2.3.4)$$

which has the solution

$$N_i(t) = N_i(0)e^{-A_i t} \quad (2.3.5)$$

where  $N_i(0)$  is the initial population of the state.

The lifetime  $\tau$  of the excited state is given by the reciprocal of the Einstein  $A_i$  coefficient.

$$\tau = \frac{1}{A_i} = \sum_j A_{ij}^{-1} \quad (2.3.6)$$

The total fluorescence intensity emitted in the decay of the excited state is divided between the transitions to the various possible final states. In this experiment, where only a single transition was observed, the time evolution of the fluorescence was governed by the population of the excited state which decayed at a rate defined by  $A_i$ ; the intensity  $I(t)$  of the observed fluorescence was given by  $N_i(t)A_{ij}$ .

### 3 THE APPARATUS AND EXPERIMENTAL PROCEDURES

#### 3.1 The Apparatus and Procedure Used in Fine-structure and Zeeman Mixing Experiments

A schematic diagram of the apparatus is shown in figure (3.1). The apparatus was used for the determination of the fs mixing cross sections in zero magnetic field and the Zeeman mixing cross sections at a field of 70 kG. The following description will be mainly relevant to the Zeeman mixing experiment with particular differences pertaining to the fs mixing experiment pointed out when appropriate.

Potassium atoms, mixed with a noble gas and contained in a fluorescence cell located at the center of a superconducting solenoid, were irradiated with pulses from a  $N_2$  laser ( $N_2L$ ) -pumped dye laser (DL) which excited one of the  $KS^2P_{1/2-1/2}$ ,  $KS^2P_{3/2-3/2}$  Zeeman substates. The resulting polarized fluorescence, monitored at right-angles to the direction of excitation and parallel to the magnetic field, consisted in each case of a direct fluorescence component emitted in the decay of the optically excited state, and sensitized components emitted from the collisionally populated Zeeman substates of the 5P manifold. The fs mixing experiment was carried out in the absence of a magnetic field, the fluorescence was not polarization analyzed and the individual  $S^2P_{1/2}$  and  $S^2P_{3/2}$  fs states were selectively excited.

The output from the dye laser was condensed into an optical fibre and conveyed to the fluorescence cell where a termination consisting of a lens and mirror directed a parallel beam 3mm in diameter into the cell at right angles to the direction of observation. The circularly polarized fluorescence was collected by a lens, rendered parallel,

passed through a quarter-wave plate (manufactured by Meadowlark Optics for 405.5 nm (the centre of the fluorescence doublet)) followed by a linear analyzer (Polaroid HN38) and was made incident on the mirrors of a piezoelectrically scanned Fabry-Perot interferometer (FP). The interferometer output was focussed onto the photocathode of an ITT FW130 refrigerated photomultiplier (PM1) (operated at 1800 V) whose output pulses were amplified by an Ortec 9302 amplifier-discriminator (AMP) and transferred to an in-house built inverter-amplifier (50 MHz maximum count rate) with a gated detection window (GATE); its standard TTL output pulses (20 ns pulse width) were accumulated in a multichannel scaler (MCS). To avoid detecting scattered laser light, the amplifier was gated-on by the signal from a fast photodiode which monitored the dye-laser output. The amplifier operated in a time window starting from the gate-on pulse through 1400 ns (approximately 10 lifetimes of the 5P state). The experimental data were corrected for this time delay (see section 3.1.4). The MCS channel advance was synchronized to the interferometer sweep and thus the recorded spectra may be regarded as interferograms, digitized in wavelength resolution and intensity.

The fluorescence count rate was adjusted to produce 1-2 counts per MCS sweep (35 laser pulses) by varying the output power of the nitrogen laser as well as the degree of focussing of the exciting laser beam into the optical fibre. The count rate was frequently checked and adjusted to keep it constant as the laser dye (DPS) deteriorated. The excitation wavelength was periodically changed to alternate between the Zeeman states or two fs states; the resulting fluorescence signals were stored in different sections of the MCS memory.



The spectra accumulated in the MCS were transferred to a Commodore Pet2001 computer for further analysis and final plotting. The plots, corrected for background noise, were analyzed to determine the integrated intensities of the individual Zeeman fluorescence peaks. This information was used, with the appropriate Einstein A coefficients, to obtain the population ratios of the collisionally-to-radiatively populated Zeeman substates in relation to the buffer gas pressure. After correcting for the time delay between optical excitation and fluorescence detection, these data yielded the Zeeman mixing cross sections as well as the multipole relaxation, fs mixing, and orientation transfer cross sections.

This technique was first used to determine the fs mixing cross sections in zero field which did not require extremely high resolution as the spectrum consisted of only two fluorescence components. A measurement of the Zeeman mixing cross sections was first attempted at 37.5 kG, however the resolution of the individual Zeeman peaks was unsatisfactory. The extensive fs mixing of the 5P state (due in part to its small fs splitting of  $18.75 \text{ cm}^{-1}$ ) required the full resolution of the six Zeeman components, emitted from both fs levels. The experiment was then modified to obtain better resolution. This was accomplished by operating at 70 kG, at which the Zeeman splitting was larger and by separating the left- and right- circularly polarized fluorescence components with a circular analyzer, effectively increasing the resolution by factor of four. The  $\text{N}_2$  laser, which generated considerable electrical noise, was relocated 15m away from the detection equipment, reducing the shot noise to barely detectable levels and the single grating dye-laser oscillator was replaced with a double grating design with a narrower bandwidth (see section

3.2). The dye laser tuning arm was modified to include a piezoelectric transducer<sup>2</sup> which facilitated the fine-tuning of the laser to the selected Zeeman transition.

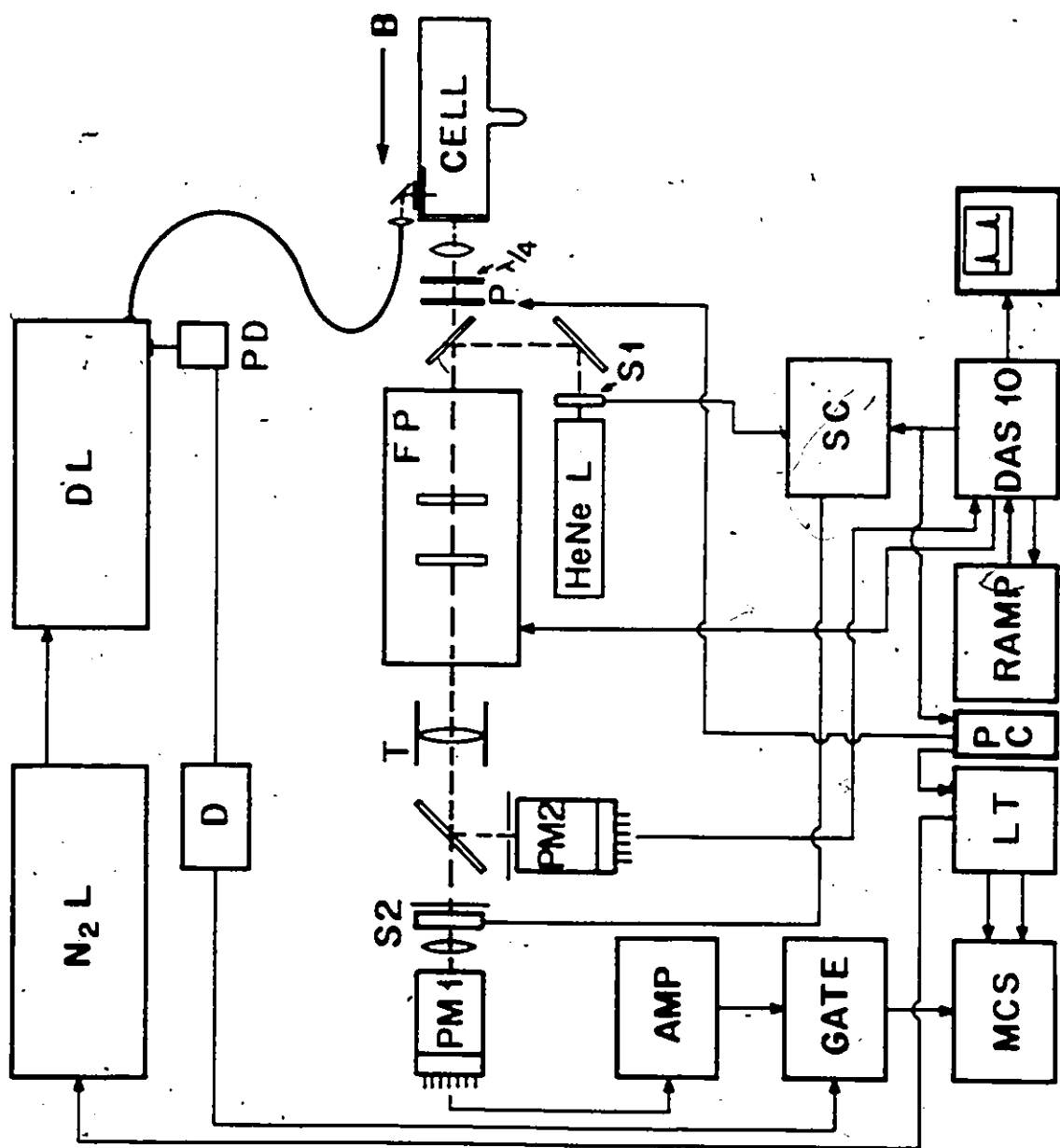
The identification of the spectral components was accomplished by means of sequential optical excitation of the individual Zeeman substates. The dye-laser was calibrated with a thermionic diode (see section (3.1.5)) and its setting was calculated for each Zeeman substate (see Appendix A). The Zeeman substates were then optically excited in turn, starting with the lowest energy state; the highest fluorescence peaks in these spectra (see for example Figs. (4.2.2-3)) correspond to the fluorescence emitted from the directly excited Zeeman substates. It was possible to selectively populate substates using laser wavelengths corresponding to their  $\pi$  transitions, but it was not possible to observe the direct  $\pi$  fluorescence with the detection geometry which was employed in the experiments.

---

<sup>2</sup> The piezoelectric elements were taken from two barbecue lighters supplied by the Canadian Tire Corp.  $\pm 5 \times 10^{-6}$  m displacement with a  $\pm 2500$  V bias.

Figure (3.1) Schematic arrangement of the apparatus for fine-structure and Zeeman mixing.

N<sub>2</sub>L, nitrogen laser; DL, dye laser; PD, photodiode; D, delay line; A, vacuum and gas filling system; FP, Fabry-Pérot scanning interferometer; T, telescope; PM, photomultiplier tubes; S1, S2, shutters; AMP, amplifier-discriminator; GATE, gated pulse-inverter amplifier; LT, channel advance and laser trigger controller; SC, shutter controller; PC, polarizer controller; P, circular polarization analyzer. B indicates the 70 kG magnetic field.



### 3.1.1 The Fluorescence Cell, Oven and Vacuum System

The quartz cell had a square cross section (2.5X2.5X4.0 cm) and was fitted with a 1 cm long sidearm protruding downwards, which contained a small quantity of potassium metal. The cell was connected to the vacuum system through a 2 mm (ID) capillary tube and a greaseless teflon stopcock. The cell and the sidearm were mounted in an oven located in a brass tube extending 0.5 m from the mounting of the vacuum system into the bore of the superconducting solenoid. The oven surrounding the cell was made of thick copper plates containing channels through which silicone oil was circulated. The sidearm oven, mounted beneath the main oven and insulated from it, consisted of windings of narrow-bore copper tubing in thermal contact with the sidearm of the cell, through which silicone oil was circulated. The heated silicone oil was supplied by two Neslab thermostats, one controlling the sidearm temperature and the other controlling the temperature of the main oven.

The temperatures of the cell and of the main oven were monitored with 5 copper-constantan thermocouples located at various points on the cell and referenced to the triple point of water (273.16 K). The temperature stability was  $\pm 0.5$  K over a period of 6-8 hours, as long as the room temperature remained reasonably stable.

The vacuum system consisted of an Edwards 2" diffusion pump backed by an Edwards EM2 forepump. Back streaming of pump oil was minimized by a chevron baffle and a liquid nitrogen (LN) cold trap. The gas-filling system consisted of pyrex bottles of research-grade gas supplied by the Linde company, separated from the vacuum system by individual teflon stopcocks as well as a main stopcock and a microleak valve which was used to admit controlled quantities of gas

to the cell. Gas pressures were measured with an MKS Baratron capacitance gauge (0-1 torr, full scale precision 5 parts in  $10^5$ ).

Before beginning the experiment the entire glass vacuum system was repeatedly flame heated to remove impurities on the glass surfaces. The ultimate vacuum attainable by the system was of the order of  $7 \times 10^{-8}$  torr. Before each experimental run, the fluorescence cell was pumped down to about  $5 \times 10^{-7}$  torr and isolated from the vacuum system. For a period of about 12 hours, the main oven was kept at  $116^\circ\text{C}$  and the sidearm at  $15^\circ\text{C}$  to ensure the condensation of all the potassium in the sidearm. The cell was then reopened and evacuated for 1-2h with the sidearm at  $74^\circ\text{C}$  in the case of the zero-field fs mixing experiment and at  $94.5^\circ\text{C}$  for the Zeeman mixing experiment (this corresponds to a K vapour pressure of  $1 \times 10^{-5}$  torr at which radiation trapping is insignificant (see section 4.3)). During this time the nitrogen laser and other systems were aligned and stabilized. The laser was tuned to excite the selected fs state at 4044 or 4047 Å by observing the fluorescence produced in an auxiliary high temperature cell containing potassium vapour. Tuning of the dye-laser to the selected Zeeman level was done by calibrating the tuning assembly with the aid of the thermionic diode and fine-tuning with the piezoelectric transducer. The fluorescence cell was then flushed with clean buffer gas, pumped down again and finally filled with buffer gas at the required pressure, allowed to come to equilibrium and isolated from the vacuum system.

### 3.1.2 The Superconducting Magnet

The superconducting magnet, an Oxford Instruments (Mod.s7/123/1) superconducting solenoid (NbTi), was capable of generating magnetic fields up to 70 kG with a specified homogeneity of 1% within 11 mm of the centre of the coil along its axis. The solenoid had a room temperature access bore in which the potassium cell and oven assembly was placed.

The slight non-uniformity of the field had no significant effect on the experiment as the field variation over the volume of fluorescing vapour ( $10 \text{ mm}^3$ ) was negligible. Test measurements of the field variation were made with a Bell Incremental Gaussmeter fitted with a Hall effect 10X reducer probe. At 50 kG the axial field variation within 10 mm of the solenoid centre along the axis, was found to be at most 25 G, corresponding to a homogeneity of 0.05 % over this region. The bandwidth of the laser (4 GHz) was sufficient to excite any atom in the excitation volume with this field variation, but sufficiently narrow to cause no overlap of optical excitation to other Zeeman substates.

The magnet assembly consisted of a 100-l LN reservoir connected to a lower 30-l LH reservoir surrounded by a vacuum containment vessel and several internal heat shields. The LH boil-off rate was found to be approximately 4L/day and thus it was necessary to refill the magnet every 7 days in order to avoid complete depletion of LH, which would then require a warm restart of the magnet. The LH level had to be maintained at a minimum of 10% to reduce the possibility of a field quench which would take place if the superconductivity were lost with full current through the coil (56.3 A was required to generate 70 kG).

Several attempts were made to lower the boil off rate. The external electrical solenoid contacts were continuously cooled with LN, but this had no noticeable effect on the boil off rate. The only success in slowing the evaporation rate of the helium was achieved by pumping on the LN exhaust ports with a rotary pump. With a pressure of 220 torr above the LN, a temperature of 67 K was obtained (the temperature of LN at atmospheric pressure is 77 K). Temperature measurements were made with a copper-constantan thermocouple referenced to LN at atmospheric pressure. Care had to be taken when refilling the LN reservoir because the vacuum, created when 'warm' nitrogen vapour condensed on the colder pumped LN surface, tended to draw air and water vapour into the tanks. Care also had to be taken to avoid freezing the LN (63 K), as solid nitrogen is a good insulator. The estimated LN boil-off-rate reduction amounted to only 1.5%.

The magnet was mounted on a wheeled platform which moved on rails fixed to the concrete floor. This arrangement, which was made possible by the light weight of the magnet (100kg empty), allowed easy access to the oven and cell assembly for the occasional alignment of the optical components normally positioned at the centre of the solenoid, also permitted the magnet to be moved to a location with greater overhead clearance required when filling with LH. An additional advantage of this design was that the vacuum system remained rigidly fixed.



### 3.1.3 The Interferometer and Synchronization System

A Burleigh Mod. 110 scanning interferometer was used to resolve the Zeeman fluorescence. An analogue high voltage ramp, applied to the piezoelectric transducers attached to one mirror, produced repetitive scans through several interference orders. This instrument, fitted with broadband  $\lambda/200$  mirrors having an average reflectivity of  $94 \pm 2\%$ , had a finesse of 30 and a free spectral range of  $12.5 \text{ cm}^{-1}$ .

The alignment of the interferometer was very sensitive to vibrations and temperature shifts which, if uncompensated, cause changes in the alignment of the mirrors and thus in the free spectral range, and also decrease the resolving power of the instrument. Thermal instabilities in the laboratory were buffered by a temperature-controlled enclosure which compensated for slow changes of several degrees. Vibrational effects, which are particularly large on the upper floor of the building, were reduced by loading the interferometer table with cement slabs and placing rubber pads under the table supports. These attempts to stabilize the interferometer were partially successful, but the stabilization problems were finally solved with the aid of the Burleigh DAS-10 stabilization system. This instrument actively corrected the interferometer alignment by locking it to a He-Ne laser interference pattern. The DAS-10, coupled to the ramp generator, sampled this interference pattern in a particular time 'window' of the scan and adjusted the spacing and alignment of the interferometer cavity to maintain the He-Ne peak within this window at a maximum peak amplitude (finesse). The instrument maximizes the finesse through an automatic procedure of trial and error test steps, adjusting the bias voltage to one of the three piezoelectric stacks fixed to

the scanning mirror and then observing the resultant increase or decrease in finesse or alignment. If the finesse diminishes as a result of the voltage test step, the test step is then applied in the opposite direction, or to a different stack. This automatic alignment resulted in a stable average fringe pattern with a high average finesse. The test step amplitude was kept as small as possible to decrease the resulting slight broadening of the spectra. The system worked well at scanning frequencies of 0.5 Hz or higher, and this lower limit was chosen for the experiment.

An electromechanical system was developed to synchronize the analogue scanning of the interferometer with the firing of the pulsed dye laser. This was done in such a way that the fluorescence, resolved with a polarization analyzer and the interferometer after each laser pulse, could be detected and stored in the memory of the MCA, synchronized with the interferometer spacing. The DAS-10 was also interfaced to the scan of the interferometer in order that the He-Ne laser light could be passed through the optical path of the instrument in the time window required for the alignment test step without interfering with the fluorescence detection (this was accomplished with the aid of two mechanical Optikon leaf-shutters). The analogue high voltage ramp generator and the DAS-10 formed the nucleus of the synchronization system. A trigger pulse was produced by the ramp generator at the beginning of each scan and was sent to the shutter controller, the polarizer rotator, and the MCA start and channel advance controller.

The shutter controller opened and closed the shutters in sequence. The first, when open, allowed a parallel beam of He-Ne laser light to pass through the interferometer. The transmitted signal was detected with a photomultiplier (PM2), amplified by a high speed picoammeter and directed to

(

the DAS-10 stabilizer which used this signal to align the interferometer. This operation took approximately 150 ms after which the shutter was closed and the second shutter opened. The second shutter, located in front of the photomultiplier which detected the fluorescence, was open for the remainder of the two second duration of the ramp.

The fluorescence first passed through a quarter wave plate which converted the two circularly polarized fluorescence components to linearly polarized light. These components were then directed through a rotatable linear analyzer, which changed orientation with every trigger pulse. The analyzer assembly included a high speed stepper motor (80 ms per rotation) which rotated a set of polarizers mounted on a platform. The polarizers were set perpendicular to one another and aligned at 45° to the horizontal to avoid any polarization bias to the light transmitted through the two beam splitters further along the optical path. These beam splitters were mounted so that the rotation axis was aligned for one beamsplitter with the horizontal and for the other with the vertical. The fs mixing experiment carried out in zero field did not require the polarization analyzers. The MCA was triggered by a pulse derived from the polarizer rotator after every second rotation to ensure that the polarization components registered by the MCA were always in the same order.

The MCA start and channel advance controller (LT) synchronized the firing of the nitrogen laser with the channel advance of the MCA. The MCA recorded the fluorescence in 512 channels, the first half of which recorded the  $\sigma$  components and the second half the  $\sigma'$  components. Thus two interferometer scans were recorded before the MCA was ready to accept the next start pulse. In order to collect fluorescence in each channel during a scan,

the laser would have to fire at 128 Hz. Since the laser was limited to frequencies not exceeding 40 Hz (if one wished to obtain a stable, repetitive power output), the MCA channel advance controller was programmed to interleave the channels; during each scan only every fourth channel registered the PM signal. This scheme allowed the laser to be fired at 32.5 Hz and all MCA channels to register a signal after 4 MCA scans. Several channels were not used for the registration of fluorescence signals as they were located in the time window in which the polarizers were rotated and the DAS-10 was in operation. After sufficient fluorescence signal had been accumulated, the MCA data were transferred to the PET2001 computer and the dye-laser tuned to the other excitation wavelength.

#### 3.1.4 The Effect of Gating on the Measured Fluorescence Intensity Ratios

To obtain accurate values of fluorescence intensity ratios and thus of the cross sections, the measured intensity ratios had to be corrected for the effects of gating which was described in section 3.1. The most obvious result of gating the detection system (besides dramatically improving the signal to noise ratio) is to artificially enhance the ratio of the sensitized-to-direct fluorescence. The sensitized fluorescence is derived from the excited states whose populations, initially zero, gradually increase through collisional excitation transfer and decrease through spontaneous decay. The direct component is derived from the directly excited level whose population immediately begins to decrease through spontaneous decay and collisional transfer.

The fs mixing experiment (zero field) had a delay of 8 ns and the multipole relaxation experiment had a delay of 30 ns. The theoretical analysis of the two experiments (discussed in section 2.1 and 2.2) assumes a time-integration period extending from 0 to  $\infty$ .

In practice, the integration time extended from the gate-on time of the amplifier through the data accumulation period of 1400 ns (roughly 10 lifetimes of the 5P state).

$$\int_0^{\infty} \dot{N} dt = \int_{t_g}^{10\tau} \dot{N} dt. \quad (3.4.1)$$

A computer simulation of the time evolution of the excited state population density was developed to test the validity of this approximation.

The change in the population of the  $i$ -th Zeeman substate  $dN_i$ , due to optical excitation, radiative decay and collisional excitation transfer in a time interval  $dt$  may be expressed as follows:

$$dN_i = \left( S_i - N_i/\tau - \sum_{j \neq i} N_i Z_{ij} + \sum_{j \neq i} N_j Z_{ji} \right) dt \quad (3.4.2)$$

where  $S_i$  denotes the excitation rate of the  $i$ -th level which was modeled by the function  $S_i = A \sin(\pi t/10)$  describing the time evolution of the 8 ns (FWHM) laser pulse (Pace and Atkinson, 1974).  $N_i$  is the population of the  $i$ -th level and  $Z_{ij}$  are the collision rates. Quenching has been neglected in eq.

(3.4.2) (see section 2.1). The experimental data were used to determine a first approximation of the collision numbers for the collisional transfer between the Zeeman substates. These numbers  $Z_{ij} = Z(j, m \rightarrow j', m')$  were related to the average Zeeman mixing cross sections calculated from experimental integrated fluorescence intensities determined from the areas under the peaks in the spectra:

$$Z_{ij} = N \nu_r Q(i \rightarrow j) = \frac{1}{\tau} \left( \frac{I_j^o}{I_i^o} \right) \left( \frac{A_i^o}{A_j^o} \right). \quad (3.4.3)$$

As it was only necessary to excite the  $5^2P_{1/2-1/2}$  and the  $5^2P_{3/2-3/2}$  state in order to determine all the multipole relaxation rates, not all the  $Z_{ij}$  were determined independently. Most of the collision rates were obtained directly from the experimental data assuming the symmetry relationship  $Z(j, m \rightarrow j', m') = Z(j, -m \rightarrow j', -m')$  (Boggy and Franz, 1982). It was also assumed that the reverse process  $Z(j, m \leftarrow j', m')$  was related to the forward process through the principle of detailed balancing. In this manner all but six of the rates were determined. The remaining six were approximated by various sums and differences of the known

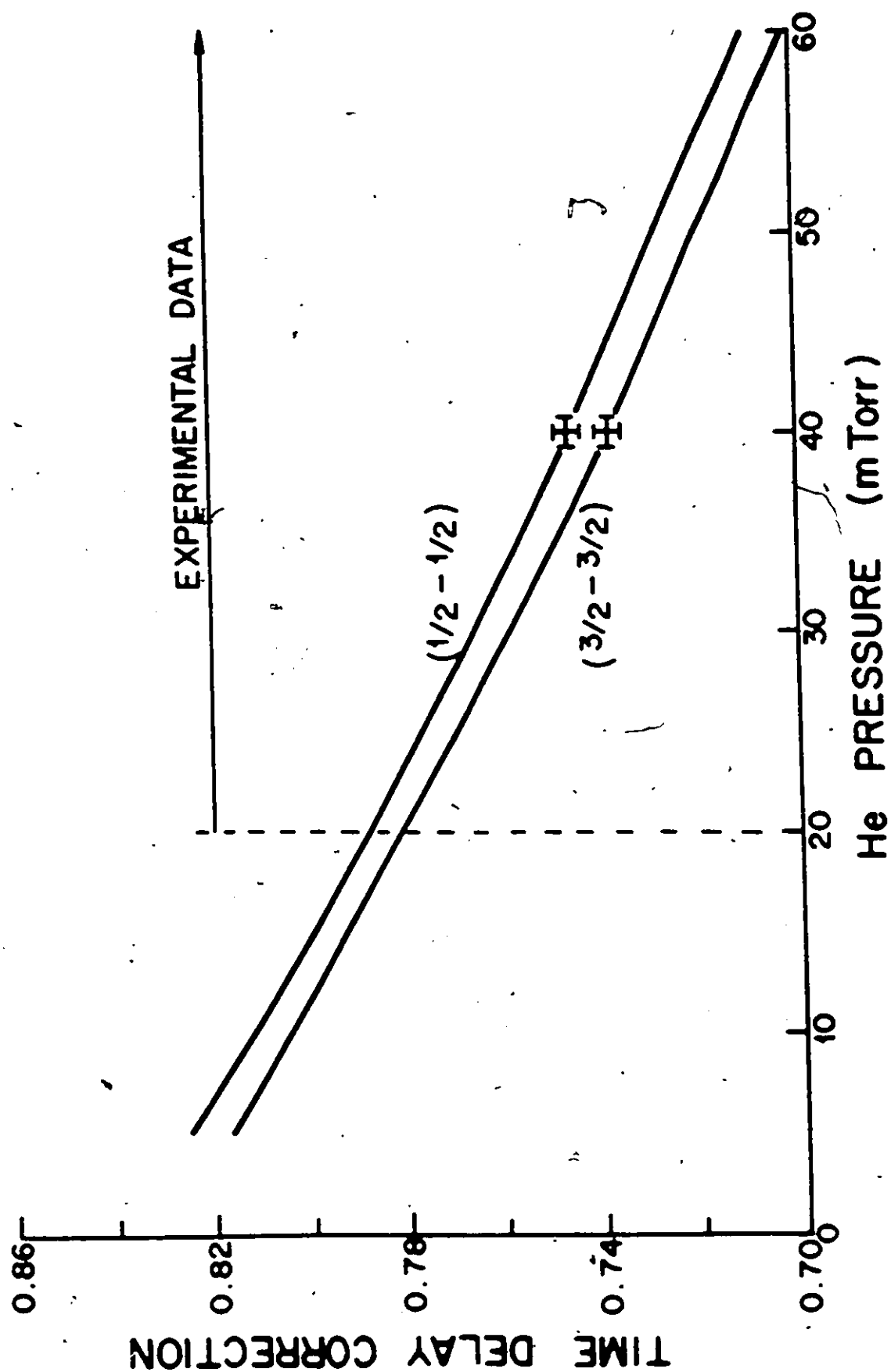
rates. The validity of these approximations was evident in the noticeable lack of sensitivity of the final correction factors to moderate variations in these collision numbers although the correction factors were pressure dependent.

The computer simulation produced the sensitized-to-direct fluorescence ratios for the three following cases: (1) cw excitation with zero time delay; (2) Pulsed excitation with zero time delay; (3) Pulsed excitation with 30 ns time delay. As expected, cases (1) and (2) produced nearly the same ratios while the comparison of the population ratios determined in case (3) to the population ratios determined in case (1) provided the factors needed to correct the measured intensity ratios. The final average correction factors are  $0.74 \pm 0.04$  for  $S^2P_{3/2-3/2}$  excitation and  $0.75 \pm 0.04$  for  $S^2P_{1/2-1/2}$  excitation. These factors correspond to gas pressures midway between the experimental pressure limits, and were applied to the measured fluorescence intensity ratios. The error associated with the correction factors represents their predicted variation over the pressure limits used in the experiment, and a plot of this variation is shown in figure (3-1.4) for He (the correction factor variation from one gas to another was within the stated error).

Figure (3.1.4)

A plot of the time delay correction factor against  
He pressure.





### 3.1.5 The Design and Operation of a Potassium Thermionic Diode

The thermionic diode (TD) was developed to make possible the accurate setting of the dye-laser wavelength for the excitation of various transitions in potassium. The operating principle of this device is similar to that of a Geiger counter. Pulsed laser light, focused into the K vapour between the electrodes, induces photoionization when the laser wavelength coincides with an atomic transition. The resulting ions, accelerated by the electric field applied between the electrodes, gain sufficient kinetic energy to collisionally ionize the buffer gas atoms and create an avalanche resulting in the amplification of the initial ion current.

The TD consisted of a cylindrical glass tube 14 cm long and 2.5 cm in diameter fitted with two metal feed-throughs which were connected to the internal anode and cathode, and a sidearm 4 mm in diameter and 1 cm long which contained a small quantity of K. The cylindrical cathode consisted of a 3 cm long Al tube 1 cm in diameter and the anode needle was centred in it. Argon was added to sustain the diode operation. Several diodes were constructed with buffer gas pressures ranging from 20 mtorr to 20 torr. All the models worked, although the operating characteristics (especially voltage) were different. The best model contained 2 torr of argon and was operated at 50 V (just below the voltage required for glow discharge). The diode was housed in an electrically heated oven which produced a maximum temperature of 230° C. The sidearm temperature was held at about 15° C below that of the TD to avoid condensation on the input window.

To produce maximal sensitivity, the excitation region was located between the electrodes, but the capability for fs resolution was not as good as in a Doppler-free shielded TD where the excitation region takes place in a field-free region; this eliminates Stark and Zeeman broadening and has been found useful in doppler-free two-photon absorption investigations (Harvey 1981, Niemax and Weber 1978).

✓ An oscilloscope, triggered by a fast photodiode, was used to monitor the potential across a 2 M $\Omega$  resistor connected in series with the TD electrodes. When the laser was tuned to an atomic transition, a voltage spike, nominally 100  $\mu$ s in width and having an amplitude up to several volts, resulted from the 8 ns input laser pulse. The output pulse height depended on the diode temperature (K density) and voltage as well as the oscillator strength of the transition. It was possible to observe a voltage spike for the 4S-5P transition even in the absence of a potential difference across the electrodes, but the 4S-4D transition, with its anomalously low oscillator strength, was barely observable under the most favourable conditions. The transitions which could be readily detected are listed in table (3.5).

The TD facilitates simple and quick dye-laser tuning to 'hard to find' transitions in K and has been used for the calibration of the dye-laser. The optogalvanic effect in Ne and Ar discharge lamps (Nestor, 1982) has also been used for this purpose although these optogalvanic signals tend to be more difficult to observe because of electrical noise and discharge lamp oscillations.

Table (3.5) Excited States Detected with the Potassium Thermionic Diode

<u>EXCITED STATE</u>	<u>EXCITATION</u>	<u>WAVELENGTH</u> (nm)
$5^2S$	Quadrupole	475
$6^2S$	Two photon	728
$7^2S$	Two photon	661
$8^2S$	Two photon	630
$9^2S$	Two photon	613
$5^2P_{1/2,3/2}$	Dipole	404.721 404.414
$6^2P_{1/2,3/2}$	Dipole	344.738 344.637
$7^2P_{1/2,3/2}$	Dipole	321.762 321.716
$8^2P_{1/2,3/2}$	Dipole	310.2
$9^2P$	Dipole	303.4
$10^2P$	Dipole	299.2
$3^2D_{1/2,3/2}$	Two photon	464.68 464.24
$5^2D$	Two photon	662.6
$6^2D$	Two photon	631

### 3.1.6 A Fizeau Wavemeter with Single-Mode Optical Fibre Coupling

The Fizeau wavemeter is one of the most promising devices for measuring the wavelength of both cw and pulsed dye lasers with an accuracy comparable to the linewidth produced by most pulsed lasers. Most wavemeters for use with pulsed lasers use a spatial filter with a metallic pinhole which is susceptible to damage caused by the high power density. Diamond pinholes, which can withstand high powers, have inherent drawbacks due to the translucence of the material and to the limited range of available pinhole sizes which are rather large. The present design utilizes a single-mode optical fibre coupling which overcomes these difficulties as well as the problem of input-beam alignment. The fibre coupling is more convenient and easier to use than the spatial pinhole as the input fibre can easily be aligned with the input laser beam while the fixed pinhole design requires the laser beam to be aligned with the wavemeter.

#### a Principle of Operation

The laser light entering the wavemeter is spatially filtered by a single-mode fibre which creates a beam with a spherical wave front. This is made incident on an off-axis parabolic mirror which produces a wide and well-defined parallel beam having a gaussian intensity profile, and directs it onto a wedge consisting of two fused silica interferometer plates. After reflection from the wedge, the beam now consists of two coherent parts almost parallel to each other, which produce a Fizeau interference pattern; the fringes are registered by a photodiode array interfaced to a computer. The wavelength of the incident laser light is

determined from the spacing and phase of the fringe pattern. The approximate value of the wavelength  $\lambda_0$  is obtained from the expression (Morris et al., 1984):

$$\lambda_0 = 2p\alpha \quad (3.6.1)$$

where  $p$  = fringe-spacing and  $\alpha$  = wedge angle. The optical path difference (opd)  $\Delta d(x)$ , corresponding to a fringe minimum chosen for reference at a value  $x$  along the interference pattern, is calculated from the wedge spacing and the wedge angle, and yields the interference order  $N$  of this fringe (Lu and Wu, 1984):

$$N = \frac{\Delta d(x)}{\lambda_0} \quad (3.6.2)$$

where  $N$  is rounded-off to the nearest integer (a phase shift of  $\pi$  is introduced in the beam reflected from the inner wedge surface). The final value of the wavelength  $\lambda$  can then be determined with an accuracy limited by the error in the measurement of the wedge-spacing:

$$\lambda = \frac{\Delta d}{N} \quad (3.6.3)$$

#### **b Details of Construction**

The optical layout of the wavemeter, is shown in fig. (3.2), is similar to that proposed by Morris et al. (1984). All optical components, except the precision fibre coupler, are mounted on a 4-cm thick aluminum plate placed inside an aluminum vacuum chamber maintained at 2 Pa.. Laser light is spatially filtered by focusing it onto the 4  $\mu m$  core of a F-SV Newport single-mode fibre with the aid of the external fibre coupler, and is formed into a parallel beam by reflection from the surface of a 20 cm focal length 21° off-axis parabolic mirror. The parallel beam is reflected from the two inner uncoated Fizeau wedge surfaces and the

resulting interfering components are focused by a cylindrical lens of 5 cm focal length onto a 2.5 cm long 1024-element photodiode array (RETICON RL1024H) placed at the zero-shear position (Snyder, 1981). The fibre optic cable ends must be properly cleaved in order to yield a high quality output beam and allow proper focusing into the fibre. The input fibre end is susceptible to mechanical damage and power damage caused by too tight focussing of the input beam into the fibre. If the wavemeter is tested with a He-Ne laser and alignment or focussing into the fiber is difficult, this is a good indication that the fiber input end is damaged. This damage is readily repaired by re-cleaving the input end and an excess of fibre was left inside the vacuum chamber to allow for this. The fibre was fed into the chamber through a small pinhole made in a rubber membrane. The membrane was then compressed with a pressure plate to ensure a tight vacuum seal. To lengthen the external fibre, the excess fibre inside must be unwound by opening the top plate and the pressure plate loosened after which the fibre may be carefully pulled through.

The Fizeau wedge was manufactured (by Interoptics Ltd. of Ottawa) of optically contacted quartz components. The wedge plates were flat to  $\lambda/20$ , inclined at an angle of  $5.5364 \times 10^{-4}$  rad, and separated by a quartz wedge ring with a spacing of 1 mm. The outer surfaces of the plates were antireflection coated for visible light while the 'active' inner plate surfaces were uncoated. We decided to use uncoated wedge surfaces in order to avoid fringe shift and asymmetry (Rogers 1982) and to eliminate the spectral dependence of the finesse due to the coating bandpass characteristics.

The temperature of the aluminum plate was maintained at  $305 \pm 0.5\text{K}$  and the vacuum chamber was maintained at  $301 \pm 0.5\text{ K}$  using two temperature controllers of the same type as that used to stabilize the Burleigh scanning interferometer. Without temperature stabilization a very small systematic wavelength drift was observed of one part in  $10^7$  per degree temperature change of the aluminum plate. The temperature stabilization must be kept on constantly because of the large thermal capacity of the instrument which delays the establishment of a thermal equilibrium. The electronic data acquisition system is shown schematically in Fig. (3.3). The optical signal, registered by the RETICON RL1024H monolithic self-scanning linear photodiode array, is converted into a series of electric pulses which are sampled and held by a sample-and-hold amplifier, and are then digitized with  $0.8\text{ }\mu\text{s}$  conversion speed by an 8-bit ADC, loaded into a 1K memory buffer and finally transferred to an IBM XT computer. An additional variable amplifier was later added between the Reticon array and the ADC and adjusted to ensure that the largest possible signal from the Reticon array (corresponding to the output signal just below the optical saturation point) used the full 8-bit resolution of the ADC. The fringe data processing and wavelength calculation is performed using the algorithm of Snyder (1980) in a Turbo Pascal program at a rate of about 1 Hz (higher speeds are possible with minor modifications to the computer and electronic hardware). The power requirement is about 0.01 mW for a TEM00 cw laser source and about  $2\text{ }\mu\text{J}$  energy per pulse for a pulsed laser source. At high power densities, particularly for the case of pulsed laser wavelength measurement, one can expect the generation of Stokes-shifted wavelengths in the fibre due to the nonlinear susceptibility of the optical material, which may lead to unexpectedly large errors in the calculated wavelengths. In



order to estimate and minimize these errors we reduced the power entering the optical fibre by a factor of about fifty and allowed the photodiode array to accumulate and integrate the signal of 50 pulses before each scan of the array. This procedure gives an average wavelength of 50 laser pulses but with a negligibly small contribution from Stokes-shifted wavelengths. Both the single shot or the 50 pulse average method produced the same wavelength measurements under normal input powers, indicating that Stokes-shifted wavelength generation in this fibre was negligible at the power densities employed. As long as the input power is not so high that it saturates the photodiode array or too weak to be registered, the instrument yields reproducible repetitive measurements. High input power densities can easily be compensated by reducing the input focussing into the fibre. When measuring weak signals the resolution capability of the ADC cannot be fully used, and this leads to lower accuracy because of increased round-off errors by the ADC. Increased accuracy of the wavelength measurements could be obtained with a higher resolution ADC (>8 bit) and a larger photodiode array (e.g. 2048 channels).

### c Calibration

The accuracy of the wavemeter depends crucially on the precision of its calibration. The calibration procedure, especially a method for calculating the Fizeau wedge spacing, was described by Lu and Wu (1984). For a preliminary calibration we used an argon ion laser and a ring dye laser. The calculation of the wavelength included a correction for dispersion by the quartz plates (Morris et al. 1984). A modified version of this calibration procedure was used, which employed a scanning ring laser with its own

built-in wavemeter. The calibration of this device was checked against several accurately known absorption lines of iodine and was found to be in excellent agreement.

The wedge angle  $\alpha$  was first accurately determined with a He-Ne laser, using the fringe spacing  $P$  calculated from the interference pattern. It was found that the minima yielded a more consistent fringe spacing as they are less affected by the input power and the 'noise' present on the interference spectrum. Assigned to each fringe is the total phase difference due to the path difference between the two beams, given by

$$\phi_0 = \frac{2\pi}{\lambda_0} \Delta d(x) \quad (3.6.4)$$

The relative phase within an interference minimum of order  $N$  is given by

$$\phi = \frac{2\pi}{\lambda_0} \Delta d(x) - (2\pi N + \pi) \quad (3.6.5)$$

where the factor of  $\pi$  is due to the phase shift of the beam on reflection. Solving this expression for  $N$  yields:

$$N(\lambda_1) = \frac{\Delta d(x)}{\lambda_1} - \frac{\phi}{\pi} - \frac{1}{2} \quad (3.6.6)$$

When two wavelengths can be found whose relative phase is equal and which are separated in frequency within one interference order, (3.6.6) yields the following expression from which the opd may be determined.

$$1 = N(\lambda_1) - N(\lambda_2) = (\lambda_1^{-1} - \lambda_2^{-1}) \Delta d(x) \quad (3.6.7)$$

Knowing the opd allows the wavelength to then be calculated from (3.6.3).

While the above method is quite similar to the actual computer routine used in our system, certain modifications were made to improve the stability of the calculation. In our calculation, the reference fringe was specified to be the minimum which is closest to the first photodiode in the photodiode array. The position of this fringe is calculated from the intercept of a least squares fit of the position of all the interference fringe minima against the relative fringe order on the array. The first photodiode was also chosen to be the relative origin of the interference pattern and the opd  $\Delta D$  (now a constant since the position  $x$  has been fixed) was calculated for this diode.

The accurate determination of the opd  $\Delta D$  for this was accomplished by using the 'Autoscan' Coherent ring laser to determine three wavelengths for which the phase in eq. (3.6.6) was zero. A particular wavelength was chosen for which the phase was nearly zero and a scan about this wavelength, while determining the fringe spacing using our wavemeter, gave sufficient information that a least-squares fit of this data yielded an accurate wavelength value at which the phase was zero. A second wavelength was similarly determined, differing by one free spectral range of the wedge. Subtracting these two wavelengths as shown in eq. (3.6.7) yields the opd  $\Delta D$ . Once a first estimate of the opd was calculated from this expression, a third wavelength 100 free spectral ranges away was located at the farthest working range of the ring laser allowing a more accurate calculation of the opd.

The determination of an unknown wavelength follows from the solution of a modified form of eq. (3.6.6).

$$\lambda = \frac{\Delta D}{N(\lambda) + \frac{1}{2}} \quad (3.6.8)$$

where  $N$  is the interference order found with eq. (3.6.2) and the phase  $\phi'$  is the relative phase shift of the reference fringe (within one interference order) from the origin where the opd is known. This phase shift  $\phi' = \text{Intercept}/P$ , determined from the intercept of the least-squares fit of the interference minimum, has been normalized to the fringe spacing  $P$  such that it has a maximal value of  $\pm 1$  which corresponds to a wavelength shift equal to one free spectral range of the wedge as a function of the wavelength of the input light.

The final wavelength was determined from an expansion of eq. (3.6.8) neglecting higher order terms; this is essentially just a modified version of eq. (3.6.3):

$$\lambda = \frac{\Delta D}{N} + \frac{\Delta D \phi'}{N^2 \pi} \quad (3.6.9)$$

#### d Realignment of the Optical Components

Realignment of the wavemeter should not be required unless the optical fibre has to be replaced. Whenever this becomes necessary the following procedure is followed.

A new length of fibre is prepared and coupled to a He-Ne laser input beam. This coupling should be very good and should result in a power transmission of 50% or better of the input laser power through the fibre (and should be verified with a power meter). After removal of the top plate and loosening the fibre input sealing flange, the fibre chuck screw should be carefully loosened while noting the amount of fibre protruding from the end of the chuck. The old fibre should be replaced with the new section without tightening the chuck. This end of the fibre should produce a perfectly symmetric gaussian beam pattern if it is

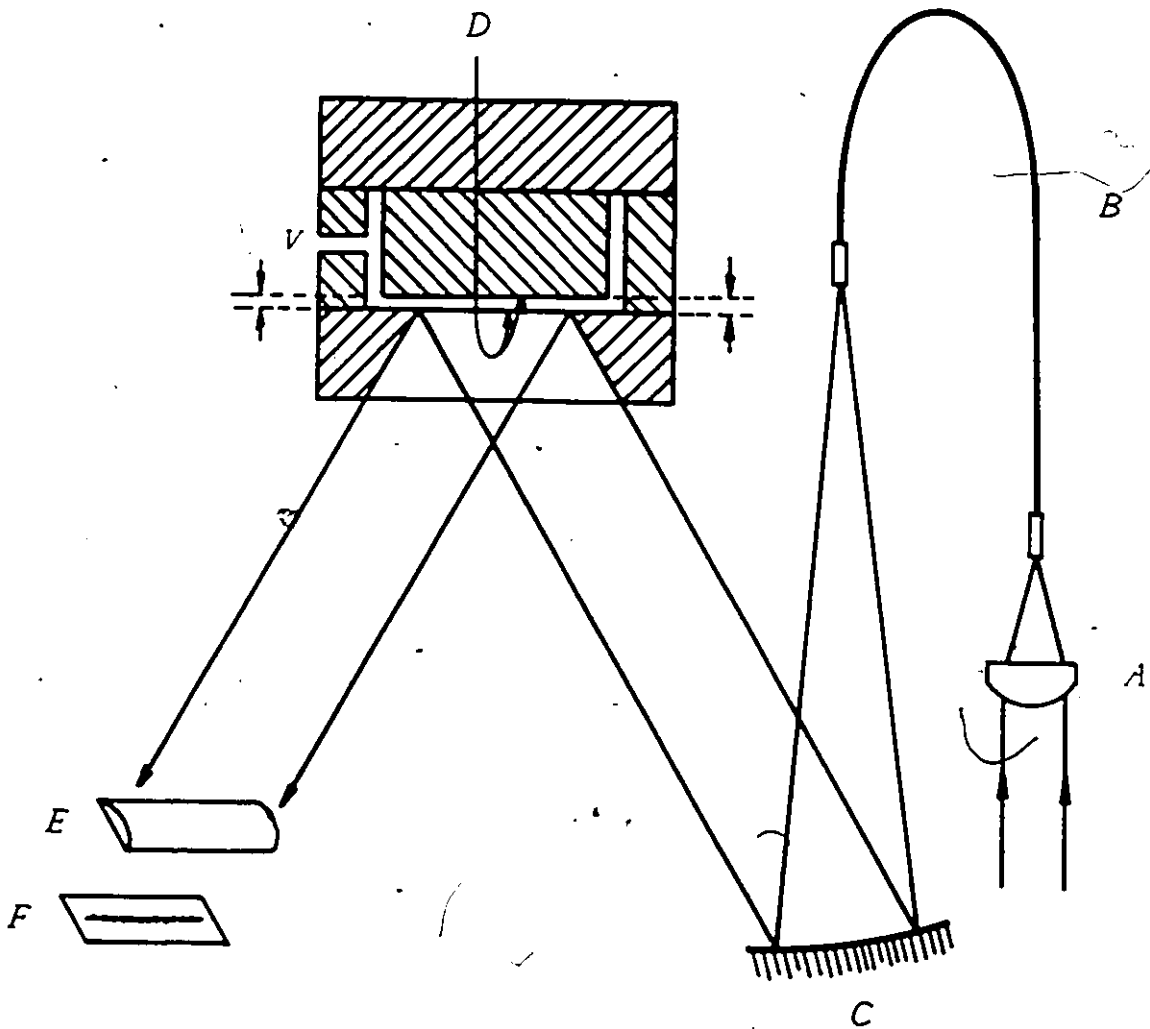
correctly cut.

The new fibre end must be placed at the focus of the parabolic mirror. To this end the bottom plate may be removed from the vacuum chamber after disconnecting the electrical contacts from the various components and removal of the plate hold down springs, though this is not recommended because critical alignments such as the zero-shear position may be disturbed and this operation may not be necessary if the alignment can be carried out in situ. The fibre position may be checked by using an interferometer to test the wavefront flatness on reflection from the mirror while adjusting the fibre end location, though this is rather difficult. The simplest way to ensure that the fibre is correctly positioned is to measure the size of the reflected pattern and adjust the position of the fibre-end until it appears that the pattern is non-divergent, even at considerable distances away from the wavemeter (this pattern may be observed through the window located behind the wedge). If the pattern remains non-diverging along one axis but diverges along another axis, the tilt of the fibre end has to be adjusted. The location and orientation of the wedge, cylindrical lens and the Reticon array (which have all been mounted with their faces parallel to one another) does not require adjustment. The final test for the adjustment of the fibre is that the interference pattern height is properly aligned with the center of the photodiode array (this may be checked by maximizing the amplitude of the video output signal from the photodiode controller). If it is not, the fibre end position has to be changed and the above procedure repeated.

### e Performance Specifications

The accuracy of the wavemeter depends strongly on the precision of its calibration. For preliminary calibration we used several  $\text{Ar}^+$  lines and the 632.8 nm He-Ne laser line. In addition we used approximately 50 wavelengths in the range 575-620 nm from a Coherent Auto-scan ring laser equipped with its own internal wavemeter. The Auto-scan wavemeter, which was dedicated to the ring laser and restricted to cw operation, was checked against two calibration lines of the  $\text{I}_2$  absorption spectrum. Its accuracy was better by a factor of 5 than that of ours which we found capable of wavelength measurement with an absolute accuracy of one part in  $10^6$  for cw input and, for pulsed input, better than two parts in  $10^6$ ; the short term precision was better than two parts in  $10^7$ . The accuracy of this instrument is limited mainly by systematic offsets due to the limited resolution of the ADC and, to a lesser extent, by statistical scatter.

Fig. (3.2) Optical layout of the Fizeau wavemeter. A, microscope objective; B, optical fibre; C, off-axis paraboloid; D, Fizeau interferometer; E, cylindrical lens; F, photodiode array. The arrows indicate the uncoated interferometer surfaces, v = vent. The air-gap spacing was  $10^{-3}$  m, the wedge angle was  $5.5364 \times 10^{-4}$  rad.





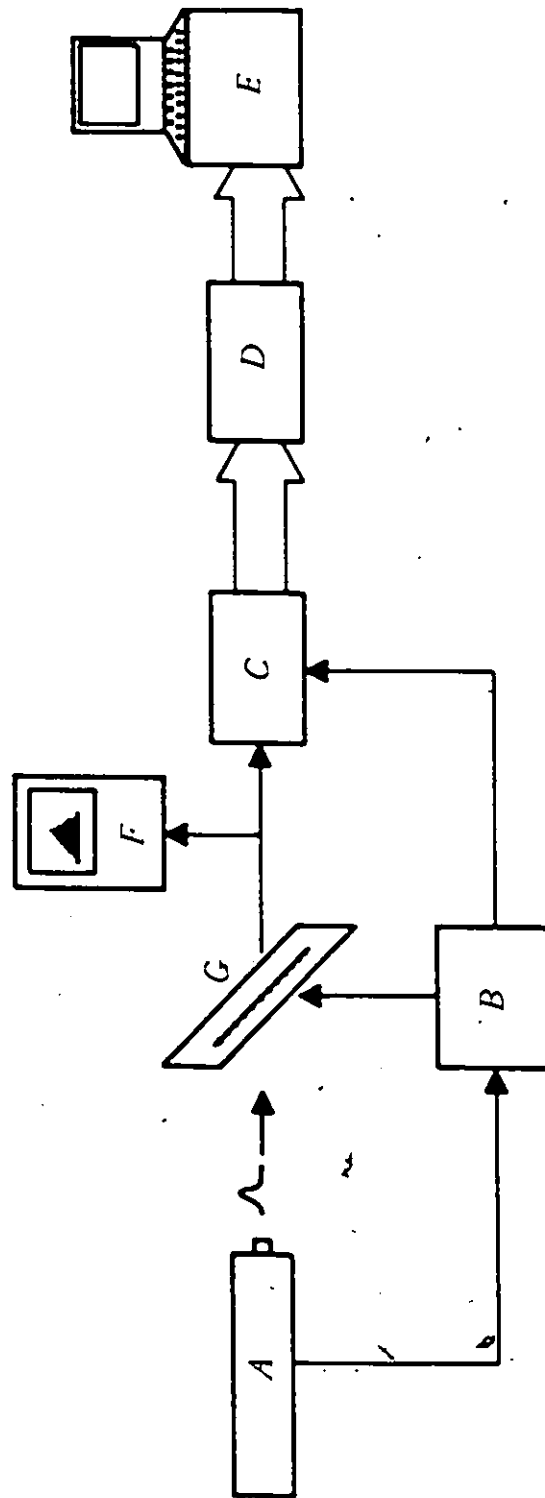


Fig. (3.3) Schematic diagram of the electronic data acquisition system of the wavemeter. A, laser; B, electronics for synchronization and timing; C, 8-bit ADC; D, memory buffer; E, microcomputer; F, oscilloscope; G, photodiode array.

### 3.2 Description of the Apparatus for the Measurements of Atomic Lifetimes

The arrangement of the apparatus is shown in figure (3.4) and is similar to that described by Hart and Atkinson (1986). The output of a N<sub>2</sub> laser pumped dye laser, directed into a pyrex cell containing potassium vapour, was used to selectively excite the 5P, 6P or 7P fs states. The fluorescence, resulting from the decay of the excited state to the 4S ground state, was monitored at right-angles to the direction of excitation, resolved by a monochromator and detected with a photomultiplier. The amplified PM signal was analyzed by a transient digitizer interfaced to a computer, yielding a time-evolution spectrum of the fluorescence.

The N<sub>2</sub> laser and dye laser were both manufactured in house. The N<sub>2</sub> laser produced an output energy of 2mJ per pulse and was operated at 12 Hz. The dye laser consisted of an oscillator and an amplifier. The oscillator incorporated two holographic 1800 l/mm gratings, one held at near grazing incidence and the other mounted on the tuning arm in a Littrow configuration. The tuning arm was coarsely adjusted by means of a micrometer screw and fine-tuned by means of a piezoelectric transducer which acted as the stop for the micrometer screw and allowed a  $\pm 20 \mu\text{m}$  movement for a  $\pm 1000 \text{ V}$  bias. The dye laser output spanned 3-4 modes and had an effective bandwidth of 4 GHz. A saturated solution of DPS in a solution of p-dioxane was used for the excitation of the 5P state,  $10^{-3} \text{ M}$  Nile blue in ethanol was used for the 6P state (the 689 nm output was frequency doubled), and the 7P state was excited using the frequency doubled 643 nm output produced by  $2 \times 10^{-2} \text{ M}$  solution of R640 in ethanol.

The dye laser output, after frequency doubling (if required), was made incident on a Pellin-Broca prism where the uv and visible components were separated. The visible component was used to trigger a fast photodiode and the uv component was directed into the fluorescence cell. The diameter of the laser beam was sufficiently small that tight focussing into the cell was not necessary; this reduced the occurrence of photoionization which has a higher probability at higher laser power densities.

The cylindrical fluorescence cell was 10 cm long and 5 cm in diameter, with plane end-windows perpendicular to the cell axis. It was fitted with a 7-cm long sidearm, 1 cm in diameter, which contained a few grams of potassium and protruded in a horizontal direction. The cell was connected by a narrow-bore tube 2mm in diameter through a magnetically operated greaseless stopcock to the vacuum system, composed primarily of an Edwards 2 inch diffusion pump backed by an ES30 forepump which produced a nominal vacuum of  $5 \times 10^{-7}$  torr. During the experimental runs the cell was continuously pumped through the capillary and the closed greaseless stopcock (as this leaked slightly) to remove any gaseous impurities desorbed from the glass surfaces, however no noticeable trace of K metal diffused from the cell. The cell and sidearm were mounted in a two compartment electrically heated oven and were separated from the heaters by a stainless steel enclosure. The sidearm was heated separately and was insulated from the main oven heaters. The temperature was measured with 4 copper-constantan thermocouples attached at various points on the cell and sidearm which was kept at a temperature 15 K below that of the cell to avoid condensation of metal on the windows. The

whole oven assembly was located at the centre of Helmholtz coils whose purpose was to counteract the effects of the earth's magnetic field on the measurement of the lifetimes.

The fluorescence emitted by the vapour was focused on the entrance slit of an ISA Mod. HR-320 grating monochromator fitted with an 1800 l/mm holographic grating and a stepper motor drive for wavelength scanning. The entrance and exit slits were set to produce an 80 Å band pass. The radiation passing through the exit slit was focused onto the photocathode of a refrigerated RCA 31034 photomultiplier tube operated at 2070 volt, whose signal was amplified and sent to the Biomation 6500 transient digitizer interfaced to a Commodore Pet 2001 computer.

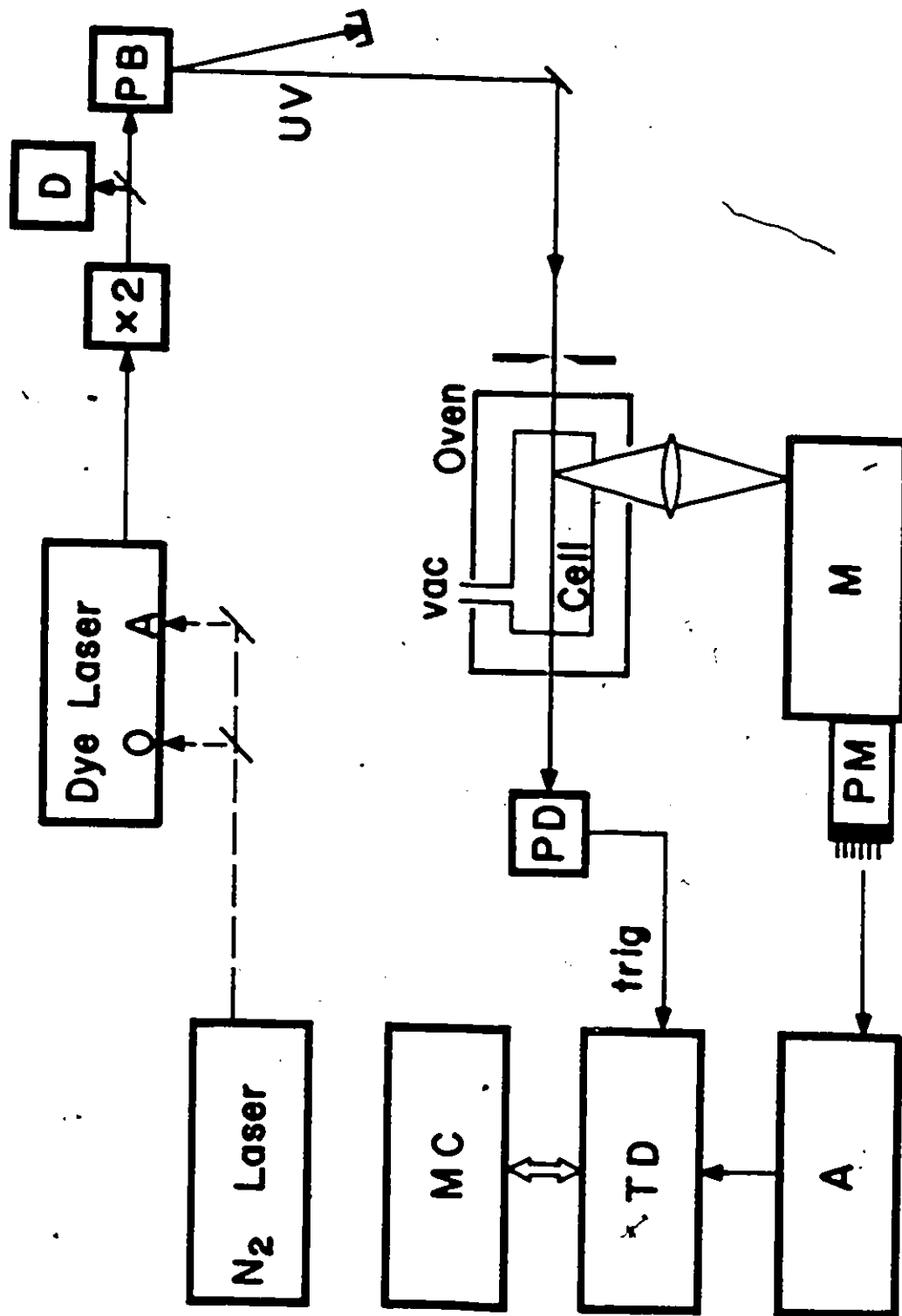
The signal was amplified with a fast Ortec 9301 10X preamplifier whose 50  $\Omega$  terminated output was further amplified (20X) by a slower Ortec 9302 amplifier. This configuration was the final result of numerous trials with other amplifiers and various terminations to minimize the after-pulse ringing and noise pickup. The Ortec 9302, when used at a gain of 200X, produces considerable after-ringing which results in false signal modulation. The final combination of the two amplifiers still produces some pulse ringing which was observed on a 1 Gigasample/sec transient analyzer; however, the amplitude was small and of such high frequency that the 100 MHz input bandwidth limit of the Biomation waveform analyzer did not easily detect it.

The Biomation Mod. 6500 waveform analyzer is a 1024 channel TD capable of a time resolution of 2 ns per channel. The time resolution was set at 2 ns for the 5P and 6P states, and 5 ns for the 7P state. The TD was gated-on after a short time delay from the start of the laser pulse to avoid the detection of scattered laser light. After each pulse was analyzed, the digitized signal was sent to the

computer where the data were summed until the first channel had accumulated more than 65000 counts. The data were then stored on disk along with the temperature profile and further analyzed to determine the lifetime of the excited state.

Figure (3.4).

Schematic diagram of the apparatus for lifetime measurements. D, thermionic diode; PB, Pellin-Broca prism; PD, photodiode; A, amplifiers; TD, transient digitizer; MC, computer.



### 3.2.1 Experimental Procedure

Before starting the experiment, the fluorescence cell and sidearm were baked under vacuum for 2 days and then potassium was vacuum distilled into the sidearm. The main oven was kept at operating temperature throughout the experiment while the sidearm was allowed to cool between runs. Before each run the sidearm oven was turned on and allowed to stabilize over a 2 hour period. During this time the lasers were stabilized, the dye laser was tuned to the selected wavelength with the aid of the thermionic diode or the Fizeau wavemeter, and the Pellin-Broca prism, frequency doubling crystal, monochromator and lenses adjusted for the proper wavelength and alignment. The oven and sidearm temperatures were periodically checked during each run and were found to be stable within  $\pm 0.5$  K over the average run of 4 hours.

The initially recorded spectra exhibited modulation components, even though the earth's magnetic field had been cancelled to within  $\pm 2 \times 10^{-3}$  G with the aid of the Helmholtz coils. To suppress the quantum (hfs) beats, a linear polarizer was first inserted between the cell and the monochromator at the 'magic angle' of  $54.7^\circ$ , which is the first zero of the quantum beat polarization characteristics (Dodd and Series 1978, van Wijngaarden et al. 1986). The modulation was then suppressed to barely noticeable levels, but the low transmission of the linear polarizers for this wavelength region ( $< 20\%$ ) resulted in a noticeable reduction of the signal-to-noise ratio. An alternative and more successful device for suppression of the quantum beats was then applied, by setting the Helmholtz coils to produce a field of 25 gauss at the cell, thus shifting the frequency of the modulation to a range which was not detectable or was



time-averaged to zero by the TD. At this field, the Zeeman splitting of the fs P states was still only 10% of the pump laser bandwidth, ensuring uniform excitation of the broadened fs state. The main advantage of this method was found to be the good reproducibility of the data and the high signal-to-noise ratio.

## 4 RESULTS AND DISCUSSION

### 4.1 Fine-structure Excitation Transfer

Figure 4.1.1 shows typical interferograms of the fluorescence Zeeman spectrum consisting of two components, one due to direct fluorescence and the other due to sensitized fluorescence resulting from collisions with noble gas atoms. A large number of such spectra was recorded over a range of buffer gas pressures. The integrated intensity ratios  $r$  of sensitized-to-direct fluorescence are plotted in figures (4.1.2) and (4.1.3) in relation to the buffer gas pressure and the collision numbers  $Z_{ab}$ , corresponding to these ratios, are plotted in figures (4.1.4) and (4.1.5). The plots exhibit a moderate curvature which indicates the presence of multiple collisions at higher gas pressures. As expected, the plots of the  $Z$  numbers are linear. The cross sections  $Q$ , which are proportional to the slopes of the plots of the collision numbers, were calculated with eqs. (2.1.11-12) from all the data points and averaged. They are presented in Table (4.1.1) and are compared with the theoretical values of Spielfiedel et al. (1979). Our values are considered to be accurate within  $\pm 15-20\%$ , the main source of experimental error arising from the uncertainty of the gas pressure measurements and from the counting statistics, since the count rate was kept low to avoid pileup corrections.

The ratio  $Q_{12}/Q_{21}$  of the independently measured cross sections is in better agreement with the value of 1.9 predicted from detailed balancing than might be expected from the stated limits of error. While no estimate is available for the accuracy of the theoretical values,

3

Spielfiedel et al. (1979) quote a range of values obtained by their various calculations, which differ among each other by a few percent. It is apparent from Table (4.1.1) that, although there is agreement as to order of magnitude between the experimental and calculated values, the experimental results are larger except for the Xe cross section.

Nevertheless, the two sets of cross sections exhibit a similar overall trend, showing minima for Neon bracketed by relatively larger He and Ar values. No fully satisfactory explanation can be offered for the decrease of the measured cross sections from Ar to Xe, since the opposite trend should be expected on the basis of the polarizabilities of these atoms, though previous experiments with the second and third P-doublets in Rb (Siara et al., 1972) and Cs (Siara et al., 1974; Pimbert et al., 1970) also produced cross sections which were not fully correlated with the polarizabilities of the noble gases. The fact that the mixing cross sections do not increase monotonically with the polarizabilities, might be due to the effect of the different relative velocity of the colliding pairs from K-He to K-Xe. These results are compared to those measured at 70 kG and with the most recent theoretical calculations in Table (4.2.2).

Figure (4.1.1)

Interferogram of the 4044 Å/4047 Å fluorescence doublet in K with 200 mtorr Kr, arising from the  $5^2P \rightarrow 4^2S$  transitions (2 orders), showing direct and sensitized components; (a) with laser excitation of the  $5^2P_{3/2}$  state; (b) with laser excitation of the  $5^2P_{1/2}$  state.

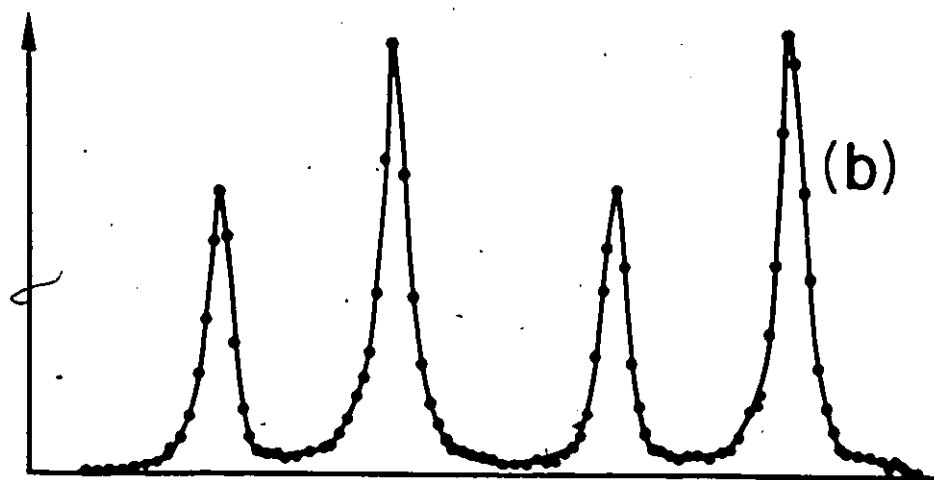
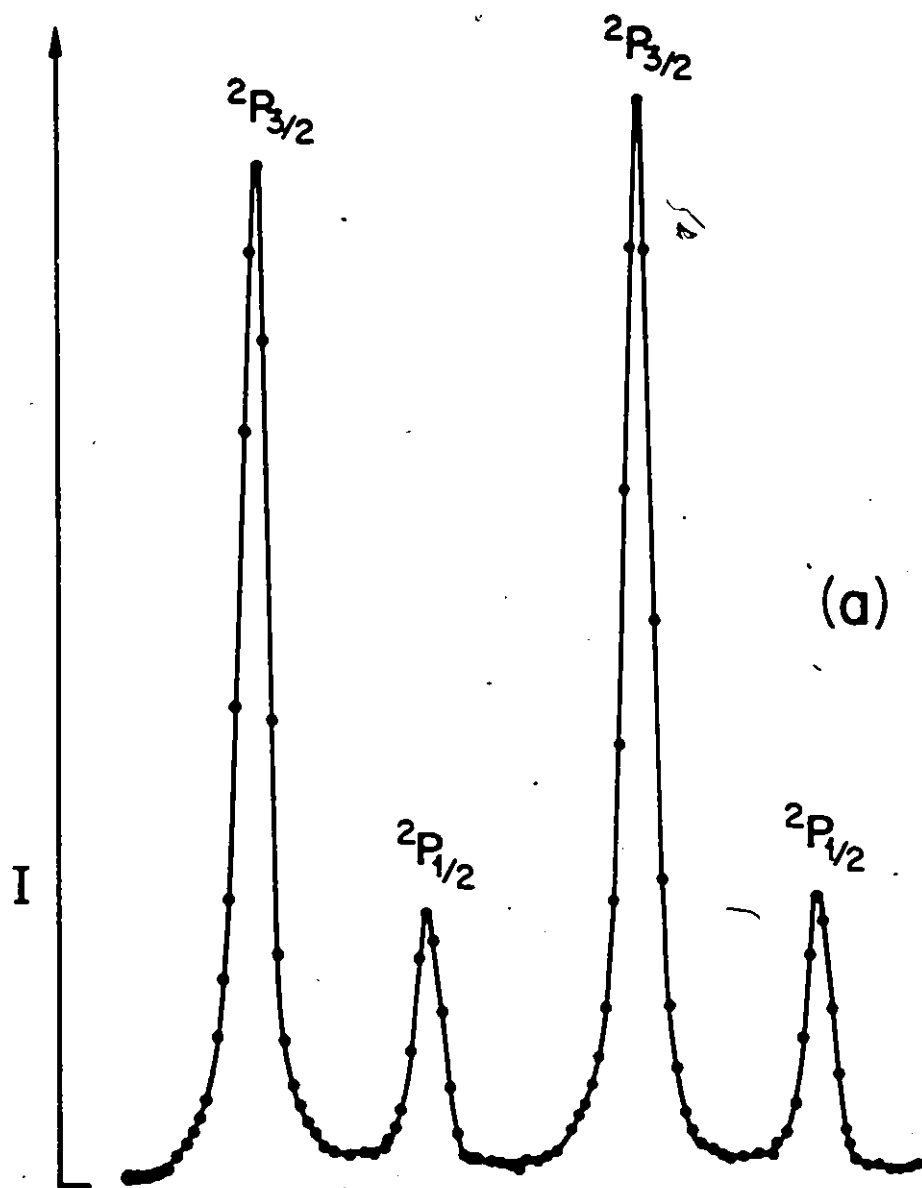


Figure (4.1.2)

Plots of fluorescent intensity ratios  $\eta_1$  and  $\eta_2$  against He and Ar pressure.

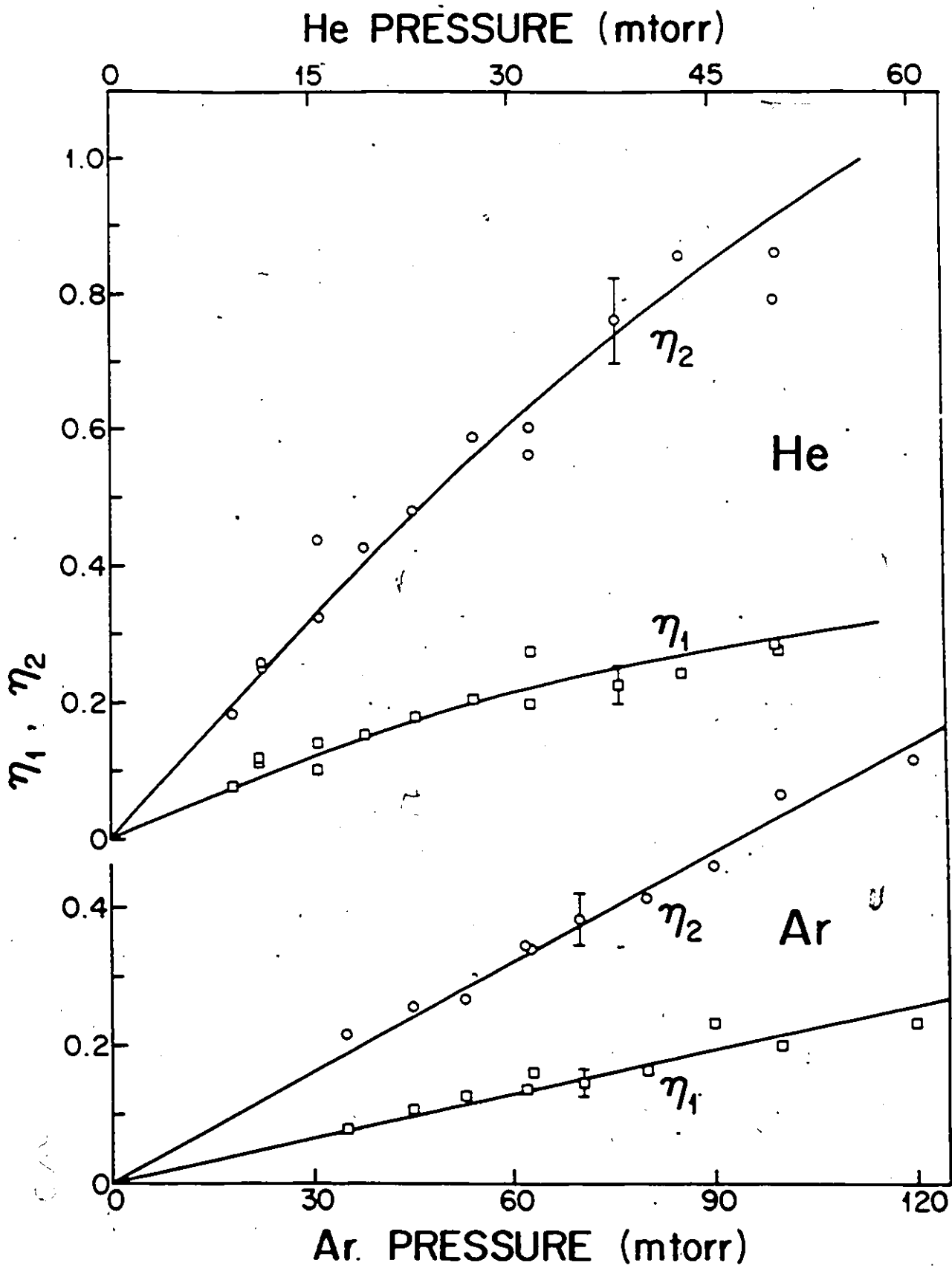


Figure (4.1.3)

Plots of fluorescent intensity ratios  $\eta_1$  and  $\eta_2$  against Ne, Kr and Xe pressure.



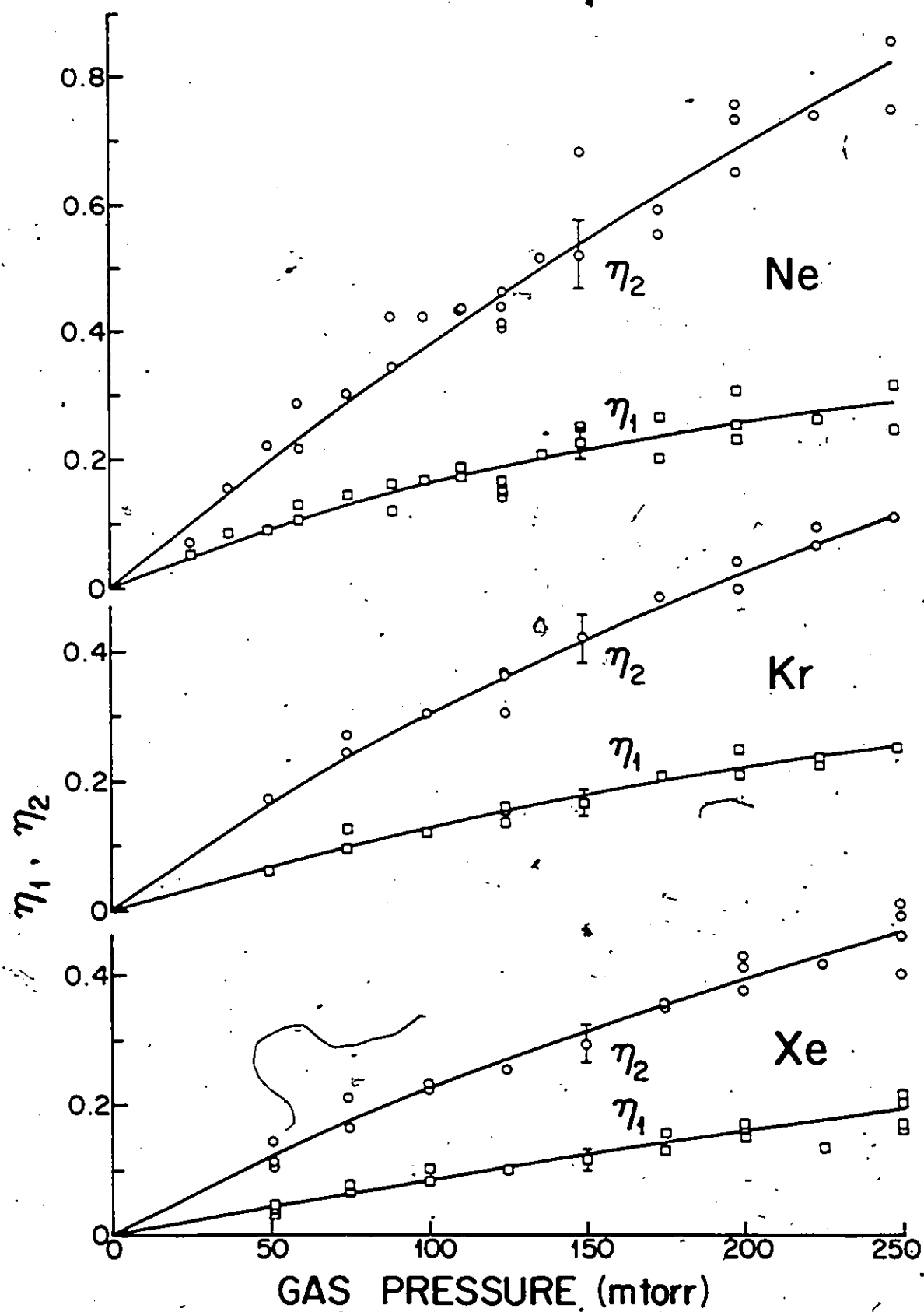


Figure (4.1.4)

Plots of collision numbers  $Z_{12}$  and  $Z_{21}$  against Ar and He pressure.

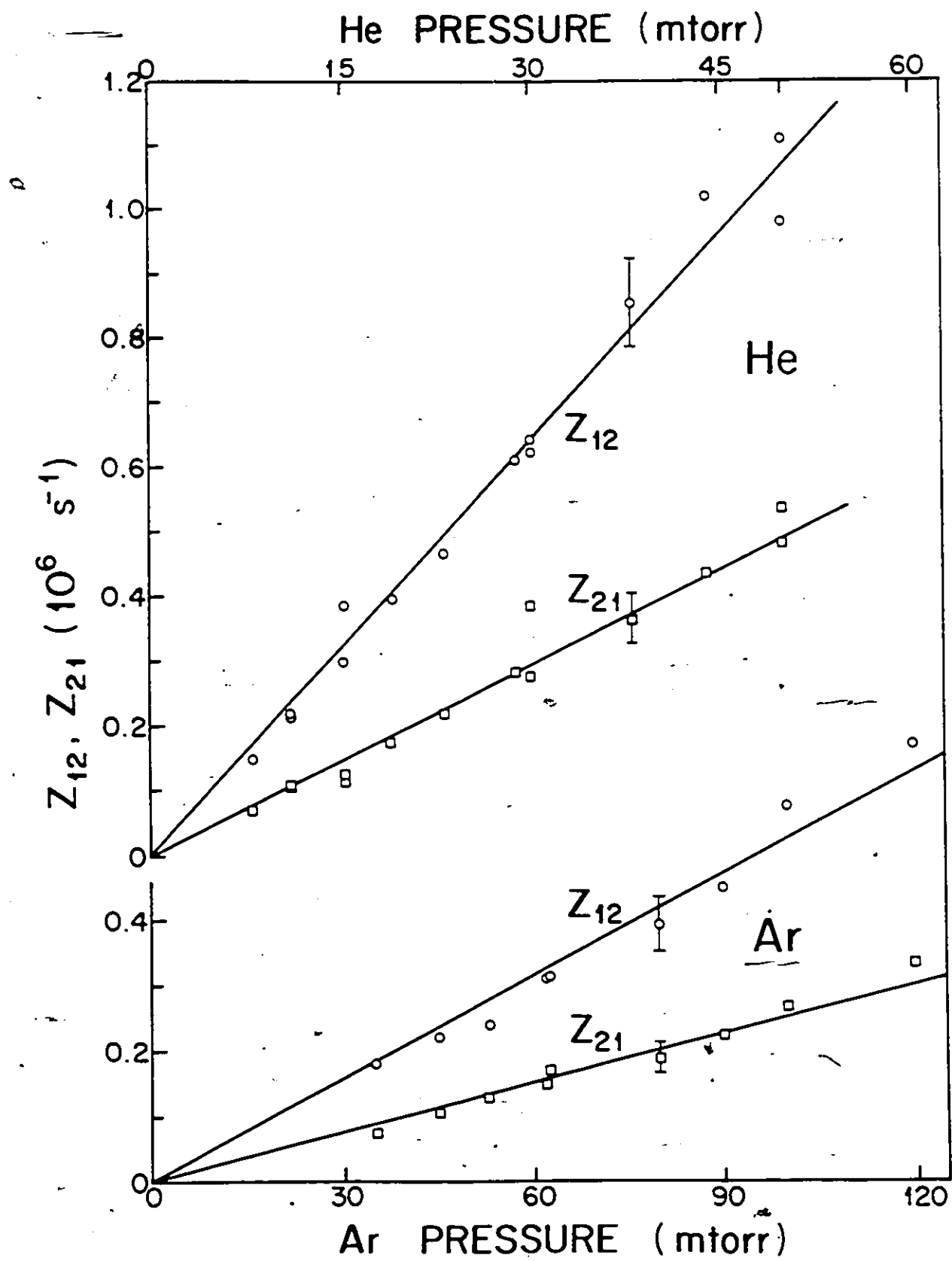


Figure (4.1.5)

Plots of collision numbers  $Z_{12}$  and  $Z_{21}$  against Ne, Kr and Xe pressure.

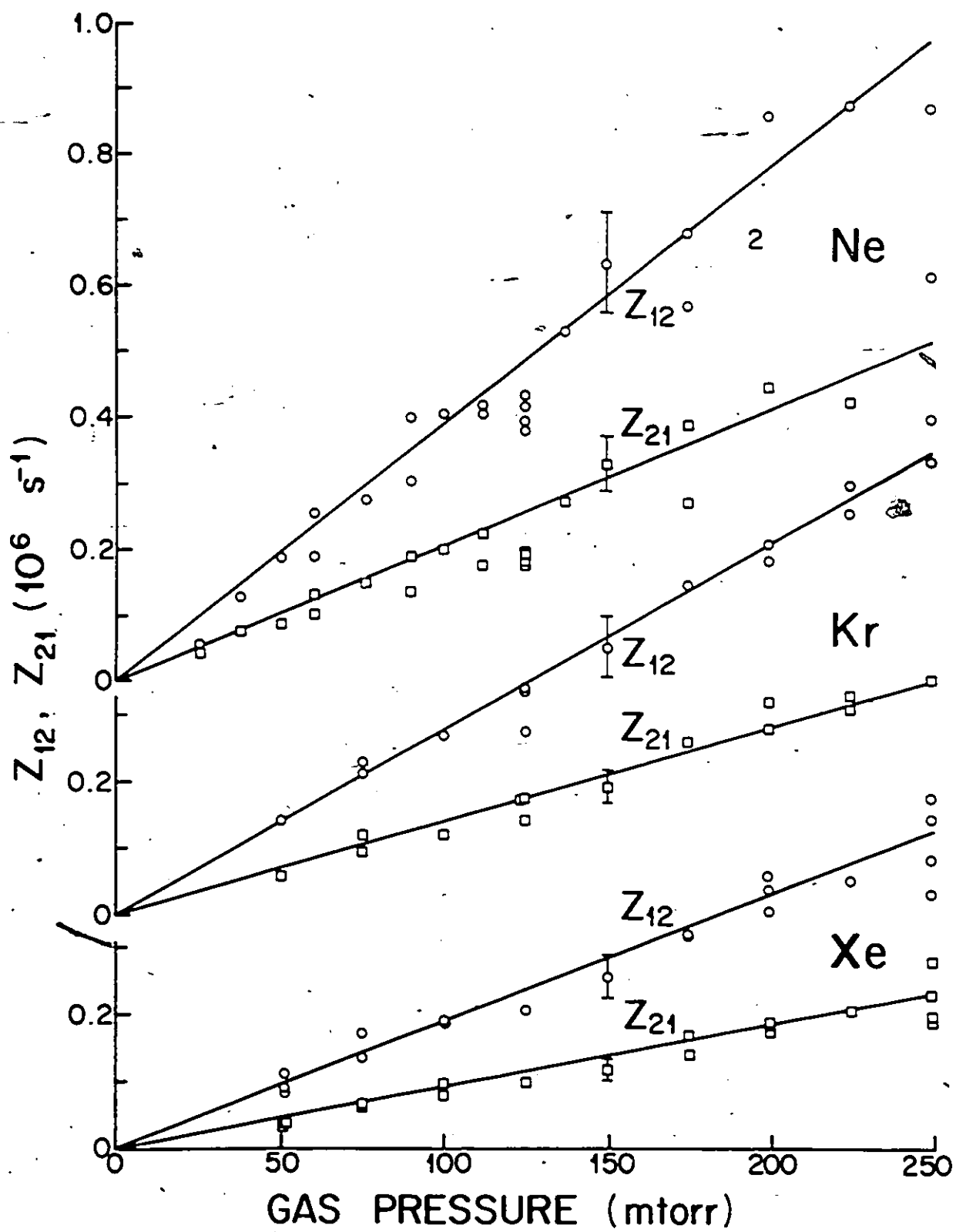


Table (4.1.1): 5P Fine-structure Mixing Cross Sections for He-Xe ( $10^{-16} \text{ cm}^2$ )				
Collision Partner	$Q_{12}$ ( $5^2P_{1/2} \rightarrow 5^2P_{3/2}$ )	$Q_{21}$ ( $5^2P_{1/2} \leftarrow 5^2P_{3/2}$ )	$\frac{Q_{12}}{Q_{21}}$	Ref.
K-He	561 $\pm$ 84 156	260 $\pm$ 39	2.2	a b
K-Ne	196 $\pm$ 29 75	98 $\pm$ 18	2.0	a b
K-Ar	317 $\pm$ 45 139	153 $\pm$ 22	2.1	a b
K-Kr	195 $\pm$ 29	99 $\pm$ 18	2.0	a
K-Xe	146 $\pm$ 21 166	67 $\pm$ 11	2.1	a b
a, This work: b, Spielfiedel et al. (1979)				

#### 4.2 Relaxation Of The 5P Multipole Moments

The energy levels of the 5P Zeeman substates and the transitions between them are shown in Fig.(4.2.1). The fluorescence spectrum obtained with  $5^3P_{1/2-1/2}$  excitation in the presence of 50 mtorr Ar is shown in Fig. (4.2.2). The peaks are identified as arising from the transitions labelled A-F in Fig. (4.2.1). The spectrum consists of two traces, one above the other, which represent the two polarization components  $\sigma^+$  and  $\sigma^-$  of the fluorescence; the two components were detected and registered separately in alternate sweeps of the interferometer. The traces include two interference orders in which the six separate Zeeman components are clearly resolved (the experimental data usually included 3 orders). The asterisks in the figure indicate contributions of the opposite polarization due to leakage through the linear polarizers. The polarizer leakage was less than 5% and introduced little error in the measured cross sections as it could be identified and compensated for. The trace represents typical data accumulated during an 8-h run and consisted of over 30,000 counts. A similar trace of the fluorescence spectrum recorded for  $5^3P_{3/2-3/2}$  excitation with a Ne pressure of 150 mtorr is shown in Fig. (4.2.3). As the buffer gas pressure is considerably higher here than in Fig. (4.2.2), the sensitized fluorescence peaks have a correspondingly higher intensity relative to the direct fluorescence peak. The resolution of the Zeeman components is considerably better than might be apparent from the figures in which the horizontal scale has been compressed. The area under each peak in these fluorescent spectra was calculated by hand from a plot of the data listing the number of counts accumulated in each channel. The ratio of

the sensitized-to-direct fluorescence peak areas was then found and corrected for the time delay between excitation and detection as discussed in section (3.1.4).

The ratios of sensitized to direct fluorescence intensities, multiplied by the appropriate A coefficients, are plotted in relation to the buffer gas pressures in Figs. (4.2.4-5) for He, Figs. (4.2.6-7) for Ne, and Figs. (4.2.8-9) for Ar. The plots represent the population ratios of the collisionally-to-radiatively populated Zeeman sublevels in the 5P Zeeman manifold as a function of pressure of the buffer gas; the plots are reasonably linear over a range of buffer gas pressures which extend from 20 mtorr (He) to 160 mtorr (Ar). The linearity of the data suggests the absence of multiple-collisional excitation transfers, including back transfer. The individual Zeeman mixing cross sections  $Q(J,m \rightarrow J',m')$ , determined from the slopes of the plots of the experimental data presented in Figs. (4.2.4-9) against  $Nv,\tau$ , were calculated from weighted least-squares fits of the data and are listed in Table (4.2.1). In order to verify the observed linearity of the population ratios with pressure, the evolution of the population density of the Zeeman substates with pressure was computer-simulated (see section 3.1.4), using the experimental Zeeman mixing cross sections. The result of the simulation for He is shown in Fig. (4.2.10). It predicts a roughly linear dependence of the ratios with pressure, with a slight downward curvature at increased pressures. This curvature is within the experimental error indicated in the plots of the experimental ratios shown in Figs. (4.2.4-5). The simulation agrees (within error) with the observed experimental trends, indicating that the slopes of plots of population ratios against  $Nv,\tau$  are representative of the Zeeman mixing cross sections.



The results presented in Table (4.2.1) show a trend which has been noted in some previous experiments, namely, that the Ne cross sections are relatively smaller when compared with the He and Ar values (Gay and Schneider 1976, Berdowski and Krause 1968). The last entry in Table (4.2.1) is the cross section  $Q(3/2, -1/2 \rightarrow 3/2, 1/2)$  which was not determined experimentally but may be calculated from the other cross sections using eq. (2.2.93). The uncertainties listed with the cross sections represent one standard deviation of the average value of the cross section determined from the raw data points. These statistical uncertainties are of the order of 10% for most of the cross sections with the exception of  $Q(3/2, -3/2 \rightarrow 3/2, -1/2)$  and  $Q(3/2, -3/2 \rightarrow 1/2, -1/2)$ , which were more difficult to determine because of a slight overlap of the fluorescence peaks and the small 'leakage' through the polaroid analyzers.

Table (4.2.1) also includes theoretical values of the cross sections calculated for He by Pascale (1987) and for Ne by Spielfiedel and Feautrier (1988). The experimental and theoretical cross sections for He agree on the whole within the stated error limits, with the notable exception of the cross sections  $Q(1/2, -1/2 \rightarrow 3/2, -3/2)$  and  $Q(1/2, -1/2 \rightarrow 3/2, -1/2)$ . The latter were derived from clearly resolved fluorescence components and were consistent from one run to another as indicated by the standard deviations as well as by the linearity of the data points shown in Fig. (4.2.4). This difference between the experimental and theoretical values cannot be readily explained in terms of only experimental error. The experimental and theoretical cross sections for Ne agree well for transfers between Zeeman substates within the directly excited fs state, but not nearly as well for the transfers between the fs states.

The fs and orientation transfer cross sections,  $\sigma^{(0)}$  and  $\sigma^{(1)}$ , respectively, were derived from the Zeeman mixing cross sections using eqs. (2.2.79) and (2.2.80) and are listed in Table (4.2.2) for He, Ne and Ar along with the theoretical values calculated by Spielfiedel et al. (1979), Pascale (1987) and Spielfiedel and Feautrier (1988). The error limits accompanying the experimental cross sections in Table (4.2.2) were derived from the sums of the standard deviations of the individual Zeeman mixing cross sections from which the transfer and relaxation cross sections were calculated. The fs transfer cross sections provided a useful check against the values of these cross sections determined in zero field, which are also listed in the table. It may be seen that there is agreement (within error) between the experimental cross sections obtained at 70 kG and those determined in zero field for Ne and Ar, though the agreement for He is not as good. The He values determined in both the zero and high field experiments are consistently larger than the theoretical values. The difference between the calculated cross sections and experimental high-field data, particularly for the case of Pascale's calculation, arises from a disagreement between the cross sections  $Q(1/2-1/2 \rightarrow 3/2-1/2)$  and  $Q(1/2-1/2 \rightarrow 3/2-3/2)$ . The agreement between the experimental and calculated fs mixing cross sections for Ne is not very good. The theoretical calculations of Spielfiedel and Feautrier (1988) are a factor of four smaller than the corresponding cross section for He and are a factor of two smaller than the previous calculations of Spielfiedel et al. (1979); they are also much smaller than the experimental values determined in zero field and at 70 kG. The orientation transfer cross sections  $\sigma^{(1)}$  are derived from the sums and differences of considerably larger cross sections which renders them subject to considerable error. It should be noted that the

practice of presenting the negative of the orientation transfer cross sections (Berends et al. 1988 eq.(11)) has not been adopted here. The large variety of conventions for normalization and for the sign indicating the direction of transfer (Elbel 1979, Wilson and Shimoni 1975) leads to confusion in the comparison of theoretical and experimental values; the convention used here is stated by eq. (2.2.79). The comparison of the orientation transfer cross sections with the calculated values of Spielfiedel (1979) and Pascale (1987) is interesting in that, though the magnitudes of the cross sections are similar, the transfer direction for  $\sigma'(1/2 \rightarrow 3/2)$  is different. This difference in sign is consistent for all the buffer gases as indicated in Table (4.2.2). It may be seen in Table (4.2.1) that, in each case, the cross sections  $Q(1/2-1/2 \rightarrow 3/2-3/2)$  and  $Q(1/2-1/2 \rightarrow 3/2-1/2)$  are larger than  $Q(1/2-1/2 \rightarrow 3/2+3/2)$  and  $Q(1/2-1/2 \rightarrow 3/2+1/2)$ , respectively, indicating the preferred excitation transfer to the negative  $m_j$  components of the collisionally populated fs Zeeman manifold, in contrast to the theoretical predictions. This is equivalent to the preservation of orientation during the collisional interaction, which was not observed with the Na(3P) atoms in collisions with noble gases (Gay and Schneider, 1976). It should be noted, however, that the orientation transfer cross section  $\sigma'(3/2 \rightarrow 1/2)$  for He agrees both in magnitude and direction with the predicted value. The disagreement in the sign of the orientation transfer direction for the transition  $S^2P_{1/2} \rightarrow S^2P_{3/2}$  states is most likely due to the large Zeeman splitting which is shown to scale in Fig. (6.1), Appendix A. The energy difference between the  $S^2P_{1/2-L_{2,3}}$  and the  $S^2P_{3/2-3/2}$  states is  $13.3 \text{ cm}^{-1}$  while the energy difference between the  $S^2P_{1/2-1/2}$  and the  $S^2P_{3/2-3/2}$  is  $26.4 \text{ cm}^{-1}$ . Although the Boltzmann factor is not appreciably different for these two cases at the experimental temperatures, nevertheless the

non-negligible difference in energy splitting would suggest a greater probability of excitation transfer between states with relatively smaller energy separation. This is verified by the Zeeman mixing cross sections shown in Table (4.2.1).

The multipole relaxation cross sections for collisions with He, Ne and Ar are presented in Table (4.2.3). They were calculated from the Zeeman mixing cross sections presented in Table (4.2.1) using eqs. (2.2.93-96).

The multipole relaxation cross sections may also be calculated from eqs. (2.2.81-82) which require the determination of all the population ratios in the directly excited fs state if the zero-field transfer cross sections are used, or by eqs. (2.2.98-101) which require the accurate determination of all the population ratios for the complete Zeeman 5P manifold at a particular pressure. The denominator of the coefficient  $K_{\mu}$  in eqs. (2.2.84-87) approaches zero when the individual population ratios approach unity; this should be expected at high buffer gas pressures, when the high collision rate would create a uniform population density distribution among the Zeeman substates. Because of the form of the denominators, the coefficient  $K$  and thus eqs. (2.2.81-82, 98-99) have a non-linear pressure dependence. The pressure variation of equation (2.2.98-99) has been plotted for He in Fig. (4.2.11) using the experimental cross sections to predict the population ratios, which were then substituted into the  $K$  coefficients, and in Fig. (4.2.12) for the theoretical cross sections (Pascale 1987). The plots in Fig. (4.2.11), the slopes of which are representative of the multipole 'relaxation cross sections' defined by eq. (2.2.98-99) for all the gases, are characterized by their curvature which, though small for the dipole components, increases for the quadrupole and octupole components. It thus seems clear

that the interpretation of the data by eqs. (2.2.98-99) and shown in Figures (4.2.11-12), is imprecise as the cross sections cannot be pressure dependent (as indicated by the curvature of the plots). We are also led to the conclusion that both eqs. (2.2.81-82) and (2.2.98-99) are only valid at low pressures. Equations (2.2.100-101), however, are of the form  $\chi = A + BX$ , where  $X$  is proportional to the pressure,  $A$ , the low-pressure intercept, is defined as the inverse of the relaxation cross section and  $B$  may be regarded as a coefficient describing the rate at which the multipole components equalize at increased collision rates and indicates the degree of curvature of the plots presented in Fig. (4.2.11-12). A simulation of eqs. (2.2.100-101) has been plotted for He in Figs. (4.2.13) and (4.2.14) using the experimental and theoretical Zeeman mixing cross sections (Pascale 1987), respectively, presented in table (4.2.1). The inverse of the low-pressure intercepts in both Fig. (4.2.13) and (4.2.14) accurately yields the multipole relaxation cross sections presented in Table (4.2.3) and the slopes of the plots should be positive and in the ratio  $\sigma^{(10)}/A_{H}^{(1)}$ . Figures (4.2.13-14) indicate that a correlation exists between all the Zeeman mixing cross sections and provide a sensitive test of the self-consistency of both the experimental and theoretical cross sections. The values of  $\sigma^{(10)}$  which may be obtained from the slope of these plots do not agree with the values presented in Table (4.2.2) in magnitude or, in some cases, in sign. This is not unexpected considering the experimental error stated with the experimental cross sections in table (4.2.1), and indicates that the error associated with the individual Zeeman mixing cross sections is compounded in the calculation of the multipole relaxation cross sections for both the experimental and theoretical values.

Table (4.2.3) also includes three sets of theoretical multipole relaxation cross sections. The calculations of Spielfiedel et al. (1979) were carried out for He, Ne and Ar; some of their values are in good agreement with the experimental data, and some clearly disagree. The more recent calculations of Spielfiedel and Feautrier (1988) for Ne are in agreement within the limits of error assigned to the experimental data, as are the calculations of Pascale (1987) for He. All the theoretical calculations indicate that, for  $P_{3/2}$  relaxation, the quadrupole relaxation component should be the largest. This trend, though noted for Na(3P) in collisions with noble gases by Gay and Schneider (1976) and for K(4P) by Skalinski and Krause (1982) and Boggy and Franz (1982), is not clearly borne out in the present experiment in which the octupole component is consistently the largest. The large uncertainty present in the octupole relaxation cross sections may mask the theoretically predicted trend, but it is also possible that the relatively large Zeeman splitting between the  $5^2P_{3/2,5/2}$  and the  $5^2P_{3/2,3/2}$  ( $13 \text{ cm}^{-1}$ ) states due to the strong magnetic field may have enhanced the measured octupole relaxation cross section. The determination of the population ratios from the measured intensity ratios depends on the Einstein A coefficients listed in eq. (2.2.70). The magnetic field-dependence of the relative intensities of the circularly polarized components was not determined experimentally and is a possible source of systematic error. The zero-field and high-field fs mixing cross sections are within the stated error for Ne and Ar indicating that the predicted field variation of the A coefficients is not inconsistent with the experimental results, but the reliability of the ratio of the A coefficients for the  $5P_{3/2}$  state could not be experimentally verified.

The calculations of Spielfiedel et al. (1979) were based on the interatomic model potentials of Pascale and Vandeplanque (1974) and were carried out semiclassically (using a straight-line trajectory approximation) and also fully quantum mechanically. The cross sections listed in Table (4.2.3) are the mixed results quoted by these authors, though the semiclassical and quantum mechanical methods did not yield significantly different values. The authors employed the impact approximation in all the calculations and neglected coupling to states other than the  $5^2P$ ; their principal aim was the treatment of the broadening and shift of the spectral lines emitted in the  $5^2P \rightarrow 4^2S$  transition. It is not surprising that the agreement of the 1979 calculations with our cross sections is not particularly good as the calculations are highly dependent on the model potentials which, as the authors themselves indicated, were of doubtful accuracy. The more recent calculations of Pascale (1987) are based on improved interatomic potentials as are those of Spielfiedel and Feautrier (1988) (Masnou-Seeuws 1982) and, as may be seen, they are in better agreement with the experimental measurements of transfers within each fs state, though there are some differences between the experimental and calculated fs and orientation transfer cross sections.

The multipole relaxation cross sections are larger by roughly a factor of two than those for collisions of K(4P) atoms with noble gases (Skalinski and Krause 1982; Boggy and Franz, 1982); this is due in part to the larger fs splitting of the 4P state ( $58 \text{ cm}^{-1}$ ). They are also somewhat larger than the corresponding values for the Na(3P) state (Gay and Schneider, 1976) which has a fs splitting ( $17 \text{ cm}^{-1}$ ) similar to the K 5P state.

The errors attributed to the cross sections listed in Tables (4.2.1-3), arise from both statistical and systematic sources. The systematic uncertainty in the cross sections is estimated to be of the order of 15%. The statistical error stated in the tables of the cross sections is inherent in the photon counting procedure used to obtain the fluorescence intensities and also includes a contribution due to laser power fluctuations in the pump laser. The laser power was adjusted to maintain a steady count-rate by setting the dye laser frequency and by adjusting the N<sub>2</sub> laser power to compensate for the deterioration of the laser dye. The pulse-to-pulse jitter was averaged over the 8 hour run time. Error due to 'pile up' was most probably eliminated by maintaining a low count rate of 2-4 pulses per interferometer scan; it was determined experimentally that pile up became negligible at count rates lower than 6 pulses per scan. There were also several sources of systematic error. As it was necessary to introduce a time-delay between excitation and the detection of the fluorescence to avoid the detection of scattered laser light, the experimentally determined intensity ratios had to be appropriately corrected. The correction for the magnetic field perturbation to account for increased mixing between the Zeeman substates affecting the relative intensities of the circularly polarized components emitted from the various states, may also have contributed to the systematic error. The magnetic-field dependence of the Zeeman mixing cross sections was not determined as the experiment was carried out at only one field strength, in order to fully resolve the Zeeman components in the spectra. A field-variation of the Zeeman mixing cross sections may account for systematic differences in the comparison of the experimental data with theoretical calculations, which do not allow for the effects of large Zeeman splitting.



Figure (4.2.1)

Energy level diagram of the  $5^2P$  Zeeman substates in potassium, showing their  $\sigma$  decays to the ground state. Either the  $5^2P_{1/2-1/2}$  or the  $5^2P_{3/2-3/2}$  substate is optically excited. All other substates are populated through collisions.

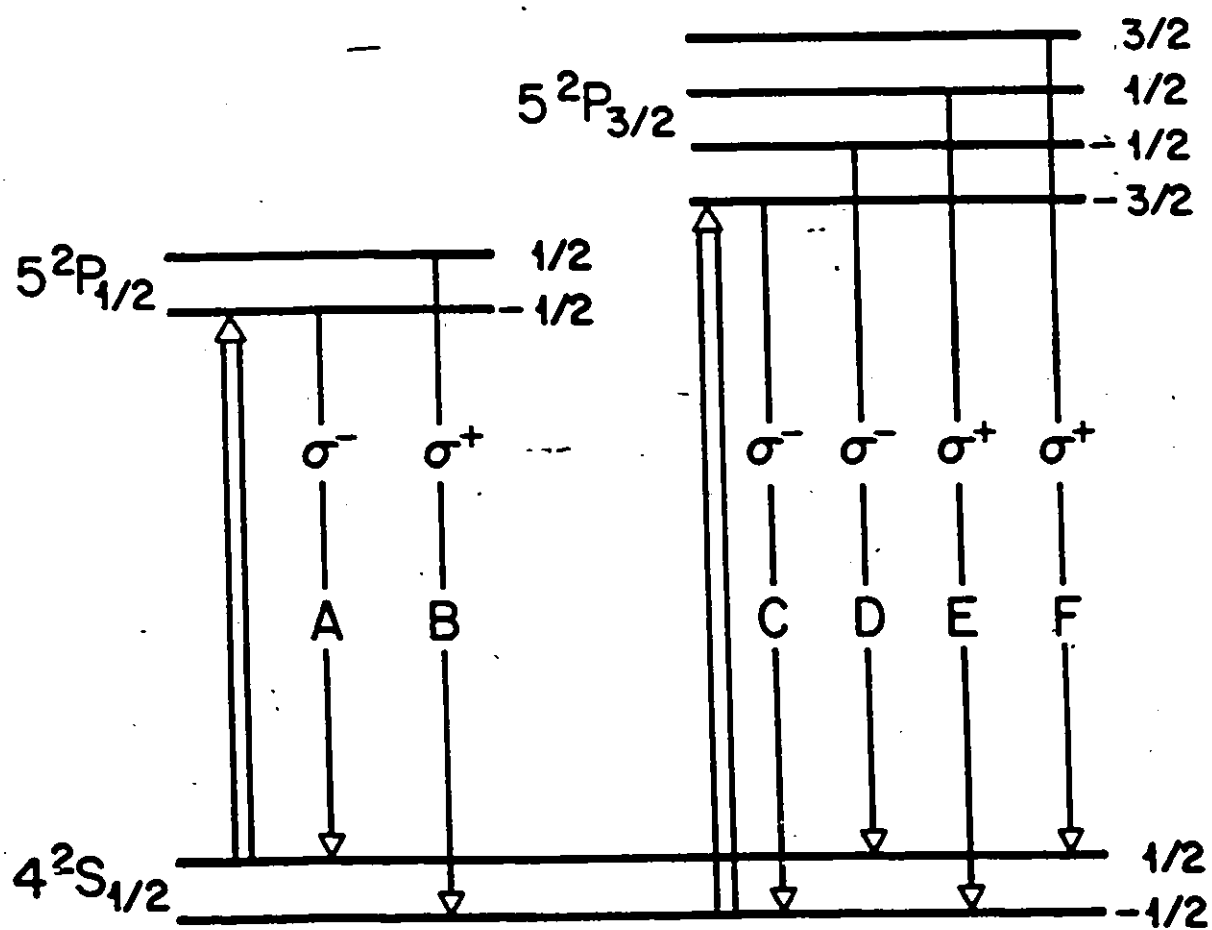
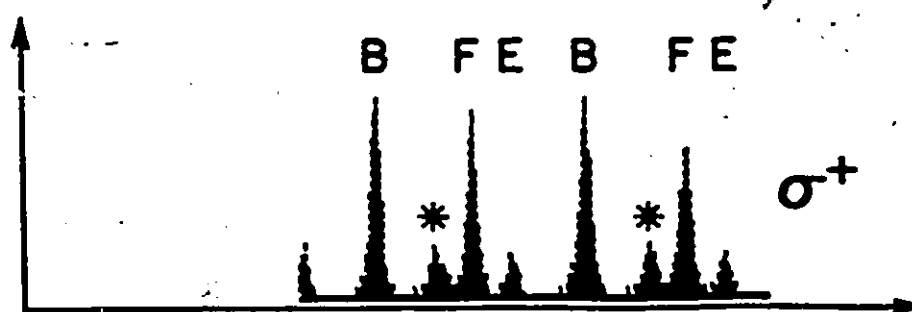
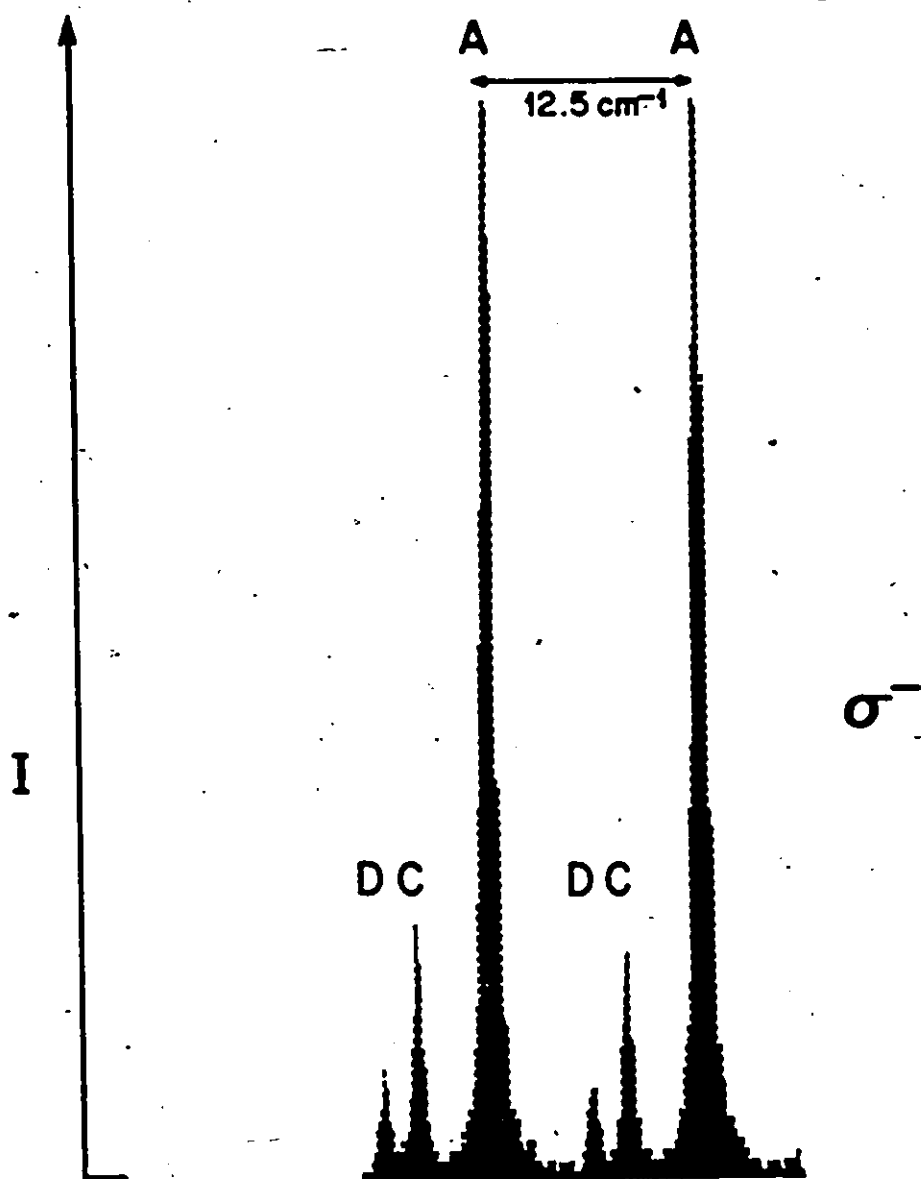


Figure (4.2.2)

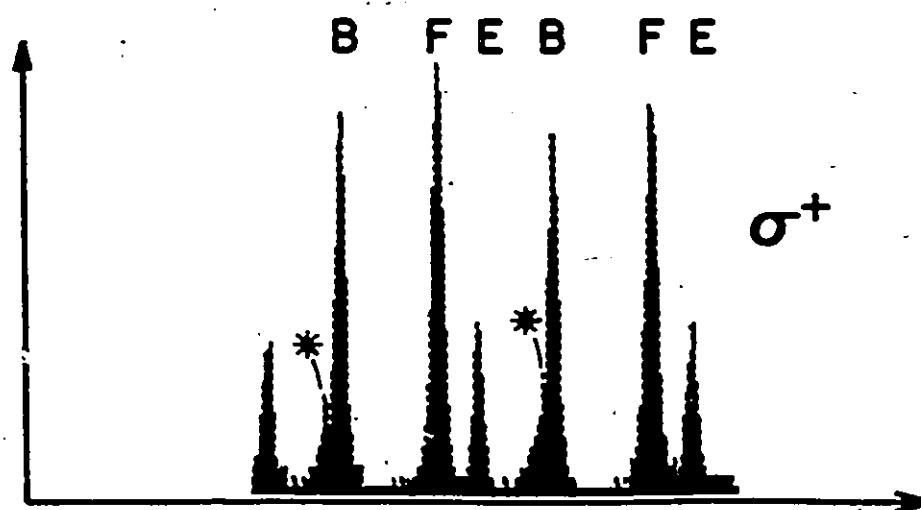
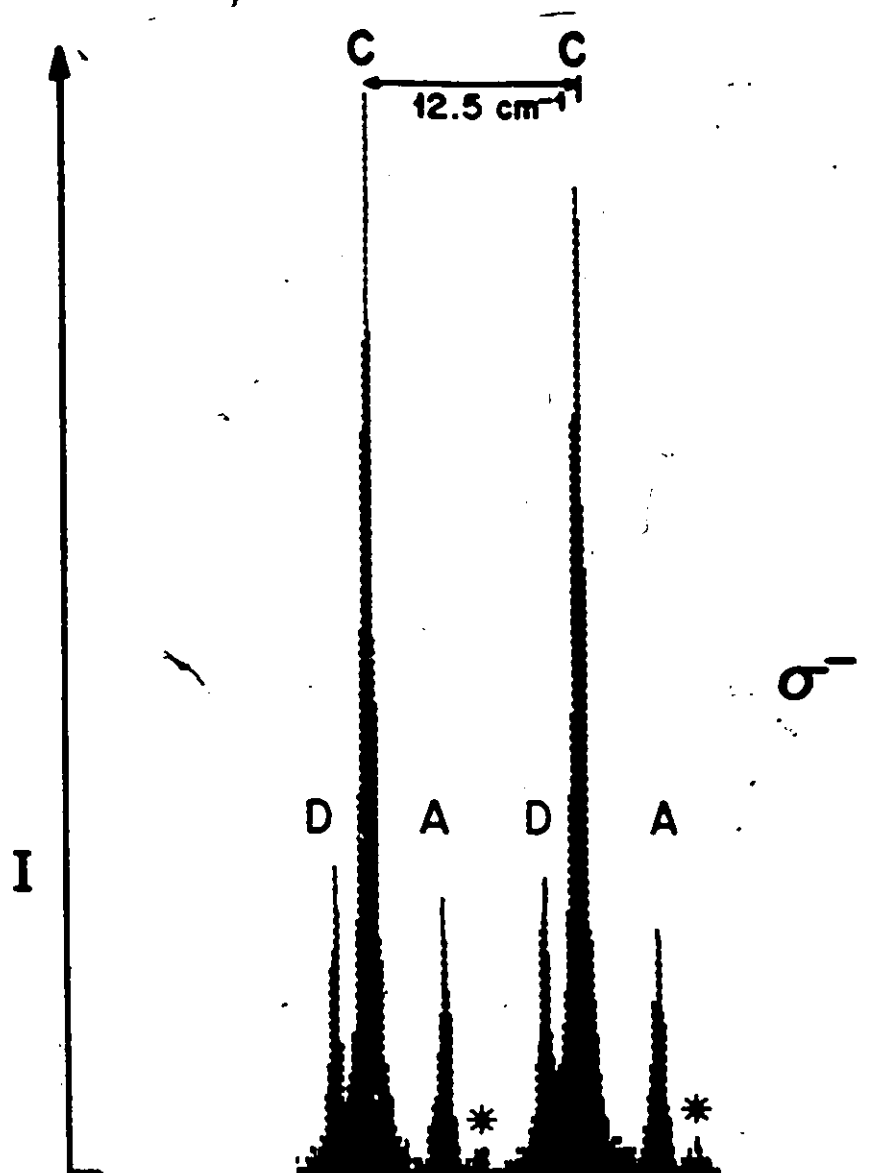
A trace of the Zeeman fluorescence spectrum emitted from potassium vapour mixed with 50 mtorr Ar. The  $5^2P_{1/2-1/2}$  state is optically excited and the peaks are labelled to correspond to the transitions indicated in Fig. (4.2.1). The free spectral range of the interferometer is  $12.5 \text{ cm}^{-1}$ . The asterisks (\*) indicate components due to polarizer leakage.



INTERFEROMETER SCAN

Figure (4.2.3)

A trace of the Zeeman fluorescence spectrum emitted from potassium vapour mixed with 150 mtorr Ne. The  $5^2P_{3/2-3/2}$  state is optically excited and the peaks are labelled to correspond to the transitions indicated in Fig. (4.2.1). The free spectral range of the interferometer is  $12.5 \text{ cm}^{-1}$ . The asterisks (\*) indicate components due to polarizer leakage.



INTERFEROMETER SCAN

Figure (4.2.4)

Plots of the Zeeman fluorescent intensity (and population) ratios arising from  $5^2P_{1/2-1/2}$  excitation, showing effects of mixing induced in K-He collisions. The separate origin for each plot is indicated on the vertical axis. The error bars represent statistical scatter of the measurements. Each point represents the intensity ratio of the specified components, multiplied by the ratio of the appropriate  $A_{ul}$  coefficients.

$\diamond 2.09I(F)/3I(A)$ ;  $\square 2.09I(E)/0.83I(A)$ ;  $\circ 2.09I(C)/3I(A)$ ;  
 $\nabla I(B)/I(A)$ ;  $\triangle 2.09I(D)/0.83I(A)$

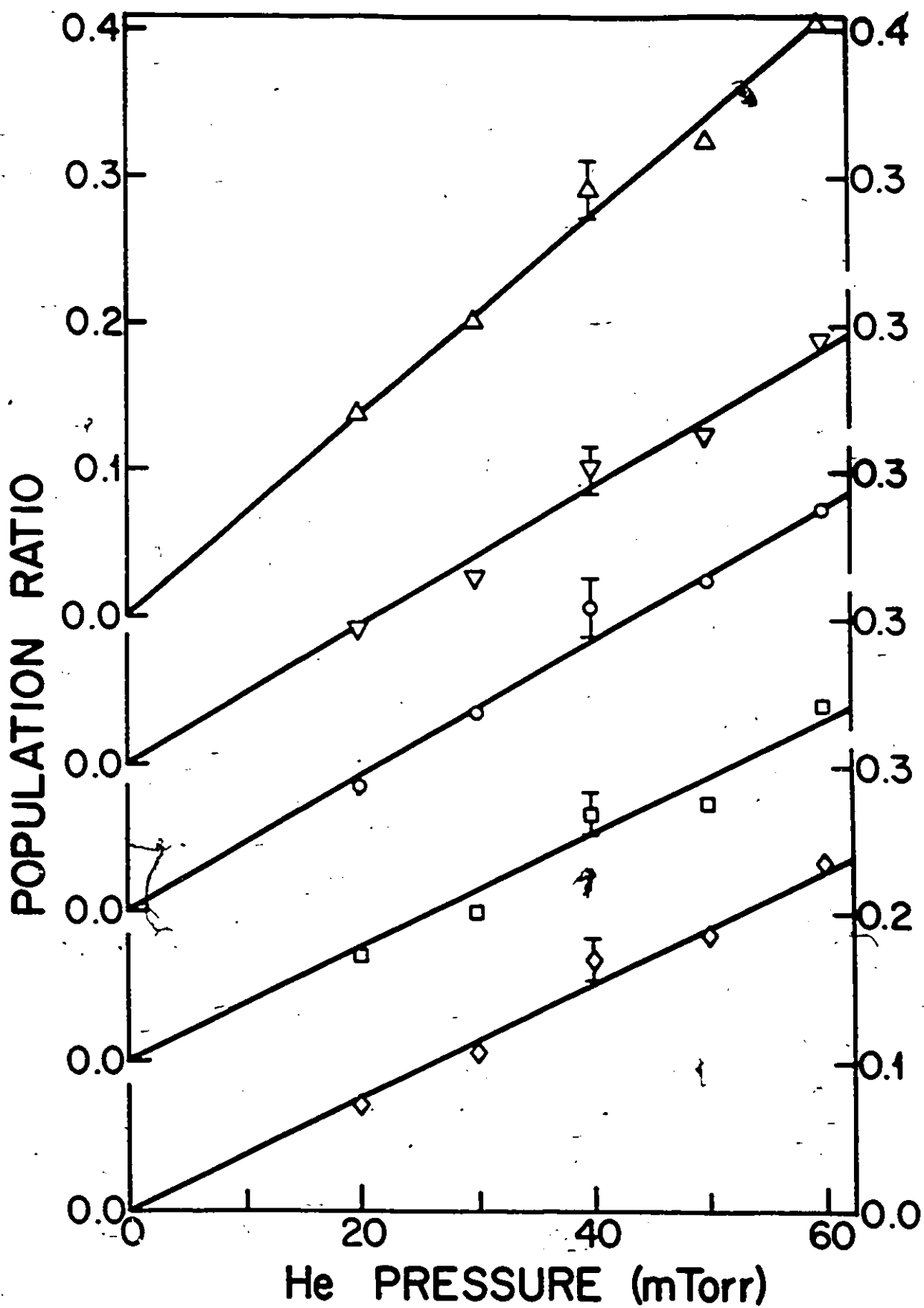




Figure (4.2.5)

Plots of the Zeeman fluorescent intensity (and population) ratios arising from  $5^2P_{3/2-3/2}$  excitation, showing effects of mixing induced in K-He collisions. The separate origin for each plot is indicated on the vertical axis. The error bars represent statistical scatter of the measurements. Each point represents the intensity ratio of the specified components, multiplied by the ratio of the appropriate  $A_{ul}$  coefficients.

◇  $I(F)/I(C)$ ; □  $3I(A)/2.09I(C)$ ; ○  $3I(E)/0.83I(C)$ ;  
▽  $3I(B)/2.09I(C)$ ; △  $3I(D)/0.83I(C)$

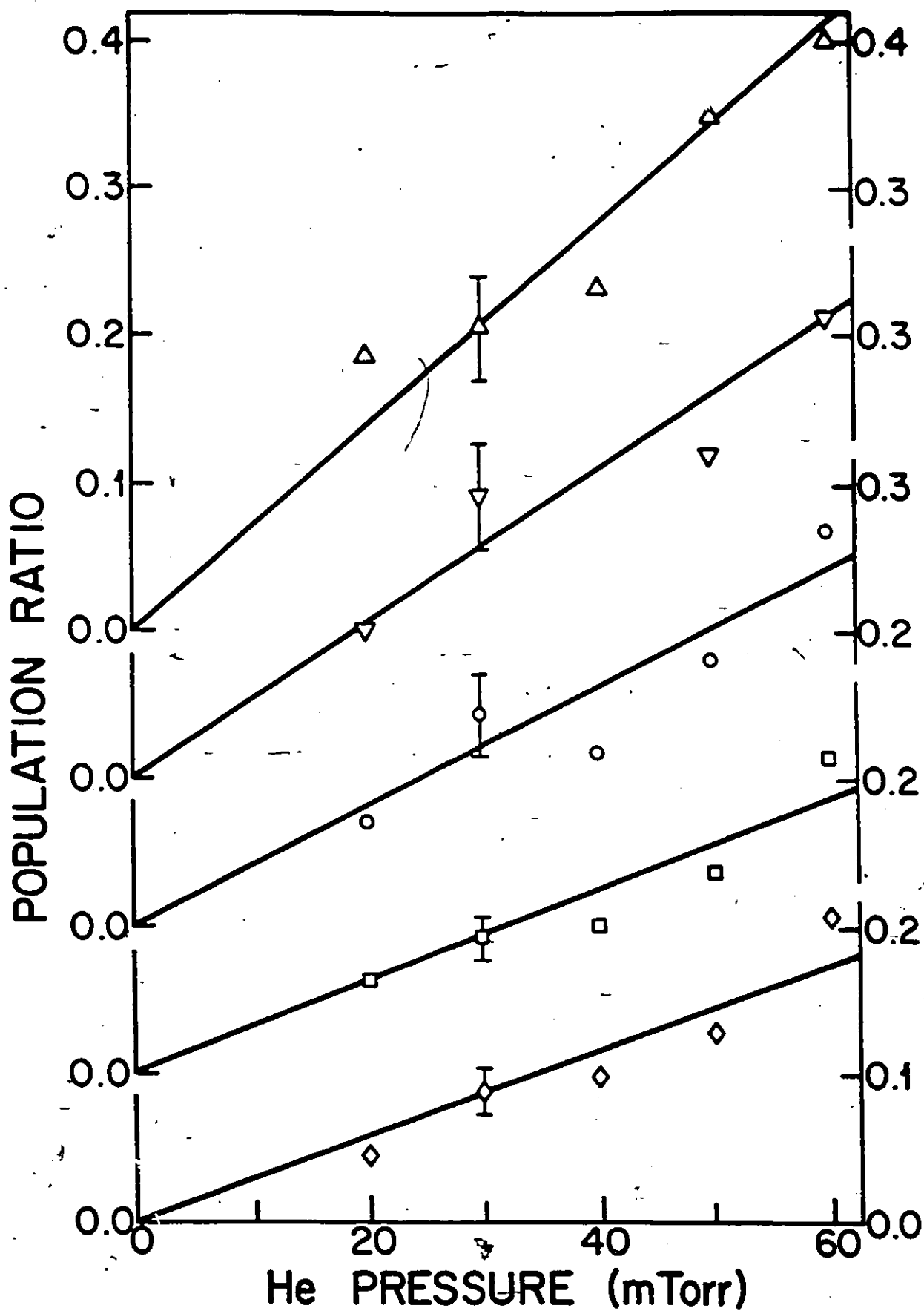


Figure (4.2.6)

Plots of the Zeeman fluorescent intensity (and population) ratios arising from  $5^2P_{1/2-1/2}$  excitation, showing effects of mixing induced in K-Ne collisions. The separate origin for each plot is indicated on the vertical axis. The error bars represent statistical scatter of the measurements. Each point represents the intensity ratio of the specified components, multiplied by the ratio of the appropriate  $A_{ul}$  coefficients.

◇  $2.09I(F)/3I(A)$ ; □  $2.09I(E)/0.83I(A)$ ; ○  $2.09I(C)/3I(A)$ ;  
▽  $I(B)/I(A)$ ; △  $2.09I(D)/0.83I(A)$

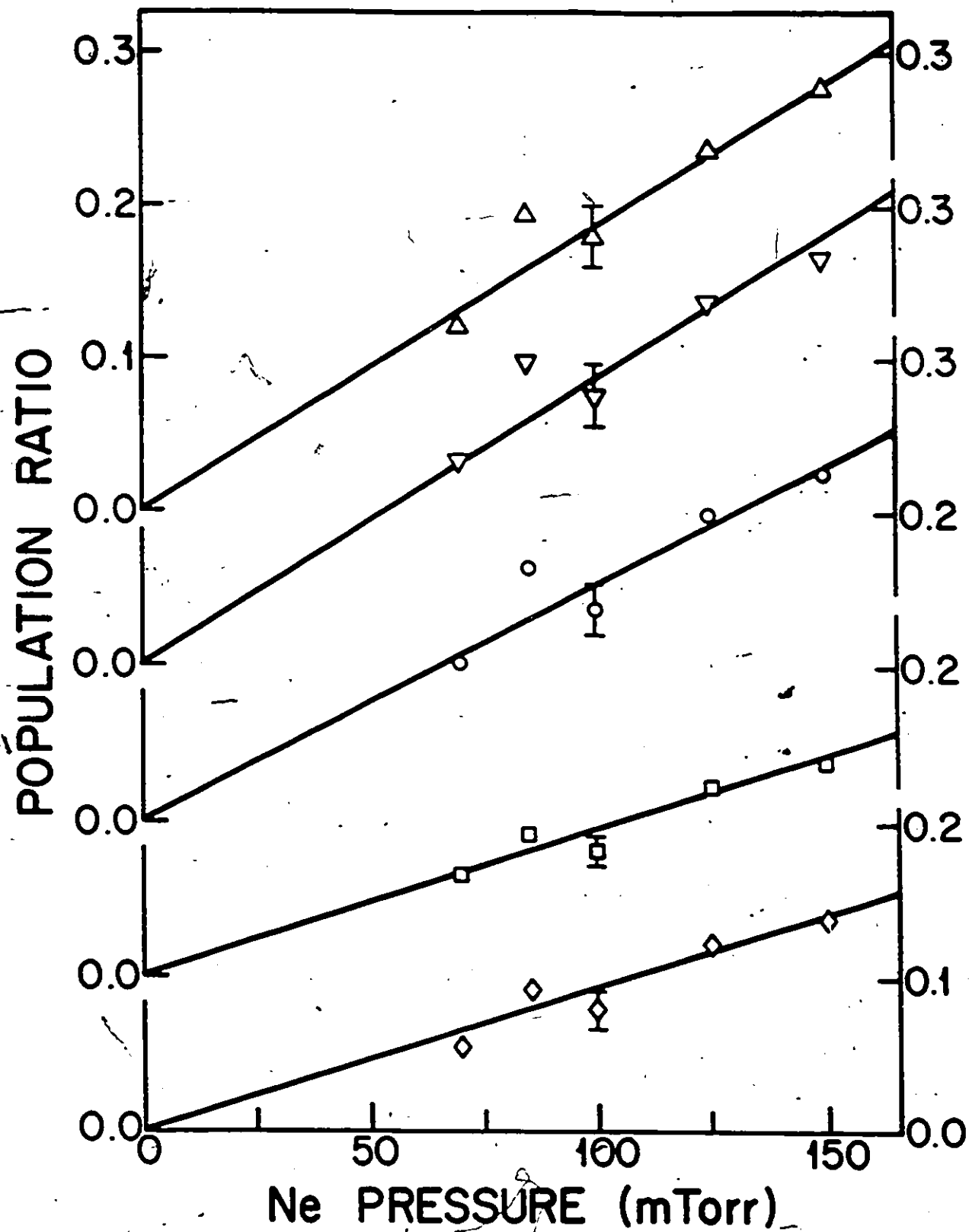


Figure (4.2.7)

Plots of the Zeeman fluorescent intensity (and population) ratios arising from  $5^2P_{3/2-3/2}$  excitation, showing effects of mixing induced in K-Ne collisions. The separate origin for each plot is indicated on the vertical axis. The error bars represent statistical scatter of the measurements. Each point represents the intensity ratio of the specified components, multiplied by the ratio of the appropriate  $A_{ul}$  coefficients.

$\diamond 3I(A)/2.09I(C)$ ;  $\square I(F)/I(C)$ ;  $\circ 3I(B)/2.09I(C)$ ;  
 $\nabla 3I(E)/0.83I(C)$ ;  $\triangle 3I(D)/0.83I(C)$

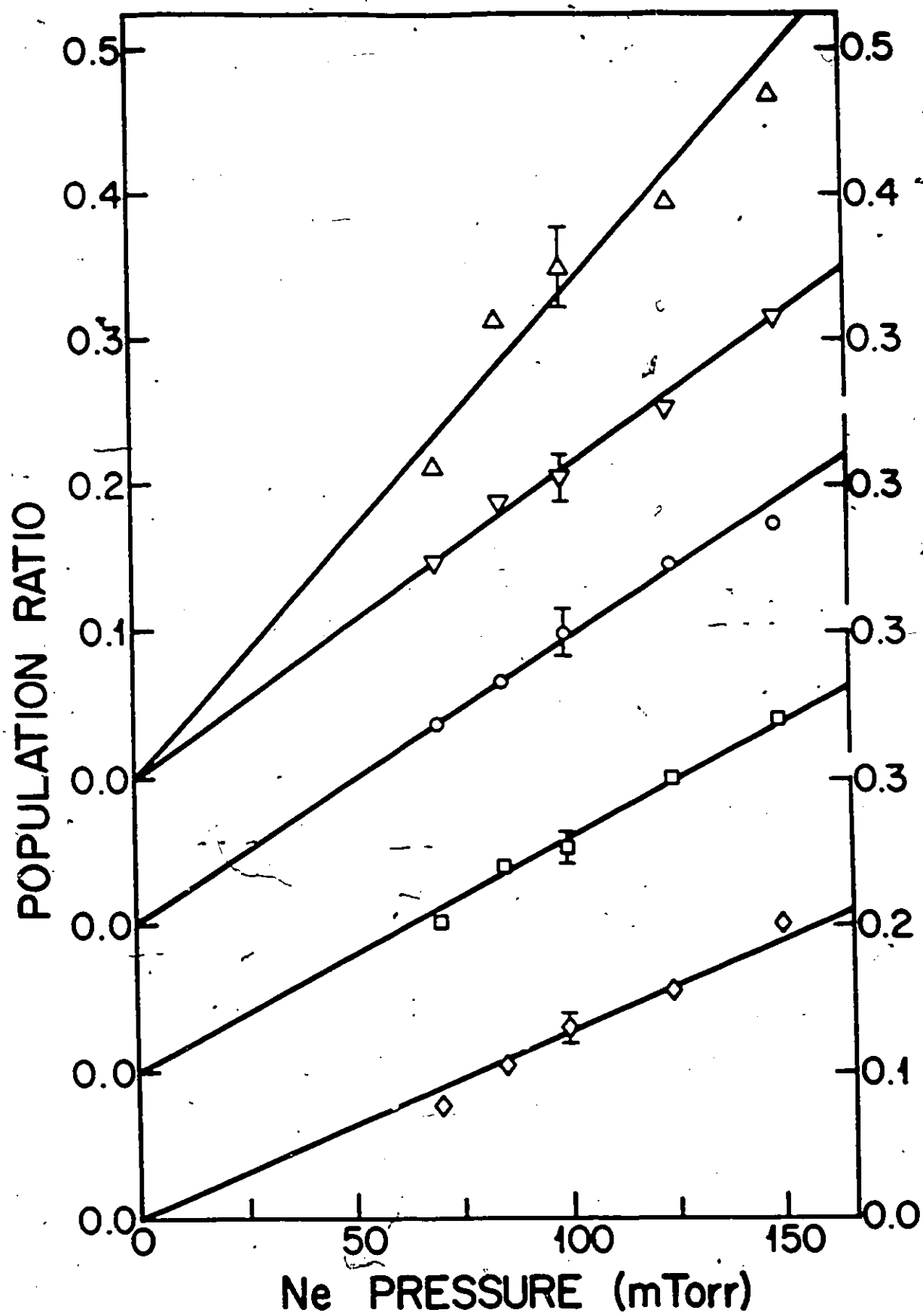


Figure (4.2.8)

Plots of the Zeeman fluorescent intensity (and population) ratios arising from  $5^2P_{1/2-1/2}$  excitation, showing effects of mixing induced in K-Ar collisions. The separate origin for each plot is indicated on the vertical axis. The error bars represent statistical scatter of the measurements. Each point represents the intensity ratio of the specified components, multiplied by the ratio of the appropriate  $A_{ul}$  coefficients.

◇  $2.09I(E)/0.83I(A)$ ; ○  $2.09I(F)/3I(A)$ ; □  $2.09I(C)/3I(A)$ ;  
▽  $I(B)/I(A)$ ; △  $2.09I(D)/0.83I(A)$

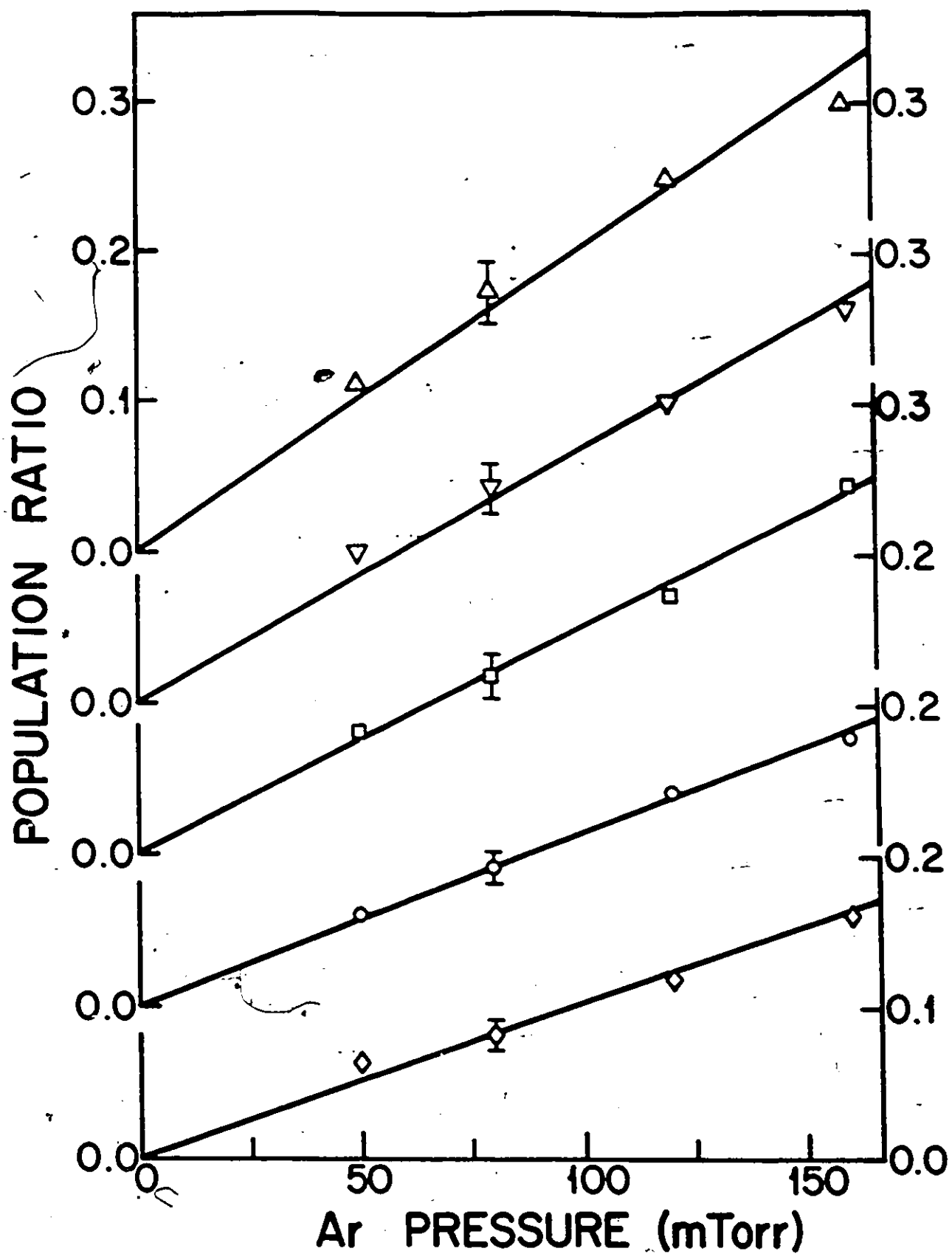




Figure (4.2.9)

Plots of the Zeeman fluorescent intensity (and population) ratios arising from  $5^2P_{3/2-3/2}$  excitation, showing effects of mixing induced in K-Ar collisions. The separate origin for each plot is indicated on the vertical axis. The error bars represent statistical scatter of the measurements. Each point represents the intensity ratio of the specified components, multiplied by the ratio of the appropriate  $A_{ul}$  coefficients.

$\diamond 3I(A)/2.09I(C)$ ;  $\square I(F)/I(C)$ ;  $\nabla 3I(E)/0.83I(C)$ ;  
 $\circ 3I(D)/0.83I(C)$ ;  $\triangle 3I(B)/2.09I(C)$

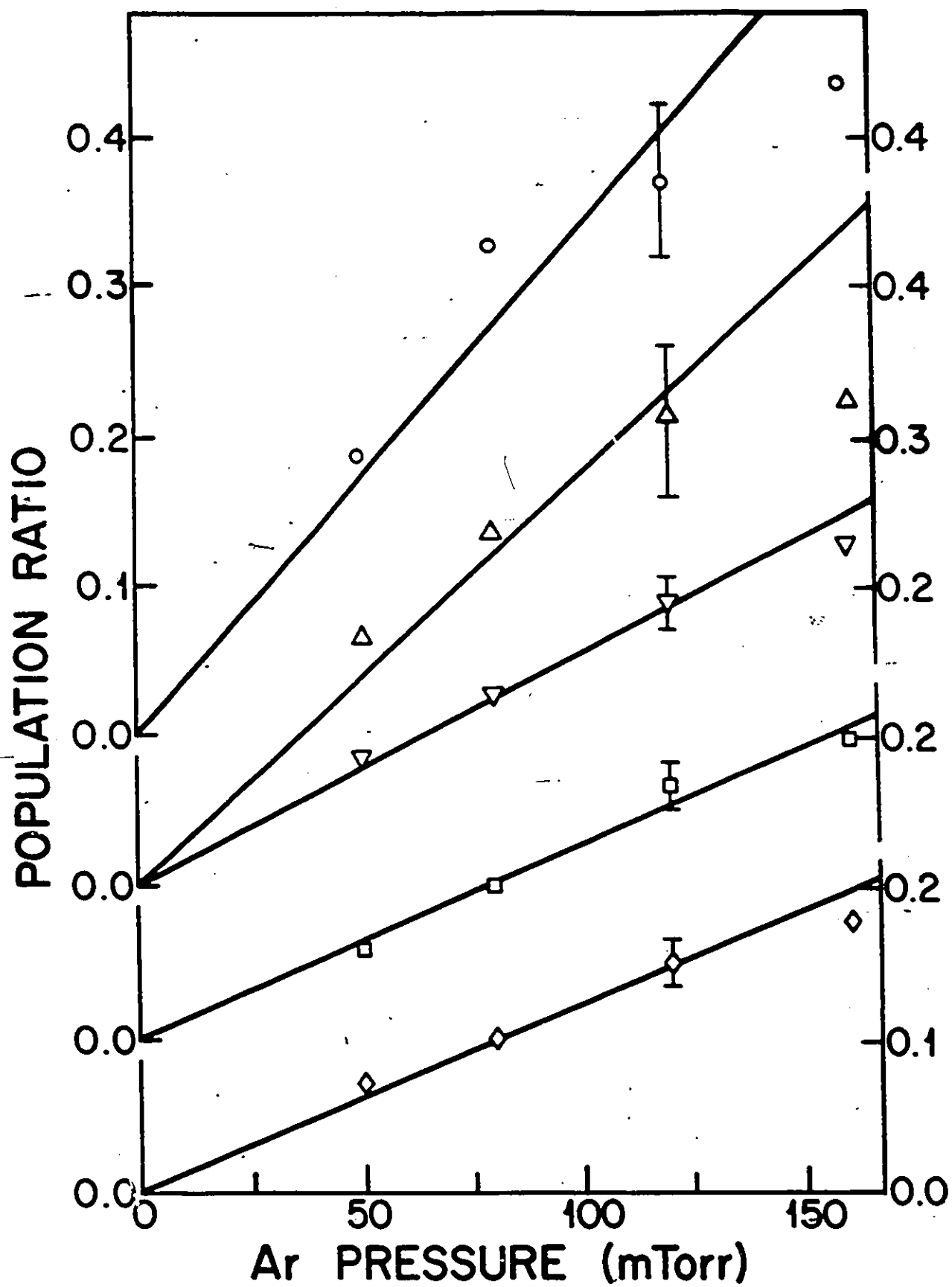


Table (4.2.1) 5P Zeeman Mixing Cross Sections for  
Collisions with He, Ne and Ar.  
 $Q(J,M \rightarrow J',M') (10^{-16} \text{ cm}^2)$

Designation	R	Collision Partner		
		He	Ne	Ar
$Q(1/2-1/2 \rightarrow 1/2+1/2)$	a	95±7	73±9	80±11
	b	74		
	c		63	
$Q(1/2-1/2 \rightarrow 3/2+3/2)$	a	78±6	35±5	54±2
	b	79		
	c		17	
$Q(1/2-1/2 \rightarrow 3/2+1/2)$	a	77±7	36±4	47±6
	b	68		
	c		15	
$Q(1/2-1/2 \rightarrow 3/2-1/2)$	a	139±4	73±8	94±8
	b	56		
	c		14	
$Q(1/2-1/2 \rightarrow 3/2-3/2)$	a	94±7	61±3	68±5
	b	45		
	c		12	
$Q(3/2-3/2 \rightarrow 3/2+3/2)$	a	59±10	61±3	62±5
	b	48		
	c		52	
$Q(3/2-3/2 \rightarrow 3/2+1/2)$	a	80±15	81±3	70±5
	b	108		
	c		101	
$Q(3/2-3/2 \rightarrow 3/2-1/2)$	a	137±26	125±11	142±29
	b	127		
	c		121	
$Q(3/2-3/2 \rightarrow 1/2+1/2)$	a	102±17	74±3	110±26
	b	85		
	c		19	
$Q(3/2-3/2 \rightarrow 1/2-1/2)$	a	62±9	50±4	57±7
	b	48		
	c		13	
$Q(3/2-1/2 \rightarrow 3/2+1/2)$	a	135±34	121±15	157±35
	b	73		
	c		79	

a, This investigation; b, Pascale (1987);  
c, Spielfiedel and Feautrier (1988)  
n.b.: The error limits represent the statistical  
scatter of the data.

TABLE (4.2.2) 5P Fine-Structure Mixing and Orientation  
Transfer Cross Sections ( $10^{-10} \text{cm}^2$ )

Designation	r e f	Collision Partner		
		He	Ne	Ar
$\sigma_{12}^0 \left( \frac{1}{2} \Rightarrow \frac{3}{2} \right)$	a	274*20	145*14	186*15
	b	397*59	139*20	224*32
	c	156	77	139
	d	174		
	e		41	
$\sigma_{21}^0 \left( \frac{3}{2} \Rightarrow \frac{1}{2} \right)$	a	232*37	175*10	236*47
	b	376*55	139*25	216*31
	d	187		
	e		45	
$\sigma_{12}^1 \left( \frac{1}{2} \Rightarrow \frac{3}{2} \right)$	a	35*16	36*12	28*11
	c	-66	-22	-52
	d	-36		
	e		-5	
$\sigma_{21}^1 \left( \frac{3}{2} \Rightarrow \frac{1}{2} \right)$	a	-41*27	-26*7	-56*35
	d	-39		
	e		-6	

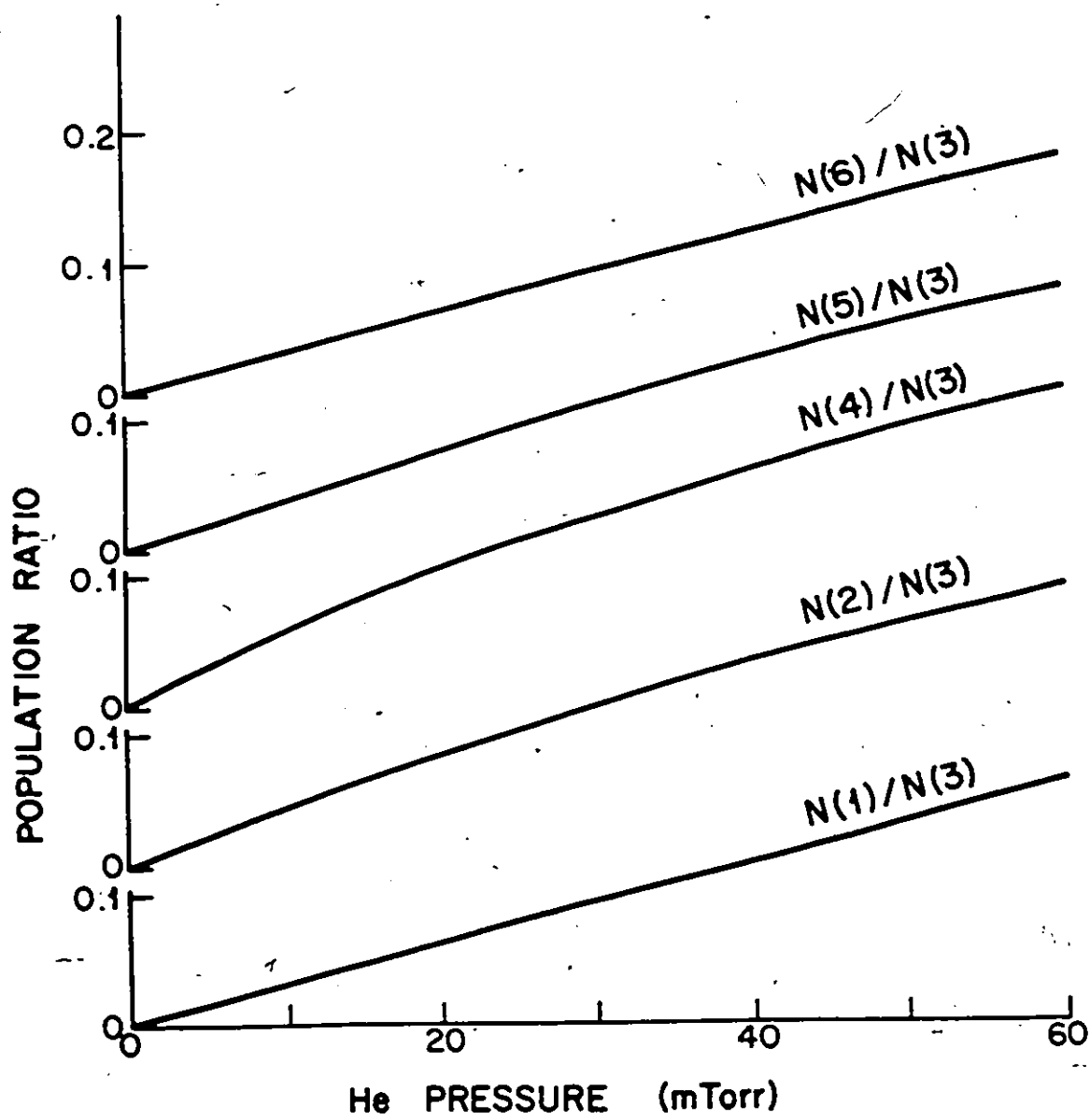
a, This experiment 70 kG; b, This experiment zero field;  
c, Spielfiedel et al. (1979); d, Pascale (1987);  
e, Spielfiedel and Feautrier (1988)  
n.b. The error limits represent the statistical scatter  
of the data.

TABLE (4.2.3) 5P Multipole Relaxation Cross Sections ( $10^{-16} \text{cm}^2$ )				
DESIGNATION	R e f.	Collision Partner		
		He	Ne	Ar
$\Lambda_{1/2}^{(1)}$	a	190 $\pm$ 14	145 $\pm$ 18	160 $\pm$ 22
	b	40.5	258	109
	c	149		
	d		125	
$\Lambda_{3/2}^{(1)}$	a	316 $\pm$ 57	314 $\pm$ 17	312 $\pm$ 46
	b	155	340	253
	c	325		
	d		321	
$\Lambda_{3/2}^{(2)}$	a	434 $\pm$ 82	411 $\pm$ 28	425 $\pm$ 68
	b	256	725	504
	c	471		
	d		445	
$\Lambda_{3/2}^{(3)}$	a	506 $\pm$ 154	462 $\pm$ 56	551 $\pm$ 136
	b	236		438
	c	388		
	d		387	
Ref.: a, this experiment; b, Spielfiedel et al. (1979); c, Pascale (1987); d, Spielfiedel and Feautrier (1988). n.b. The error limits represent the statistical scatter of the data.				

Figure (4.2.10)

Plots of the Zeeman population ratios obtained from a computer simulation of the relaxation of the 5P Zeeman manifold, showing the effects of mixing induced in K-He collisions. The  $5^2P_{3/2-3/2}$  Zeeman substate was optically excited. The separate origin for each ratio is indicated on the vertical axis. The population densities of the Zeeman substates are labelled as follows;

$$\begin{aligned} N(1) &= (1/2 - 1/2); \quad N(2) = (1/2 + 1/2); \quad N(3) = (3/2 - 3/2); \\ N(4) &= (3/2 - 1/2); \quad N(5) = (3/2 + 1/2); \quad N(6) = (3/2 + 3/2). \end{aligned}$$



5  
Figure (4.2.11)

Plots of multipole relaxation rates  $\lambda_{ij}^{(n)}$  against  $Nv, \tau$  for He (see eqs. (2.2.98-99)). The slopes of the plots correspond to the multipole relaxation cross sections. The K coefficients were determined with the experimental Zeeman mixing cross sections presented in Table (4.2.1) assuming single collision conditions.

A:  $\lambda_{11}^{(1)}$

B:  $\lambda_{22}^{(1)}$

C:  $\lambda_{22}^{(2)}$

D:  $\lambda_{22}^{(3)}$



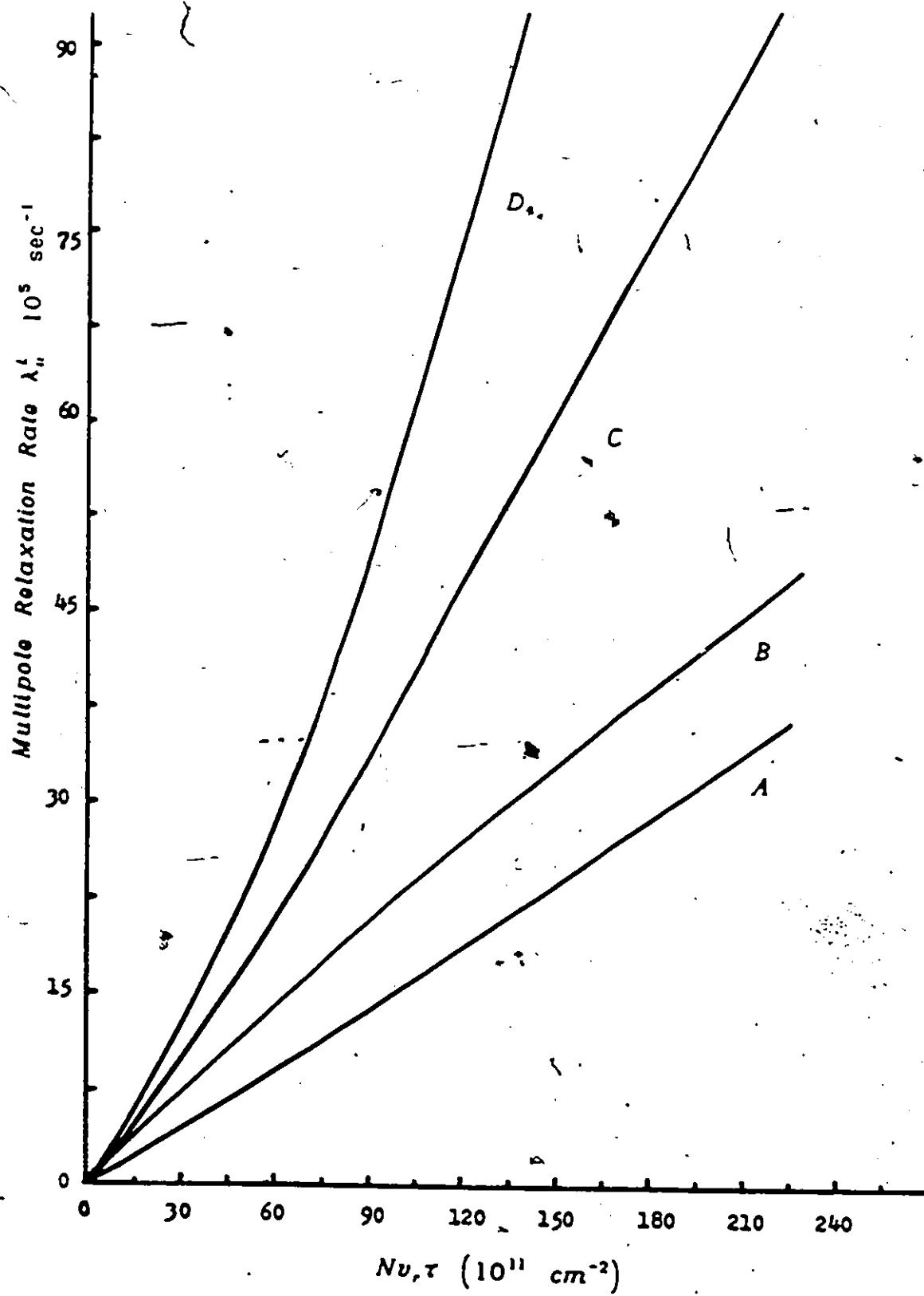


Figure (4.2.12)

Plots of multipole relaxation rates  $\lambda_{ii}^{(l)}$  against  $Nv, \tau$  for He (see eqs. (2.2.98-99)). The slopes of the plots correspond to the multipole relaxation cross sections. The K coefficients were determined with the theoretical Zeeman mixing cross sections (Pascale 1987) presented in Table (4.2.1) assuming single collision conditions.

- A:  $\lambda_{11}^{(1)}$
- B:  $\lambda_{22}^{(1)}$
- C:  $\lambda_{22}^{(2)}$
- D:  $\lambda_{22}^{(3)}$

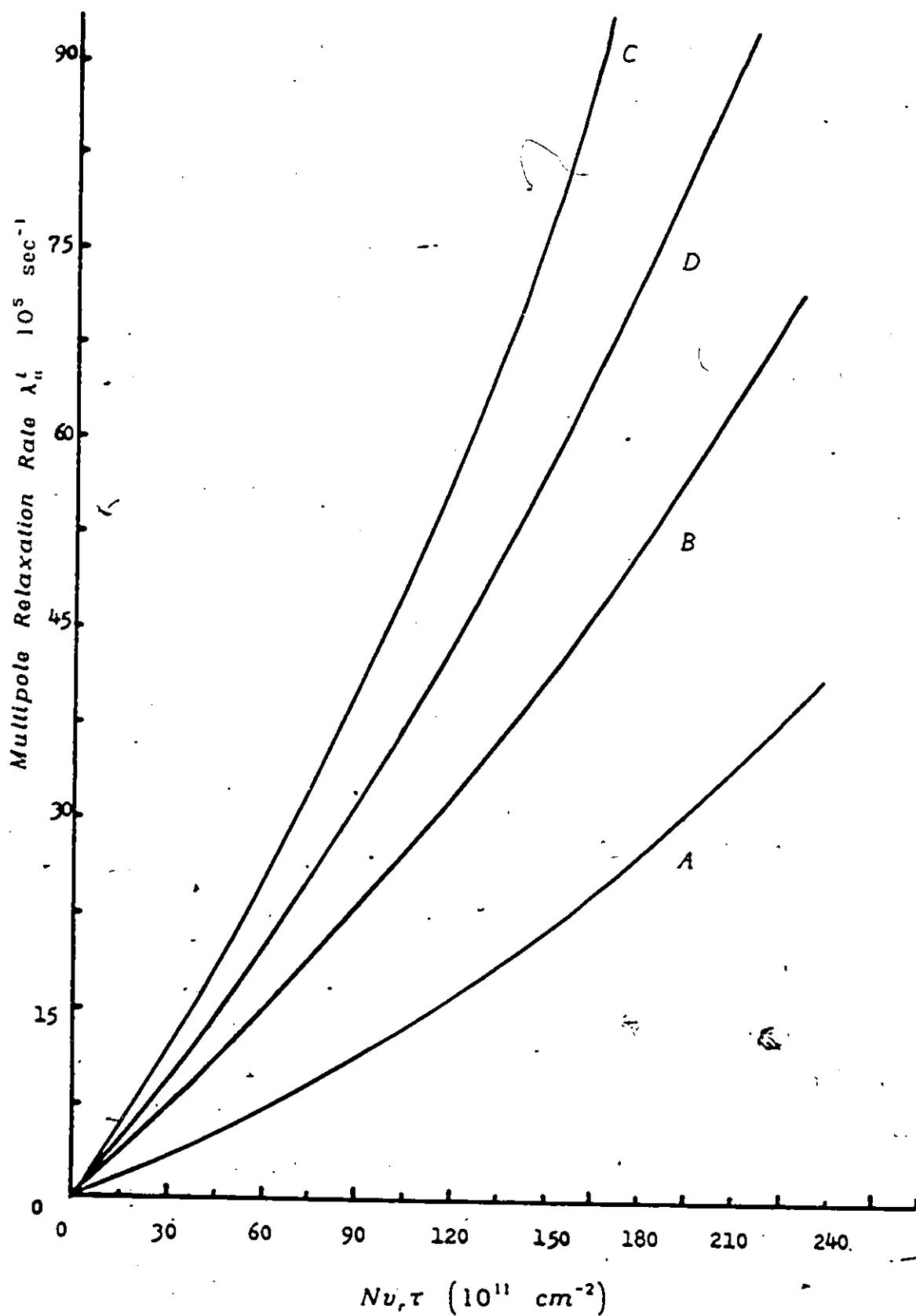


Figure (4.2.13)

Plot of eqs. (2.2.100-101) for He. The Zeeman mixing cross sections determined experimentally were used to predict the K coefficients for these plots assuming single collision conditions. These equations are of the form  $Y=A+BX$ , where A, the low pressure intercept is the inverse of the multipole relaxation cross section and the slope is a measure of the degree of curvature of the plots shown in Fig. (2.2.11).

- A:  $\lambda_{11}^{(1)-1}$
- B:  $\lambda_{22}^{(1)-1}$
- C:  $\lambda_{22}^{(2)-1}$
- D:  $\lambda_{22}^{(3)-1}$

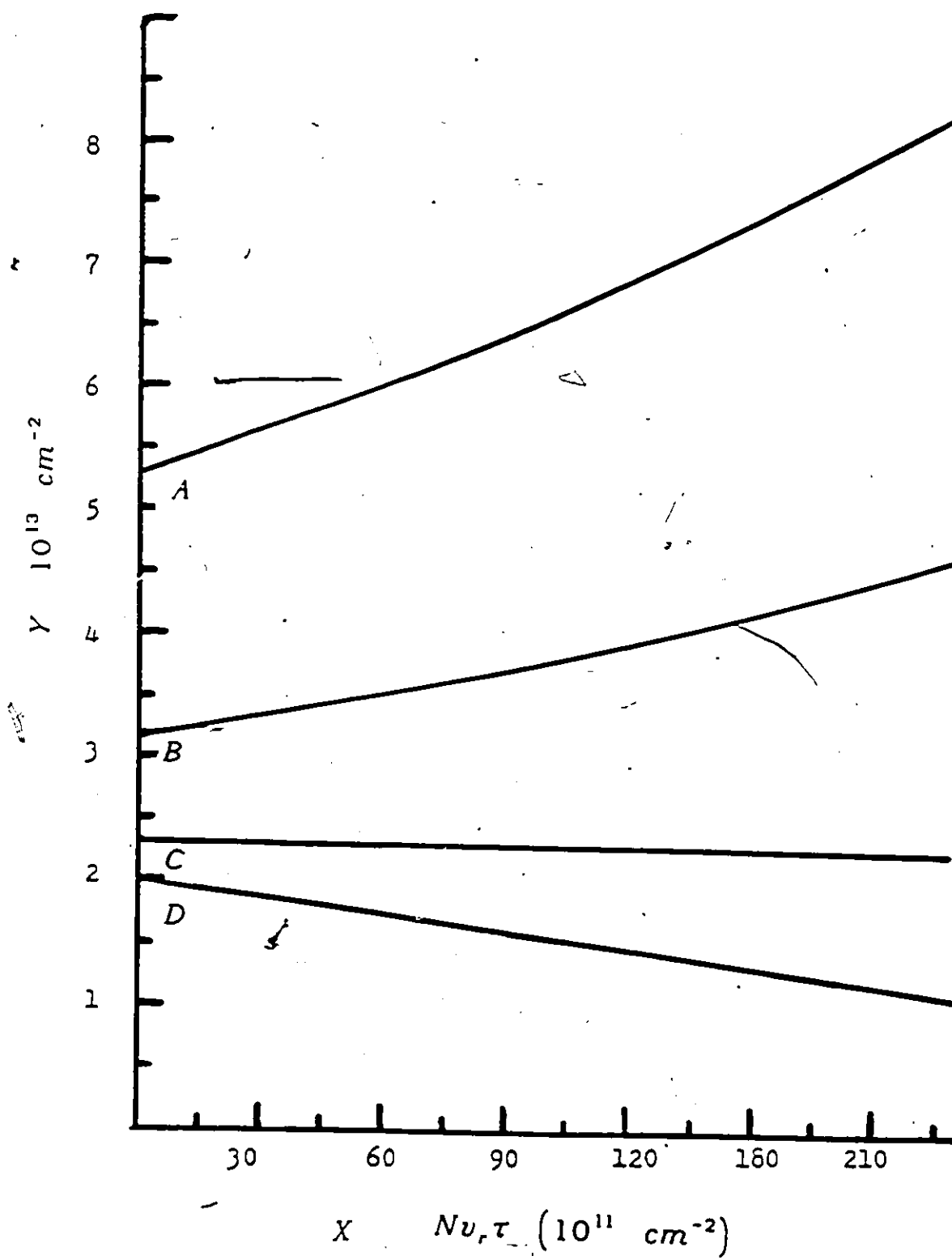
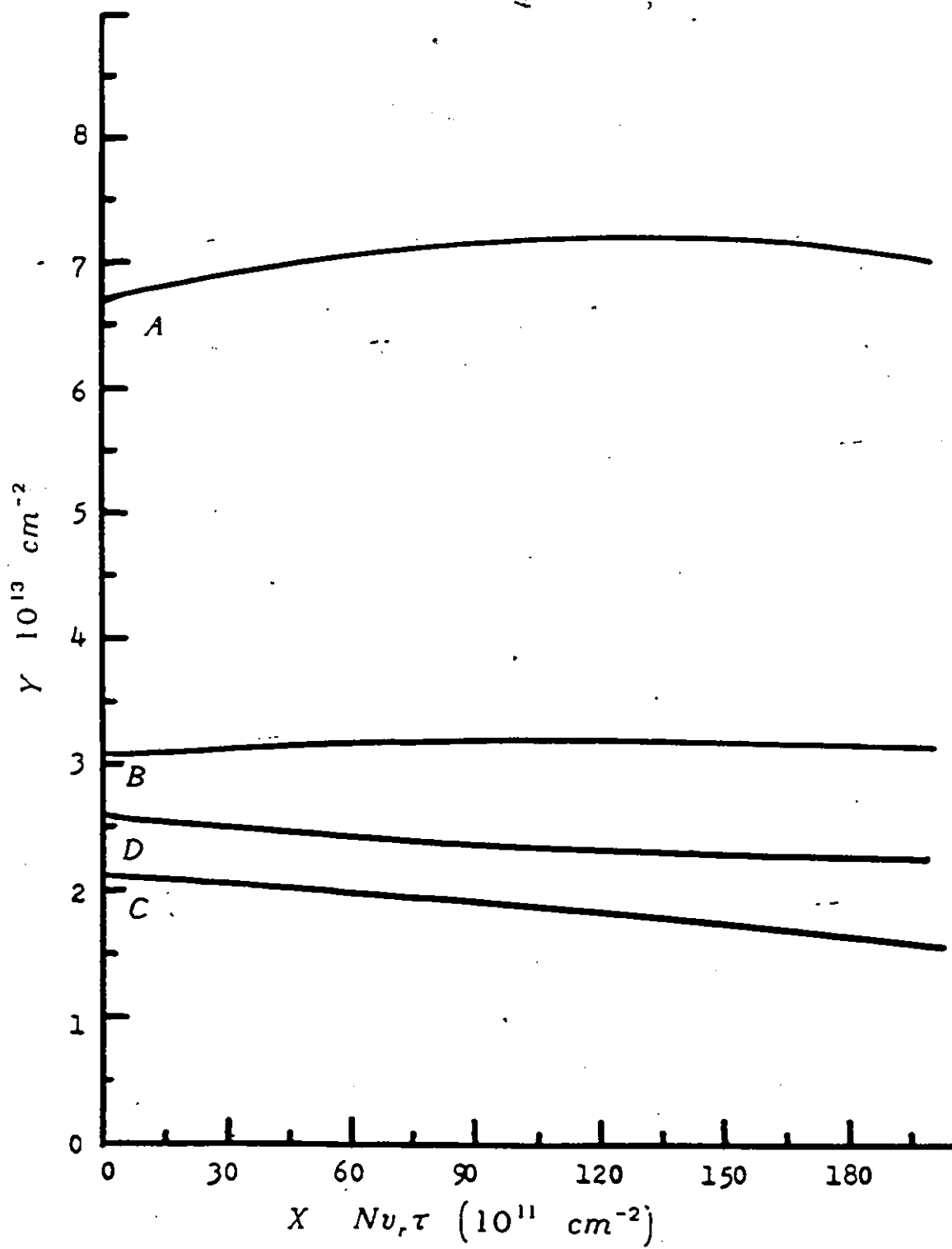


Figure (4.2.14)

Plot of eqs. (2.2.100-101) for He. The calculated Zeeman mixing cross sections (Pascale 1987) were used to predict the K coefficients for these plots assuming single collision conditions. These equations are of the form  $Y=A+BX$ , where A, the low pressure intercept is the inverse of the multipole relaxation cross section and the slope is a measure of the rate of curvature of the plots shown in figure (2.2.12).

- A:  $\Lambda_{11}^{(1)-1}$
- B:  $\Lambda_{22}^{(1)-1}$
- C:  $\Lambda_{22}^{(2)-1}$
- D:  $\Lambda_{22}^{(3)-1}$



#### 4.3 Radiative Lifetimes of the 5P, 6P and 7P Fine-structure States of Potassium

A semilogarithmic plot of the fluorescence time-decay spectrum, representing the decay of the  $7^2P_{1/2}$  state is shown in Fig. (4.3.1). This was the most difficult of the spectra to record, as the transition has the smallest oscillator strength and the 7P atoms are relatively easily photoionized because of the short wavelength of the pump radiation. It may be seen that the plot is linear and free from modulation (on the average the signal-to-noise ratio exceeded 200). The first 30 channels show a small non-linearity attributed to a photoionization cascade which could not be completely eliminated. The lifetimes were calculated from the data recorded in time segments where these effects were considered negligible. For each fs state several (4-15) experimental runs were carried out, to test the consistency of the data and probe the temperature-dependence of the lifetimes.

The lifetime of the excited state was calculated from the experimental data by a weighted least squares fit to a single exponential decay constant (Bevington, 1969). The spectra were corrected for a small contribution of electronic noise accumulated over the 3-6 hour recording times, by subtracting a constant background (noise) which, for the 5P state, was determined from the average of the signal recorded in the last 50 channels, representing the fluorescence and noise detected after 14 lifetimes of the 5P state. The noise correction, on average, amounted to 5 counts per channel for the 5P and 6P states and 20 counts per channel for the 7P state which required the longest data acquisition times.



The lifetimes were calculated from the data at various time intervals and over various time periods along the fluorescence decay path (this was done in a random fashion through computer iteration of the data). Each value was calculated with an associated  $\chi^2$  fit and the most linear fits corresponding to the largest time span of the data were chosen as the most representative. The stated limits of error represent the standard deviations  $\sigma$  of the measured values calculated from several (n) experimental runs. The systematic error due to the background and to the cascades is estimated to fall within the stated error limits.

The lifetimes are listed in table (4.3.1) for the 5P, 6P and 7P fs states together with experimental and theoretical values reported elsewhere. The experimental values reported by Svanberg (1971), Ney (1969) and Schmeider et al. (1968) were determined using level crossing techniques. The present experimental lifetimes are in good agreement with those of Svanberg who employed the Hanle effect to measure the lifetimes and the hyperfine coupling constants for these states. The limits of error assigned by the various authors appear in the table along with the temperature at which the lifetimes were determined. The errors assigned to the 5P and 6P states are rather low in view of the authors' stated difficulties in fitting a theoretical curve to experimental data which exhibited a relatively low signal-to-noise ratio (Svanberg 1971).

In most cases the theoretically determined lifetimes (none of which shows the respective limits of error) agree with those found experimentally. The theoretical calculations were performed by various methods. Grudzev et al. (1982) used a numerical coulomb approximation (NCA) calculation based on a semi-empirical method employing an effective orbital parameter. Wiese et al. (1969) also used

an NCA method correcting for spin-orbit interaction in determining the transition probabilities whose sum yielded the lifetimes shown in the table. Theodosiou (1984) employed the Bates-Damgaard approximation method with corrections for core-polarization, spin-orbit interaction and blackbody radiation. The theoretical temperature correction for the effect of blackbody radiation on the lifetime of the P states has been listed in table (4.3.1) for the 0, 355 and 600 K. The experimental data is listed with the temperature employed. A study of the temperature dependence of the lifetime of the 6P states was undertaken over a limited range as listed in the table. The effect of increased temperature on the lifetime due to quenching caused by higher potassium density and by stimulated emission due to increased blackbody radiation was not found to be experimentally significant. A recent study by Hart (1983) of the potassium S and D states also showed the temperature variation of the lifetime to be insignificant over a similar temperature range.

The values calculated by Theodosiou are not in as good agreement with the experimental data as are some of the other experimental and theoretical results (Svanberg 1971, Grudzev and Denisov 1982). In particular the blackbody correction seems to have been overestimated and the lifetimes of all the states are consistently lower than the measured values, but the difference between the  $P_{1/2}$  and the  $P_{3/2}$  lifetimes is in agreement with the experimental observations. It should also be noted that the theoretical calculations of the S and D lifetimes reported by D.Hart and Atkinson who employed Warners' method corrected for blackbody radiation, are in somewhat better agreement with their own experimental measurements than are the calculations of Theodosiou.

Figure (4.3.1)

A semilogarithmic plot of fluorescent intensity against time showing the decay of the  $^{72}\text{P}_{1/2}$  state.

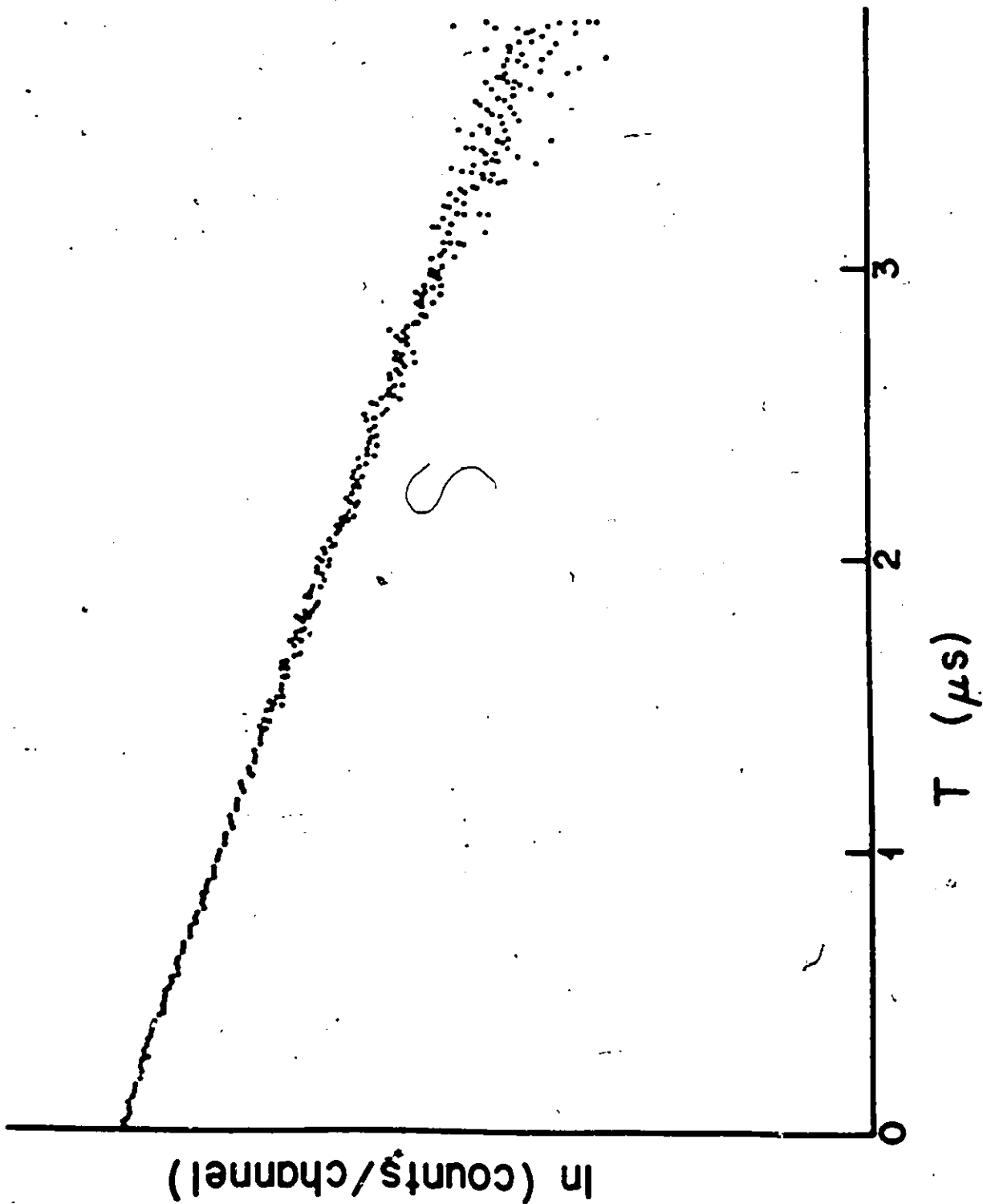


Table (4.3.1) Lifetimes of the 5P, 6P and 7P States in Potassium (ns)				
Level	n	Lifetime (ns)	Ref.	Temperature (K)
$5^2P_{1/2}$	10	137*2 ex.	*	372
		130 cal.	2	0
		127.06 cal.	3	0
		127.05 cal.	3	355
		126.86 cal.	3	600
		138 cal.	6	0
		122 cal.	8	
$5^2P_{3/2}$	12	134*2 ex.	*	372
		133*3 ex.	1	353
		130 cal.	2	0
		124.02 cal.	3	0
		124.02 cal.	3	355
		123.82 cal.	3	600
		120*4 ex.	4	363
		140.8*4 ex.	5	n.a.
		135 cal.	6	0
		118 cal.	8	
$6^2P_{1/2}$	8	344*3 ex.	*	432;378;355
		320 cal.	2	0
		321.67 cal.	3	0
		319.86 cal.	3	355
		306.33 cal.	3	600
		298 cal.	7	0
		437 cal.	8	
$6^2P_{3/2}$	15	333*3 ex.	*	432;369;355
		310*15 ex.	1	403
		315 cal.	2	0
		312.77 cal.	3	0
		311.04 cal.	3	355
		298.21 cal.	3	600
		300 cal.	7	0
		412 cal.	8	
$7^2P_{1/2}$	4	626*6 ex.	*	431
		620 cal.	2	0
		619.47 cal.	3	0
		590.93 cal.	3	355
		523.75 cal.	3	600
$7^2P_{3/2}$	7	595*6 ex.	*	431
		600 cal.	2	0
		601.8 cal.	3	0
		574.8 cal.	3	355
		511.19 cal.	3	600

n = number of measurements

References :

- (\*) = This work.
- (1) Svanberg (1971)
- (2) Grudzev and Denisov (1982)
- (3) Theodosiou (1984)
- (4) Ney (1969)
- (5) Schmieder et al. (1968)
- (6) Wiese et al. (1969) (transition probabilities)
- (7) Heavens (1961)
- (8) Warner (1968) (gf values)

## 5 CONCLUSIONS

This dissertation describes a set of experiments dealing with the radiative and collisional relaxation of the 5P, 6P and 7P states of potassium, as well the apparatus and techniques developed for this investigation. The collisional interactions of selectively excited 5P potassium atoms with noble gas atoms at thermal energies have been investigated both in zero magnetic field and in a field of 70 kG. The experimental data have yielded the cross sections for fs mixing, Zeeman mixing and multipole relaxation. The radiative lifetimes of the individual 5P, 6P and 7P fs substates have been measured using methods of time-resolved fluorescence spectroscopy. The design, construction and operation of an improved Fizeau wavemeter and a potassium thermionic diode for accurate laser wavelength tuning have also been described.

The fs mixing and multipole relaxation experiments were accomplished using a photon-counting technique synchronized to the firing of a pulsed laser and the scanning of a high-resolution Fabry-Perot interferometer. Measurements of the relative intensities of the spectral components allowed the determination of cross sections for the collisional excitation transfer. The small fs splitting of the 5P state and the large Zeeman splitting at 70 kG result in the non-negligible mixing of the fs Zeeman substates, which complicates the interpretation of the data. The determination of the absolute multiple relaxation cross sections involves the consideration of experimental error propagation and the interpretation of the derived rates equations. The proper measure of the cross sections requires the extrapolation of the data to low buffer gas pressure. The various cross sections determined in the experiment are

listed in Tables (4.2.1-3). This study is believed to be the first direct experimental determination of all the multipole-relaxation cross sections for a state lying above the resonance state in an alkali-metal atom, for collisions with noble-gas atoms.

The measurements of the 5P, 6P and 7P fs lifetimes are in good agreement with theoretical predictions and with previous experimental data, where available. The lifetimes determined as part of this investigation are presented in Table (4.3.1).

An improved wavemeter for cw and pulsed laser wavelength measurements, incorporating single-mode optical fibre coupling was developed as part of this investigation. It is capable of wavelength measurements with an accuracy better than 2 parts in  $10^6$ . A potassium thermionic diode was also developed to allow rapid and accurate dye-laser tuning to the various excited states of potassium.



## 6 APPENDIX A

### Zeeman Splitting of the P and D States

The hyperfine-structure of the potassium atoms placed in a strong magnetic field exhibits a complete Paschen-Back effect, with the Zeeman substate energy displacement,  $\Delta E$ , of each substate given by (Woodgate 1980):

$$\Delta E = g_j \mu_B B m_j \quad (6.1)$$

Expressing eq. (6.1) in terms of the frequency difference  $\Delta \nu$  in wavenumbers ( $\text{cm}^{-1}$ ):

$$\Delta \nu = 4.669 \times 10^{-5} B m_j g_j \quad (6.2)$$

where B is the magnetic field in gauss and  $g_j$  is the Landé g factor:

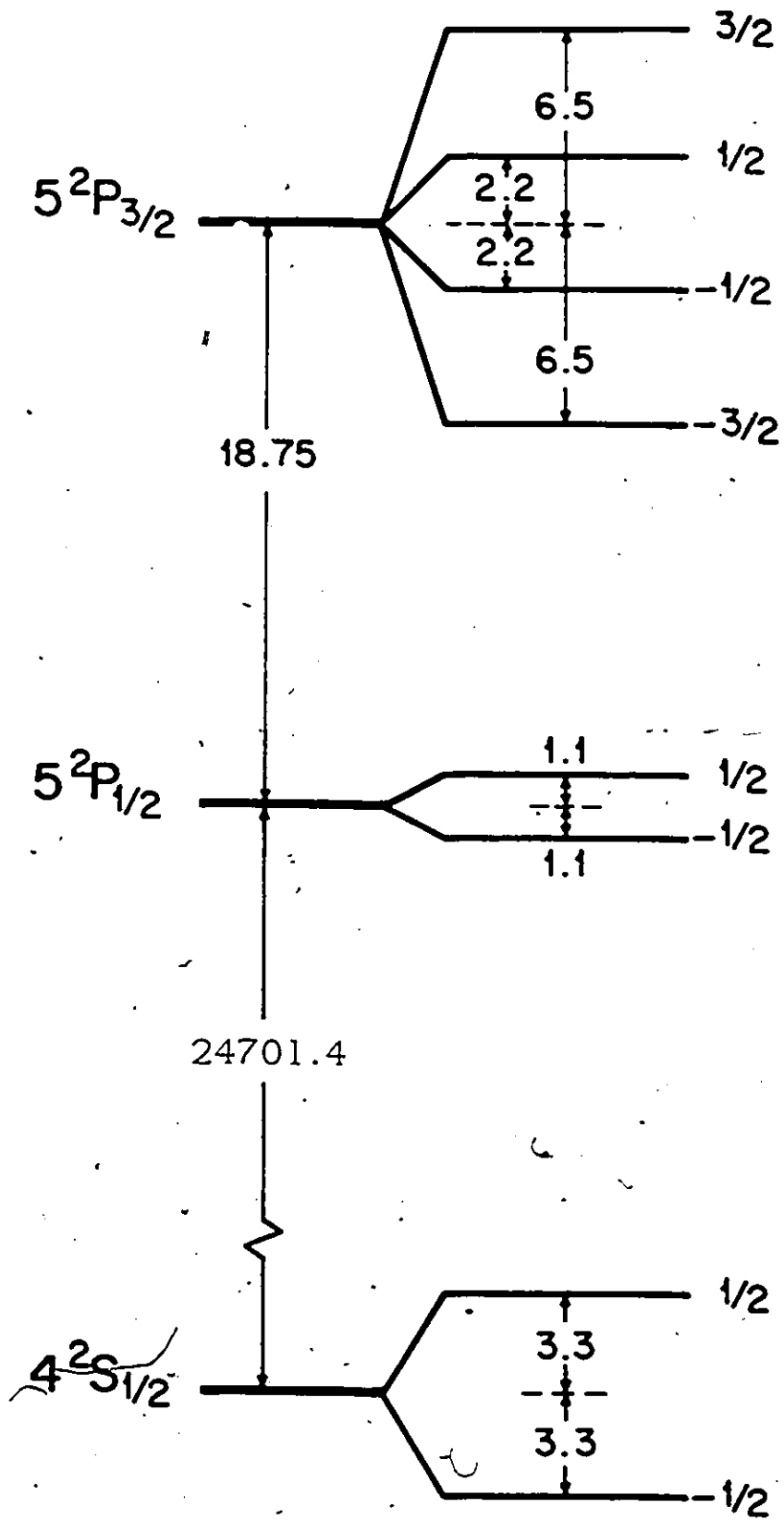
$$g_j = 1 + \frac{S(S+1) + J(J+1) - L(L+1)}{2J(J+1)} \quad (6.3)$$

The Zeeman displacements per gauss for the  $4^2S$ ,  $5^2P$  and  $5^2D$  states, as calculated using eq. (6.2) are listed in Table (6.1).

Table (6.1) Zeeman Displacement $\Delta \nu$ in Relation to Magnetic Field Strength B(Gauss) ( $\pm 10^{-5} \text{cm}^{-1}/G$ )			
FS State	$m_j = \pm 1/2$	$m_j = \pm 3/2$	$m_j = \pm 5/2$
$5^2D_{5/2}$	2.8014	8.4042	1.4007
$5^2D_{3/2}$	1.8676	5.6028	
$5^2P_{3/2}$	3.113	9.338	
$5^2P_{1/2}$	1.556		
$5^2S_{1/2}$	4.669		

Figure (6.1)

The relative displacements of the  $5P$  Zeeman substates  
in a magnetic field of 70 kG (drawn to scale)



## 7 APPENDIX B: Feasibility of an Experimental Study of Zeeman Mixing In the 5D State

### 1. Applications of Density Matrix Formalism to the Collisional Decay of Atomic Multipole Moments in the 5D State

Collisional Zeeman mixing with noble gases within the 5D state may be described by the following eqs.:

$$K\left(5^2D_{\frac{5}{2},-\frac{5}{2}}\right) + X \rightarrow K\left(5^2D_{J,m}\right) + X + \Delta E \quad (7.1.1)$$

$$K\left(5^2D_{\frac{3}{2},-\frac{3}{2}}\right) + X \rightarrow K\left(5^2D_{J',m'}\right) + X + \Delta E \quad (7.1.2)$$

where X is a buffer gas molecule. When J or J'=5/2, m or m' =  $\pm 5/2, 3/2$  or  $1/2$ ; when J or J'=3/2, m or m' =  $\pm 3/2$  or  $\pm 1/2$ . There are altogether ten Zeeman substates within this doublet manifold.

The population vector  $\bar{N}$  describing the population density of the potassium atoms in the Zeeman substates must accordingly be described by a ten-dimensional vector. The time evolution of the population density vector  $\bar{N}$  may be represented using density matrix formalism (Baylis, 1978).

$$\dot{\bar{N}} = \frac{d\bar{N}}{dt} = \bar{S} - \bar{\Gamma}\bar{N} - \bar{\gamma}\bar{N} \quad (7.1.3)$$

Assuming pulsed excitation and time integration of the population as was done for the 5P state in section (2.2), one has the rate equation;

$$\bar{\vec{S}} - \bar{r} \bar{\vec{N}} - \bar{y} \bar{\vec{N}} = 0 \quad (7.1.4)$$

where the horizontal bars indicates the time-integrated quantities.  $\bar{\vec{N}}$  is expressed in terms of the spherical basis vectors corresponding to the multipole density distribution which are defined as follows:

$$\hat{T}_{3L}^T = (\hat{u}_{3L}^T, 0) \quad L = 0, 1, 2, 3 \quad (7.1.5)$$

$$\hat{T}_{5L}^T = (0, \hat{u}_{5L}^T) \quad L = 0, 1, 2, 3, 4, 5 \quad (7.1.6)$$

Where  $\hat{u}_{3L}^T$  and  $\hat{u}_{5L}^T$  are the 4-dimensional and 6-dimensional spherical basis vectors, respectively (Baylis, 1987), identified with the multipole distributions associated with the  $D_{3/2}$  and  $D_{5/2}$  states.

$$\hat{u}_{30}^T = \frac{1}{\sqrt{2}}(1, 1, 1, 1) \quad (7.1.7)$$

$$\hat{u}_{31}^T = \frac{1}{2\sqrt{5}}(3, 1, -1, -3) \quad (7.1.8)$$

$$\hat{u}_{32}^T = \frac{1}{2}(1, -1, -1, 1) \quad (7.1.9)$$

$$\hat{u}_{33}^T = \frac{1}{2\sqrt{5}}(1, -3, 3, -1) \quad (7.1.10)$$

$$\hat{u}_{50}^T = \frac{1}{\sqrt{6}}(1, 1, 1, 1, 1, 1) \quad (7.1.11)$$

$$\hat{u}_{51}^T = \frac{1}{\sqrt{70}}(5, 3, 1, -1, -3, -5) \quad (7.1.12)$$

$$\hat{u}_{52}^T = \frac{1}{4\sqrt{21}}(10, -2, -8, -8, -2, 10) \quad (7.1.13)$$

$$\hat{u}_{53}^T = \frac{1}{6\sqrt{5}}(5, -7, -4, 4, 7, -5) \quad (7.1.14)$$

$$\hat{u}_{54}^T = \frac{1}{2\sqrt{7}}(1, -3, 2, 2, -3, 1) \quad (7.1.15)$$

$$\bar{u}_{ss}^T = \frac{1}{6\sqrt{7}}(1, -5, 10, -10, 5, 1) \quad (7.1.16)$$

The quantities  $\bar{N}$ ,  $\bar{S}$ ,  $\hat{r}$  and  $\hat{y}$  can be expressed to reflect the separate population and excitation of the two fs states. In the following equations the subscript (3) indicates the  $S^2D_{3/2}$  state and the subscript (5) represents the  $S^2D_{5/2}$  state.

$$\bar{N} = \begin{pmatrix} \bar{N}_3 \\ \bar{N}_5 \end{pmatrix} \quad (7.1.17) \quad \bar{S} = \begin{pmatrix} \bar{S}_3 \\ \bar{S}_5 \end{pmatrix} \quad (7.1.18)$$

$$\hat{r} = \begin{pmatrix} \tau_3^{-1} \mathbb{1}_3 & 0 \\ 0 & \tau_5^{-1} \mathbb{1}_5 \end{pmatrix} \quad (7.1.19) \quad \hat{y} = \begin{pmatrix} \hat{y}_{33} & \hat{y}_{35} \\ \hat{y}_{35} & \hat{y}_{55} \end{pmatrix} \quad (7.1.20)$$

$\mathbb{1}_3$  is the four-dimensional identity matrix,  $\mathbb{1}_5$  is the six-dimensional identity matrix and 0 represents the appropriately dimensioned null matrix. The radiative decay matrix components  $\tau_3 = \tau(S^2D_{3/2}) = 572.14$ , and  $\tau_5 = \tau(S^2D_{5/2}) = 553.16$  ns are the lifetimes of the  $S^2D$  state (Hart and Atkinson, 1986). The  $\hat{y}_{ij}$  components of  $\hat{y}$  are 4x4, 4x6, 6x4, 6x6 dimensional matrices, respectively.

Using these equations as shown in section (2.2), one obtains:

$$\begin{pmatrix} \tau_3^{-1} \mathbb{1}_3 + \hat{y}_{33} & \hat{y}_{35} \\ \hat{y}_{35} & \tau_5^{-1} \mathbb{1}_5 + \hat{y}_{55} \end{pmatrix} \begin{pmatrix} \bar{N}_3 \\ \bar{N}_5 \end{pmatrix} = \begin{pmatrix} \bar{S}_3 \\ \bar{S}_5 \end{pmatrix} \quad (6.2.21)$$

$$\bar{N} = \begin{pmatrix} \bar{N}_3 \\ \bar{N}_5 \end{pmatrix} = \sum_{l=0}^3 \begin{pmatrix} n_3^{(l)} \hat{u}_{3l} \\ 0 \end{pmatrix} + \sum_{l=0}^5 \begin{pmatrix} 0 \\ n_5^{(l)} \hat{u}_{5l} \end{pmatrix} \quad (6.2.22)$$

$$n_3^{(l)} = \hat{u}_{3l} \cdot \bar{N}_3 \quad (7.1.23)$$

$$n_5^{(l)} = \hat{u}_{5l}^T \cdot \bar{N}_5 \quad (7.1.24)$$

where the vector  $\bar{N}$  is now expressed in terms of the spherical basis vectors (7.1.7-16). The equations for  $\bar{s}$ ,  $s_3^{(L)}$  and  $s_s^{(L)}$  have a similar format. The quantities  $n_3^{(L)}$  and  $n_s^{(L)}$  represent the  $2^L$ -th multipole moment density associated with  $\bar{N}$ , and  $\bar{N}_s$ , respectively.

Equation (7.1.21) may be expressed in terms of the multipole densities:

$$\begin{pmatrix} \tau_3^{-1} + \gamma_{33}^{(L)} & \gamma_{3s}^{(L)} \\ \gamma_{s3} & \tau_s^{-1} + \gamma_{ss}^{(L)} \end{pmatrix} \begin{pmatrix} n_3^{(L)} \\ n_s^{(L)} \end{pmatrix} = \begin{pmatrix} s_3^{(L)} \\ s_s^{(L)} \end{pmatrix}. \quad (6.2.25)$$

The matrix elements are defined as follows.

$$\gamma_{33}^{(L)} = \bar{u}_{3L}^T (\bar{\gamma}_{33}) \bar{u}_{3L} \quad L=0,1,2,3 \quad (7.1.26)$$

$$\gamma_{ss}^{(L)} = \bar{u}_{sL}^T (\bar{\gamma}_{ss}) \bar{u}_{sL} \quad L=0,1,2,3,4,5 \quad (7.1.27)$$

$$\gamma_{3s}^{(L)} = \bar{u}_{3L}^T (\bar{\gamma}_{3s}) \bar{u}_{sL} \quad L=0,1,2,3 \quad (7.1.28)$$

$$\gamma_{s3}^{(L)} = \bar{u}_{sL}^T (\bar{\gamma}_{s3}) \bar{u}_{3L} \quad L=0,1,2,3 \quad (7.1.29)$$

$\gamma_{33}^{(L)}$  and  $\gamma_{ss}^{(L)}$  are the multipole decay rates. The elements  $\gamma_{33}^{(0)}$  and  $\gamma_{ss}^{(0)}$  are the fs excitation transfer rates for the  $(5^2D_{5/2} \rightarrow 5^2D_{3/2})$  and  $(5^2D_{5/2} \rightarrow 5^2D_{3/2})$  transitions, respectively. The elements  $\gamma_{33}^{(0)}$  are the fs orientation transfer rates.

The multipole decay rates are expressed in terms of the depopulation rates  $\gamma^{(0)}$  and the multipole relaxation rates  $\lambda^{(L)}$ .

$$\gamma_{33}^{(1)} = \gamma_{33}^{(0)} + \lambda_{33}^{(1)} \quad (7.1.30)$$

$$\gamma_{ss}^{(L)} = \gamma_{ss}^{(0)} + \lambda_{ss}^{(L)} \quad (7.1.31)$$

The multipole decay cross sections  $\sigma_{33}^{(L)}$  and  $\sigma_{ss}^{(L)}$  ( $L=1,2,3$ ) are defined by

$$\gamma_{33}^{(L)} = N\nu\sigma_{33}^{(L)} = N\nu\sigma_{3/2}^{(L)} \quad (7.1.32) \quad \gamma_{ss}^{(L)} = N\nu\sigma_{ss}^{(L)} = N\nu\sigma_{5/2}^{(L)} \quad (7.1.33)$$

The multipole relaxation rates  $\lambda^L$  are:

$$\lambda_{33}^{(L)} = N\nu A_{3/2}^{(L)} \quad (7.1.34)$$

$$\lambda_{55}^{(L)} = N\nu A_{5/2}^{(L)} \quad (7.1.35)$$

$$\sigma_{33}^{(1)} = \sigma_{33}^{(0)} + A_{3/2}^{(1)} \quad (7.1.36)$$

$$\sigma_{55}^{(L)} = \sigma_{55}^{(0)} + A_{5/2}^{(L)} \quad (7.1.37)$$

where  $A_{33}^{(L)}$  and  $A_{55}^{(L)}$  are the multipole relaxation cross sections.

Substitution of equations (7.1.30-37) into (7.1.25) yields:

$$\begin{pmatrix} n_3^{(L)} \\ n_5^{(L)} \end{pmatrix} = D_L^{-1} \begin{pmatrix} \tau_5^{-1} + \gamma_{55}^{(L)} & -\gamma_{35}^{(L)} \\ -\gamma_{53}^{(L)} & \tau_3^{-1} + \gamma_{33}^{(L)} \end{pmatrix} \begin{pmatrix} s_3^{(L)} \\ s_5^{(L)} \end{pmatrix} \quad (7.2.38)$$

$$D_L = (\tau_3^{-1} + \gamma_{33}^{(L)})(\tau_5^{-1} + \gamma_{55}^{(L)}) - \gamma_{53}^{(L)}\gamma_{35}^{(L)} \quad (7.1.39)$$

In order to simplify further manipulation, the following variable is defined as the ratio of the multipole population multiplied by the excitation rate ratio.

$$K_{ab}^{LL'} = \frac{n_b^{(L)}}{n_b^{(L')}} \cdot \frac{s_a^{(L')}}{s_a^{(L)}} \quad a, b = 3, 5 \quad (2.2.40)$$

The solution of eq. (7.2.38) for the multipole relaxation cross sections follows by considering the conditions of optical excitation. The first example involves the excitation of the  $5^1D_{3/2,3/2}$  state while the second results from only  $5^1D_{3/2,1/2}$  excitation.

(i) When the  $5^1D_{3/2,3/2}$  is optically excited,

$$\vec{s}_5^T = (0, 0, 0, s_{3/2-3/2}); \quad s_5^{(L)} = 0 \quad L = 0, 1, 2, 3, 4, 5.$$

$$n_3^{(L)} = D_L^{-1} s_3^{(L)} (\tau_3^{-1} + \gamma_{33}^{(L)}) \quad (7.1.41)$$

which reduces to:



$$K_{33}^{0L} = \frac{n_3^{(0)} s_3^{(L)}}{n_3^{(L)} s_3^{(0)}} = \frac{(\tau_s^{-1} + \gamma_{ss}^{(0)})}{(\tau_s^{-1} + \gamma_{33}^{(L)})} \cdot \frac{D_L}{D_0} \quad (6.2.42)$$

$$K_{35}^{0L} = \frac{\gamma_{35}^{(0)} D_L}{\gamma_{35}^{(L)} D_0} \quad (7.1.43)$$

(ii) When the  $K^2 D_{5/2-5/2}$  state is optically excited,

$$s_1^{(L)} = 0 \quad L = 0, 1; \quad \vec{S}_2^T = (0, 0, 0, 0, 0, S_{5/2-5/2})$$

$$n_5^L = D_L^{-1} s_5^{(L)} (\tau_s^{-1} + \gamma_{33}^{(L)}) \quad (7.1.44)$$

$$K_{ss}^{0L} = \frac{(\tau_3^{-1} + \gamma_{33}^{(0)}) D_L}{(\tau_3^{-1} + \gamma_{33}^{(L)}) D_0} \quad (7.1.45)$$

$$K_{53}^{0L} = \frac{\gamma_{53}^{(0)} D_L}{\gamma_{53}^{(L)} D_0} \quad L = 0, 1, 2, 3 \quad (7.1.46)$$

The K coefficients are related to the experimentally measured intensities of the components in the resolved Zeeman fluorescence spectra. The explicit forms of K are derived from the definitions of the multipole population and excitation densities given in eqs. (7.1.7-13).

The population ratios required for the K coefficients are obtained from the ratio of the experimental fluorescence intensities multiplied by the appropriate A coefficients assuming single collision conditions:

$$\frac{N_{JM}}{N_{J'M'}} = \frac{I_{JM}}{I_{J'M'}} \cdot \frac{A_{J'M'}^0}{A_{JM}^0} \quad (7.1.47)$$

The A coefficients for the decay of the 5D state to the 4P state have been summarized in table (7.1) for zero magnetic field.

The final equations for the multipole relaxation cross sections of the D states analogous to those for the P states and are now listed.

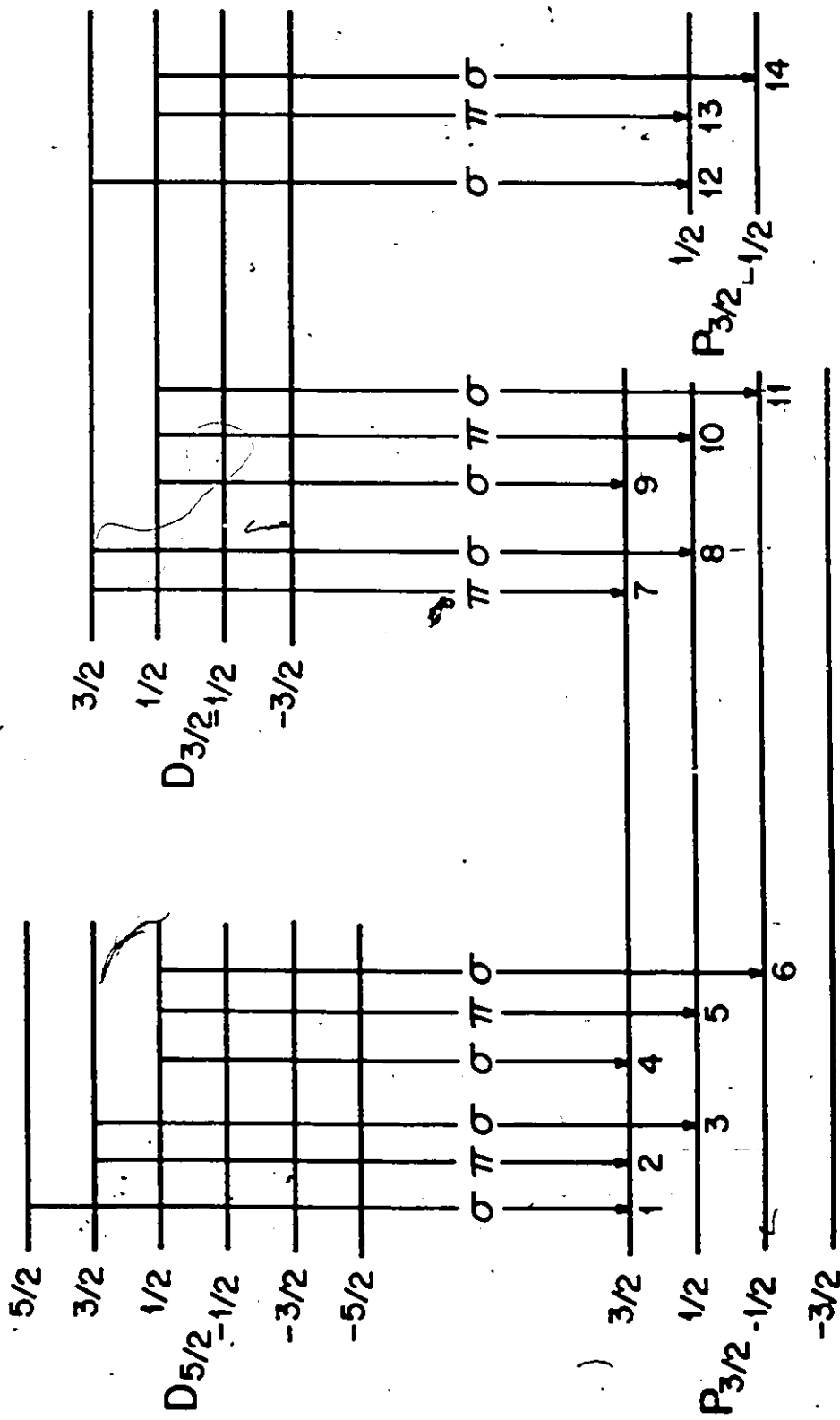
$$A_{3/2}^{(L)} = \frac{1}{N\nu\tau_3} [K_{33}^{0L} - 1] + (K_{33}^{0L} - 1)\sigma_{33}^{(0)} - \frac{K_{33}^{0L}\tau_5\sigma_{35}^0\sigma_{53}^0}{1/N\nu + \tau_5\sigma_{55}^{(0)}} + \frac{\tau_5\sigma_{35}^{(L)}\sigma_{53}^{(L)}}{1/N\nu + \tau_5\sigma_{55}^{(L)}} \quad (7.1.48)$$

$$A_{5/2}^{(L)} = \frac{1}{N\nu\tau_5} [K_{55}^{0L} - 1] + (K_{55}^{0L} - 1)\sigma_{55}^{(0)} - \frac{K_{55}^{0L}\tau_3\sigma_{53}^0\sigma_{35}^0}{1/N\nu + \tau_3\sigma_{33}^{(0)}} + \frac{\tau_3\sigma_{53}^{(L)}\sigma_{35}^{(L)}}{1/N\nu + \tau_3\sigma_{33}^{(L)}} \quad (7.1.49)$$

Table (7.1) Relative $A_i$ Coefficients for 5D→4P Radiative Polarized Emission		
(1) 61.98	(7) 9.00	(12) 57.80
(2) 24.79	(8) 6.00	(13) 38.53
(3) 37.19	(9) 6.00	(14) 19.28
(4) 6.198	(10) 1.00	
(5) 37.19	(11) 8.00	
The various $A_i$ are numbered to correspond with the transitions shown in Fig. (7.1).		
Note: The geometrical observation factor $\pi/\sigma$ has not been included in the above values. When comparing $\pi$ intensities observed perpendicular to the magnetic field with $\sigma$ components observed parallel to the magnetic field, the $\pi$ components are a factor of two weaker (Woodgate, 1980).		
The relative A coefficients were derived using the following transition probabilities for the 5D→4P fs transitions (Hart 1983).		
$5^2P_{3/2} \rightarrow 4^2P_{3/2} = 7.302 \times 10^5$		
$5^2P_{3/2} \rightarrow 4^2P_{1/2} = 1.178 \times 10^5$		
$5^2P_{3/2} \rightarrow 4^2P_{1/2} = 4.540 \times 10^5$		

Figure (7.1)

Transition diagram for the radiative decay of the 5D state. The (#) listed under individual transitions references the relative A coefficients presented on the previous page.



## 2. Preliminary Experimental Study of the D States

In order to determine whether it would be possible to excite a single Zeeman sublevel of the  $^2D$  states, it was first necessary to determine which D states were experimentally accessible.

The first state to be directly pumped was the  $3D$  state, which was easily excited by means of a quadrupole transition at 464 nm. The  $3D$  fs splitting is  $2.33 \text{ cm}^{-1}$  which was sufficient to allow the selective pumping of either sublevel. The oscillator strength for the  $3D \rightarrow 4P$  decay, which has a value of .9 (Wiese et al. 1969), is the highest among the various  $D \rightarrow 4P$  transitions. Unfortunately the  $3D \rightarrow 4P$  decay wavelength is in the infrared (1170nm) and not directly detectable, although the cascade from the  $4P \rightarrow 4S$  was detected.

In the  $4D$  state the fs splitting is  $1.1 \text{ cm}^{-1}$  and its decay to the  $4P$  level gives rise to fluorescence at 694nm. All attempts to excite this state either by a quadrupole transition at 365nm or by two-photon excitation at 730 nm were unsuccessful. These wavelengths are in general very difficult to generate with a  $N_2$  laser-pumped dye laser and further trials were attempted with the aid of the more powerful Nd:YAG laser. A very faint signal from this transition was intermittently registered on the thermionic diode with intense laser excitation, however the signal was not stable and fluorescence was not observed. The primary reason for these difficulties is the anomalously small oscillator strength for the  $4D \rightarrow 4P$  transition ( $4 \times 10^{-4}$ ) (Theodosiou (1980)). This state had also been investigated by Hart (1983) who experienced similar difficulties.

The 5D state has a fs splitting of  $0.5 \text{ cm}^{-1}$ , it decays to the 4P-state emitting fluorescence of wavelength near 582 nm and has an oscillator strength of 0.003. This state was readily excited and fluorescence from both fs levels was detected. The bandwidth of the laser (4 GHz) was not sufficiently narrow to excite the fs states separately, using frequency doubling or two photon excitation, although the  $5D_{5/2} \rightarrow 4P_{3/2}$  and  $5D_{3/2} \rightarrow 4P_{1/2}$  transitions were spectrally resolved and tentative lifetime determinations of 5D fs states were found in agreement with those by Hart (1983). The 6D state, whose fs splitting is  $0.3 \text{ cm}^{-1}$ , was also investigated with similar results.

The use of a ring laser with its inherently narrow bandwidth would facilitate selective excitation. D-state excitation requires either two-photon or quadrupole pumping from the 4S ground state and as these are nonlinear processes, they require high laser power densities to be effective. The ring laser is a cw device whose power is 5 orders of magnitude lower than the peak power of a modest pulsed dye laser, which is not sufficiently powerful to adequately populate these states. Very tight focussing of a ring laser beam into a cell containing a high density of potassium vapour, at a wavelength appropriate for 7D and 6S state excitation, produced no detectable fluorescence, indicating that much higher power densities will be required to excite these states by two-photon absorption.

It is, however, also possible to utilize the ring laser as the effective oscillator cavity for a  $N_2$  laser-pumped dye laser. The ring laser output would enter the dye cells of a three- or four-stage dye laser where the cw input would be converted into a pulse of sufficient energy to produce the

required excitation wavelength and of bandwidth much narrower than that produced by the usual pulsed dye laser (3-4 GHz).

There are several difficulties to be anticipated in attempting to determine the multipole relaxation cross sections for a set of substates whose sheer number adds to the complexity of the problem. The fs states are very close to each other and fs mixing will be a dominant process. This will have to be initially studied in zero field, using the method employed for the 5P states. The Zeeman sublevels of the two fs states begin to cross at a field strength of 1500 G, and at higher fields additional level crossings and anti-crossings will require that the field strength be chosen so as to avoid accidental degeneracy. The equations for the multipole relaxation cross sections are coupled and can only be solved through an iterative process. The relaxation cross sections may be obtained if a sufficient number of individual Zeeman mixing cross sections can be determined from the fluorescence intensity ratios at low buffer gas pressures. However, with a total of 10 different transitions to resolve, accidental overlaps of the interferometer peaks may occur obscuring the spectrum. Although the accurate determination of the multipole relaxation cross sections may not be possible, it should be possible to excite selected Zeeman sublevels and obtain the Zeeman mixing cross sections from the resolved fluorescence.

## BIBLIOGRAPHY

- Baylis W., 1978, in Progress in Atomic Spectroscopy  
Pt.B, Eds. W.Hanle and H.Kleinpoppen,  
Plenum Press, New York
- Baylis W., 1983, 1987-88, private communication
- Behmenburg W., Kroop V. and Rebentrost F., 1985,  
J.Phys.B: At.Mol.Phys. 18, 2693
- Bellisio J.A., Davidovits P. and Kindlman P.J., 1968  
J.Chem.Phys. 48, 2376
- Berdowski W. and Krause L., 1968, Phys.Rev. 165, 158
- Berdowski W., Shiner T. and Krause L., (1971), Phys.  
Rev. A 4, 984
- Berends R.W., Kedzierski W. and Krause L., 1988, Phys.  
Rev.A, 37, pg.63, eq. (11).
- Berends R.W., Skalinski P. and Krause L., 1984, J. .  
Phys. B At.Mol.Phys. 17, 605
- Bevington P.R., 1969, Data Reduction and Error Analysis  
for the Physical Sciences, McGraw Hill,  
New York (1969), pg. 118
- Boggy R. and Franz F.A., 1982, Phys.Rev.A 25, 1887
- Bulos R.B. and Happer W., 1971, Phys.Rev.A 4, 349
- Cario G. and Franck J., 1922, Z.Physik 11, 161
- Copley G. and Krause L., 1969, Can.J.Phys. 47, 533
- Dodd J.N. and Series G.W., 1978, in Progress in Atomic  
Spectroscopy Pt.A, Eds. W.Hanle and  
H.Kleinpoppen, Plenum Press, New York
- D'Yakonov M.I. and Perel V.I., 1965, Zh.Eksp.Teor.Fiz.,  
48, 345, Sov.Phys.- JETP 21, 227
- Elbel M., 1978, in Progress in Atomic Spectroscopy  
Pt.B, Eds. W.Hanle and H.Kleinpoppen,  
Plenum Press, New York
- Fano U., 1957, Rev.Mod.Phys. 29, 74
- Gay J.-C. and Schneider W.B., 1976, Z.Phys.A 278, 211
- Grudzev P.F. and Denisov V.I., 1982, Opt. Spectrosc.  
(USSR) 52, 8
- Hart D., 1983, M.Sc.Thesis, University of Windsor,  
(unpublished)



- Hart D. and Atkinson J.B., 1986, J.Phys.B: At.Mol.Phys. 19, 43
- Harvey K.C., 1981, Rev.Sci.Instrum. 52(2), 204
- Krause L., 1972, in Physics of Electronic and Atomic Collisions, Eds. T.R.Govers and F.J. de Heer, North-Holland pg.65
- Lochte-Holtgreven W., 1928, Z.Physik 47, 362
- Lu D and Wu Z, 1984, Opt. Laser Technol. 16 206.
- Masnou-Seeuws F. (1982), J.Phys.B: Atom.Mol.Phys., Vol. 15,883
- Niemax K. and Weber K.-H., 1978, J.Phys.B: Atom.Molec. Phys. Vol. 11, No.8
- Mitchell A. and Zemansky M., 1934, Resonance Radiation and Excited Atoms, Cambridge University Press, N.Y.
- Morris M.B., McIlrath T.J. and Snyder J.J., 1984, App. Opt. 23 3862
- Mrozowski S., 1932, Z.Physik 78, 826
- Nestor J.R., 1982, Applied Optics, Vol.21, No.22, 4154
- Ney J., 1969, Z.Phys. 223, 126
- Omont A., 1965, J.Physique 26, 26
- Omont A., 1977, Prog.Quantum Electronics, Vol.5, 69-138, Pergamon Press
- Pace P. and Atkinson J.B., 1974, Can.J.Phys. 52,1635
- Pascale J., Mestdagh J.M., Cuvellier J. and de Pujo P., 1984, J.Phys.B : At.Mol.Phys. 17, 2627
- Pascale J., 1987, private communication
- Pascale J. and Vandeplanque J., 1974, J.Chem Phys. 60, 2278
- Pimbert M., Rocchiccioli J.L., Cuvellier J. and Pascale J., 1970, C.R.Acad.Sc. B271, 415
- Rebentrost F., Best R. and Behmenburg W., 1987, J.Phys. B: At.Mol:Phys. 20, 2627
- Rogers J.R., 1982, J. Opt. Soc. Am. 72, 638
- Schmieder R.W., Lurio A. and Happer W., 1968, Phys. Rev.A, 173, 76
- Seiwert R., 1956, Ann.Physik 18, 54
- Seiwert R., 1956, Ann.Physik 17,371

- Siara I., Hrycyshyn E.S. and Krause L., 1972, Can.J. Phys. 50, 1826
- Siara I., Hrycyshyn E.S. and Krause L., 1972, Can.J. Phys. 50 1826
- Siara I., Kwong H.S. and Krause L., 1974, Can.J. Phys. 52, 945
- Skalinski P. and Krause L., 1982 Phys.Rev.A 26, 3338
- Snyder J.J., 1980, Appl. Opt. 19, 1223
- Snyder J.J., 1981, Proc. Soc. Photo-Opt. Instrum. Eng. 288 258.
- Spielfiedel A. and Feautrier N. (1988), Private Communication
- Spielfiedel A., Gilbert D., Roueff E. and Rostas F., 1979, J.Phys.B: At.Mol.Phys. 12, 3693
- Svanberg S., 1971, Phys.Scripta 4, 275
- Theodosiou C.E., 1980, J.Phys.B: Atom.Mol.Phys. 13, L1
- Theodosiou C.E., 1984, Phys.Rev. A 30, 2881
- Warner B., 1968, Mon.Not.R.Astron.Soc. 139, 115-28
- Wiese W.L., Smith M.W. and Miles B.M., 1969, Atomic Transition Probabilities, 22 Vol.II, p.225, NSRDS, Washington D.C.
- Wilson A.D. and Shimoni Y., 1975, J.Phys.B 8, 2393
- Wood W. and Mohler F.L., 1918, Phys.Rev. 11, 70
- Wood W. and Dunoyer L., 1914 Phil. Mag. 27, 1018
- Wood R.W., 1922, Phil.Mag. 44, 1107
- Woodgate G.K., 1980, Elementary Atomic Structure 2nd Ed., Clarendon Press, Oxford
- van Wijngaarden W.A., Bonin K.D. and Happer W., 1986, Phys.Rev.A 33, 77
- von Keussler V., 1927, Ann.Physik 87, 793

### VITA AUCTORIS

I was born in Hamilton, Ontario on March 28, 1960. After graduating from Forster Secondary School in Windsor in 1978, I began my studies in Physics at the University of Windsor. I graduated in 1982 with an Honours B.Sc. and entered the Faculty of Graduate Studies. I graduated with an M.Sc. in 1983. I served on the Executive of the Graduate Student Society and the Senate of the University from 1984-85. I have been fortunate to hold an Alumni Entrance Scholarship during my undergraduate studies and an NSERC Postgraduate Scholarship during my graduate studies.